RESOLVED SIDEBAND SPECTROSCOPY FOR THE DETECTION OF WEAK OPTICAL TRANSITIONS

A Thesis
Presented to
The Academic Faculty

by

James E. Goeders

In Partial Fulfillment
of the Requirements for the Degree
Doctor of Philosophy in the
School of Chemistry and Biochemistry

Georgia Institute of Technology
August 2013

RESOLVED SIDEBAND SPECTROSCOPY FOR THE DETECTION OF WEAK OPTICAL TRANSITIONS

Approved by:

Professor Kenneth R. Brown, Advisor
Schools of Chemistry and Biochemistry, Computational Science and Engineering, and Physics
Georgia Institute of Technology

Professor Thomas M. Orlando
Schools of Chemistry and Biochemistry, and Physics
Georgia Institute of Technology

Professor Michael S. Chapman
School of Physics
Georgia Institute of Technology

Doctor Richart E. Slusher
Georgia Tech Quantum Institute
Georgia Tech Research Institute

Professor Facundo M. Fernández
School of Chemistry and Biochemistry
Georgia Institute of Technology

Date Approved: 25 June 2013

To Karen

PREFACE

"If it disagrees with experiment it is wrong. In that simple statement is the key to science. It does not make any difference how beautiful your guess is. It does not make any difference how smart you are, who made the guess, or what his name is – if it disagrees with experiment it is wrong. That is all there is to it."
-Richard Feynman, "The Character of Physical Law"

"I suddenly realized why Princeton was getting results. They were working with the instrument. They *built* the instrument; they knew where everything was, they knew how everything worked, there was no engineer involved, except maybe he was working there too. It was much smaller than the cyclotron at MIT, and "gold-plated"?–it was the exact opposite. When they wanted to fix a vacuum, they'd drip glyptal on it, so there were drops of glyptal on the floor. It was wonderful! Because they *worked* with it. They didn't have to sit in another room and push buttons!"
-Richard Feynman, "Surely You're Joking, Mr Feynman!"

ACKNOWLEDGEMENTS

When I first arrived in Atlanta in May of 2006, I never would have imagined I would be finishing a PhD studying molecular spectroscopy of single ions seven years later. It has certainly been an interesting journey. Many thanks to:

Kenneth Brown, my PhD advisor, who took a chance on a guy who admitted to not being that great at chemistry. Many times I thought of Ken more as a friend than as a boss; always willing to go to Moe's for a burrito or just sit in his office and talk. I appreciate Ken's patience as I stumbled through learning the basics of atomic physics and for always being excited alongside me, no matter how insignificant the breakthrough. I also cannot imagine anyone else singing lead vocals for KEN Speedwagon.

Charlie Doret, who was just as valuable as a golfing buddy as he was at answering so many of my questions. Charlie was invaluable during a number of my infamous "hate-spirals," especially in my last two years when I was fighting with sideband cooling and never thought I would actually graduate. He is also one of few people to rival my editing abilities.

Grahame Vittorini, who took over on the "Oliver" cavity for me, and so I will be forever grateful. Without his work on the cavity and electronics for the 729 nm laser, none of my experiments would be possible. In addition, some of my fondest memories from graduate school will surely be Rock Band nights at the old house on Charles Allen.

Amy Jablonski, my lunchtime companion, who was always willing to put up with Charlie, Grahame, and me discussing physics so long as we also occasionally discussed football. I will miss our daily excursions to Tech Square.

Craig Clark, who I spent so much of my life with those early years. I appreciate you teaching me the method and the "ultimate test."

Ricardo Viteri, our first postdoc, who taught me many things about science, life, and wing eating. The best guitarist I have ever known.

Yatis Dodia, who built the first DDS and received countless (mostly unwarranted) swears over its perceived deficiencies. We should have gone to see Rage Against the Machine in California that first summer!

True Merrill, the man who stole my overflow desk and who always overestimated my knowledge base. I'm sorry for all the ribbing we gave you over the years, you just make it so easy some times.

Ncamiso JB Khanyile and Gang Rick Shu, who built the transfer cavity to lock the rest of the lasers, and my fellow experimenters after Craig left for Sandia. I wish we could have spent more time kicking ass and less time dealing with lab demons.

Aaron Moon, Karl Burkhardt, and Spencer Nichols, the three undergraduate students that I had the pleasure to work with the most. I apologize for all the times I was a poor mentor too focused on my own experiments. I enjoyed discussing things with the three of you, and often fed off of your optimism.

The Brown group as a whole, who helped make life enjoyable when experiments were not. I enjoyed all of the group activities, especially everyone growing a mustache in the summer of 2011.

The Quantum Information Systems group at GTRI, who provided an immense amount of knowledge and an untold amount of supplies.

Kurt Wiesmann and Dennis Denney, for teaching me in their own ways about machining and part design.

A number of fantastic teachers that I have interacted with in my several decades of being a student, particularly: Jan Gardner, Robin McCarley, Hal Meekins, Charlotte Miley, Kermit Murray, Kathy O'Neal, Paige Patterson, Robert Perlis, Erwin Poliakoff,

Leonard Richardson, Kresimir Rupnik, David Sherrill, and Cathy Williamson.

All of the people that make Georgia Tech function: Nicole Thompson (the greatest admin anyone could ever ask for), Kevin and Jason in the VWR Stockroom, the fantastic facilities people, and all of the great friends I have made in my years here. It has been a pleasure calling Georgia Tech home.

Finally, to my family, for providing encouragement and understanding no matter my goal. And to my wife, Karen, who was so very understanding of all the late nights and weekends spent in lab, for supporting me even when I left Emory, and who was the one that suggested I "go talk to this young guy at Tech who seems really smart and is doing some crazy stuff with single atoms."

TABLE OF CONTENTS

LIST OF TABLES

LIST OF FIGURES

SUMMARY

This thesis reports on the setup of a new ion trap apparatus designed for experiments with single $^{40}Ca^{+}$ ions to perform molecular spectroscopy. The calcium ion is laser cooled, allowing for sympathetic cooling of the nonfluorescing molecular ion. The aim of these experiments is to explore loading and identifying molecular ions in Paul traps, as well as developing new spectroscopic tools to measure transitions of molecular ions via the fluorescence of co-trapped $^{40}Ca^{+}$ ions. Ground state cooling of a mixed ion pair is implemented as a first step towards increasing the sensitivity of our technique to the level necessary to measure transitions with low scattering rates (like those present in molecular ions).

Doppler cooling on the $S_{1/2} \rightarrow P_{1/2}$ transition of the calcium ion results in the formation of a Coulomb crystal, the behavior of which may be used to infer properties of the molecular ion. Following cooling, sideband spectroscopy on the narrow $S_{1/2} \rightarrow D_{5/2}$ quadrupole transition of calcium may be used to identify the mass of single molecular ions. This method is verified via a non-destructive measurement on $^{40}CaH^{+}$ and $^{40}Ca^{16}O^{+}$.

The normal modes of the Coulomb crystal can also be used to extract information from the target ion to the control ion. By driving the blue side of a transition, laser induced heating can be put into the two ion system, which leads to changes in fluorescence of the $^{40}Ca^{+}$ ion, first demonstrated with two Ca^{+} isotopes. Increasing the sensitivity of this technique requires ground state cooling of both the $^{40}Ca^{+}$ ion and the ion of interest, enabling the transfer of the ion's motional state into the ground state with high probability. This thesis demonstrates ground state cooling of

the atomic ion and sympathetic cooling of a second ion ($^{44}Ca^{+}$). Once in the ground state, heating of the Coulomb crystal by scattering photons off of the spectroscopy ion can be measured by monitoring the resolved motional sidebands of the $S_{1/2} \rightarrow D_{5/2}$ transition of $^{40}Ca^{+}$, allowing for spectral lines to be inferred. Future experiments will investigate this technique with molecular ions.

CHAPTER I

INTRODUCTION

By making use of tools developed for quantum computing and quantum information it is possible to study the spectroscopy of single atoms and molecules. Traditionally, measurements on molecular ions were performed in discharges, ion beams, or in ion traps equipped with buffer gas cooling (> 10 K), limiting measurements to low resolution due to considerable Doppler broadening [1]. Additionally, spectral line data for molecular ions is limited, as most molecular spectroscopy to date has been performed using beams of neutral atoms. By co-trapping a molecular ion and sympathetically cooling it with a laser cooled atomic ion, the Doppler broadening of previous work will be eliminated and higher-resolution experiments can be conducted. This thesis is meant to be a guide to designing and constructing the necessary components to implement such spectroscopy, describing novel techniques for identifying molecular ions and performing spectroscopy, as well as diagnosing potential pitfalls within the experiments.

1.1 Ion Traps

In 1936, Frans Michel Penning added an axial magnetic field to an electric discharge in an attempt to increase the path length of discharge electrons [2]. In 1953, Wolfgang Paul invented the non-magnetic quadrupole mass filter, and in 1959, micron sized charged particles of iron and aluminum were trapped in a confined region of space with a closed form of Paul's electric mass filter [3]. Even then it was realized that this variation on the mass filter could be used to suspend any charged particle (e.g., charged dust, ions, electrons, etc.) in dynamic equilibrium [3]. Later, Penning's experiment would inspire Hans Dehmelt to combine an axial magnetic field with a

quadrupolar electrical field as a way to confine charged particles. From these innovations came the modern day Penning and Paul ion traps [2]. In the decades since, ion traps have become vital tools for experiments in both chemistry and physics. Wolfgang Paul and Hans Dehmelt were awarded the 1989 Nobel prize for Physics for their work with ion traps.

Paul traps use a combination of DC and radiofrequency (RF) voltages applied to electrodes to form stable trapping regions. The equations of motion of a charged particle (or ion) inside a Paul trap are governed by a special case of the Mathieu differential equation [3]. The solutions of these equations lead to both stable and unstable zones depending on the operating parameters that are chosen [2]. By manipulating these parameters, ions of a desired mass-to-charge ratio can be confined, while unstable ions will instead collide with the trap electrodes and be lost.

In the 1970s, it was realized that for very high resolution spectroscopy both first- and second-order Doppler shifts need to be eliminated. This goal is not possible unless very few (preferably a single) ions are present in the trap, cooled to temperatures near absolute zero [2]. Initially, trapped ions have energies of order 1 eV ($\sim$ 10000 K). Such large energies lead to large amplitude ion oscillations and greater chance of ion loss. These large amplitudes cause both first-order and second-order Doppler effects; therefore all precise spectroscopic experiments require cooling [2].

Laser cooling and trapping relies on the interaction between laser light and atoms to exert a controllable force on the atom, and many sophisticated schemes have been developed using the special properties of this interaction [4]. When applied, these techniques can increase trapping lifetimes and reduce Doppler broadening [5]. Laser cooled ions in linear Paul traps are an ideal tool for studying gas phase atomic and molecular ions at very low temperatures as well as conventional high-resolution spectroscopy [6, 7, 8]. Trapped ions provide a relatively clean system because they can be confined for long durations while experiencing only small perturbations from the

environment [9]. The tight spatial confinement and ultracold temperatures present in ion traps allow for single particle spectroscopic experiments to be performed with minimal Doppler broadening of spectral lines [10]. The accuracy of trapped ion frequency standards derives in part from this reduced Doppler broadening [11]. The large trapping depth (on the order of eV) and the wide mass acceptance range allows for simultaneous trapping of different ion species. The strong optical transitions of atomic ions allow for rapid Doppler cooling to millikelvin temperatures, and co-trapped molecular ions may be sympathetically cooled to similar temperatures via Coulombic interaction [12].

There are many methods of cooling ions within a trap, including: resisitive cooling, active feedback (stochastic) cooling, collisional cooling (such as by collision with a light-molecular-weight buffer gas, low-energy electrons, or cooling by another species of already cold ions), polarization gradient or Sisyphus cooling (which uses shifts of atomic energy levels induced by a laser field in a multilevel atomic system), cooling by radiation damping (especially by lasers), and sympathetic cooling (direct laser cooling of another species followed by collisional cooling) [13]. The final desired energy is the most important criterion to determine the type of cooling which is most appropriate, but the depth of the potential well in the trap and initial ion energies are also relevant. In terms of overall usage, collisional cooling by a buffer gas and cooling by lasers are the most commonly used techniques [2]; however, this thesis focuses purely on laser cooling. Electric-dipole allowed transitions and dipole forbidden electric quadrupole transitions (which have very long decay lifetimes) can both be used for cooling [14].

1.2 Molecular Ions

Though the field of trapped ions has been around for nearly 60 years, the subfield of cold molecular ions is still in its infancy. In the last decade, research has begun to focus on all that may be possible with the long interaction times provided by ion

traps. From a small handful of experimental groups, there are now several dozen around the world exploring a number of molecules, with goals ranging from chemical reactivity to spectroscopy, and eventually laser cooling of a molecular ion. For proper spectroscopy of a molecular ion there are three major requirements: loading and sympathetically cooling the molecule, identifying the ion of interest, and performing spectroscopy by perturbing the system via a resonant transition.

Atomic spectroscopy experienced a qualitative jump in ultrahigh-resolution spectroscopy after the technique of laser cooling was introduced, and similar enhancements are expected for molecular ions. This is due to the strong suppression of usual line-shifting and broadening effects caused by collisions, high thermal velocities, and finite transit time [13]. Vibrational and rotational levels of suitable molecules have long lifetimes (milliseconds to days), implying potentially huge transition quality factors [13].

Due to the wide mass acceptance of linear Paul traps, a broad array of molecular ion masses can be sympathetically cooled. Molecules can either be loaded directly or through gas phase reactions with the trapped atomic ions, and examples ranging in size from HD^+ to C_{60}^+ have been demonstrated [15, 16]. An ion that can be laser cooled can be used to sympathetically cool another species through the Coulombic interaction between the ions [12, 16, 17, 18, 19, 20, 21, 22]. Sympathetic cooling brings the motion of all trapped ions to the equilibrium temperature of the laser cooled ions [23] in a time proportional to the secular frequency of the trap [24, 25]. Experimental techniques for destructive and nondestructive characterization an analysis of the content of sympathetically cooled ensembles are available. Chemical reactions between cold trapped atomic and molecular ions and neutral gases can be observed and used to determine reaction rates or to produce a variety of molecular ions *in situ*. Simply by monitoring the rate at which the volume of the fluorescing reactant ions were diminished due to reactions, reaction rates could be established by knowing the density of the leaked in gas [7]. At least for simple molecules, high-resolution

rovibrational spectroscopy is feasible even if the internal temperature of the ions is room temperature.

Controlled ensembles of cold atomic and molecular ions have the potential for many applications, including: quantum information processing [26, 27], ultra-high resolution spectroscopy [27, 28, 29, 30, 31], optical clocks [32, 33], nano deposition of dopant atoms in semiconductors [34], and studies of molecular properties and chemical reactions [7, 35, 36, 37, 38, 39, 40, 41, 42, 43, 44]. Fundamental physics experiments with molecules requiring extreme resolution and accuracy include tests of quantum electrodynamics, measurement of and search for a space-time variability of the proton-to-electron mass ratio [45], and the search for parity violation effects on vibrational transition frequencies [46, 47]. Finally, a novel application is the investigation of collisions of molecules with atoms or other molecules at very low temperatures [48]. This temperature regime represents a unique situation for the study of quantum-mechanical defined internal states [49].

There are several methods to produce molecular ions within a Paul trap where they are then sympathetically cooled by a laser cooled atomic ion. A neutral gas can be introduced into the vacuum chamber via a leak valve and ionized *in situ* by an electron beam crossing the trap center [19, 20]. Here the loading rate is controlled by the partial pressure of the neutral gas and the electron beam intensity. It is also possible to ionize a large sample outside of the trapping region (i.e., by electrospray ionization) and then to transfer the molecular ions via an ion guide and additional optics to inject directly to the trap [21]. Ablation loading of atomic ions and using a confined beam of hydrogen has also been demonstrated to produce AlH^+ [50].

As mentioned previously, research has been conducted examining chemical reactions of laser-cooled atomic ions with neutrals. The study of such reactions at even lower temperatures could improve the understanding of ion-neutral reactions occurring in interstellar clouds [13]. The first examples of laser-cooled atomic ions studied

Ca^+ ions with neutral O_2 to form CaO^+ [51]. Generally these reactions require the atomic ion be in an electronic excited state in order to proceed, and are of pseudo-first order since the concentration of the calcium ion can be assumed to be infinite (even though there is only a single atom present!). All of the molecular ions produced for experiments in this thesis were through the reaction of a single laser-cooled calcium ion with a neutral gas at room temperature.

1.3 Molecular Spectroscopy

For sympathetically cooled molecular ions, one wide-ranging application is rovibrational spectroscopy with significantly enhanced resolution and accuracy [13]. Spectroscopy of rovibrational transitions in the electronic ground state can take advantage of the special conditions present in ion traps. The low translational temperature of the molecules increases the absorption rate significantly, and efficient excitation is possible even on weak overtone transitions [52]. Rovibrational spectroscopy via direct molecular fluorescence detection is not feasible for a large class of molecular ions. The corresponding low fluorescence rates would require sophisticated photon counting systems, if fluorescence could be detected at all, which may not be practical. Instead, resonance enhanced multiphoton dissociation (REMPD) has been used [13]. Unfortunately, since the spectra is obtained by repeated molecular ion production and interrogation cycles it necessarily requires destruction of the molecule of interest.

Preliminary work has been done with REMPD on certain overtone lines in CaH^+ with promising success. Due to the relatively long lifetimes of vibrational levels of molecules ($\sim$msec to days), the potential line resolution can be huge. Spectroscopy of vibrational transitions on cold and localized samples of molecular ions was first achieved using HD^+ ions [13, 53].

While REMPD is the current standard for obtaining vibrational spectra of trapped ions, advances in new methodology (such as those proposed in Chapters 6 and 7)

could lead to repeated spectroscopy of a single molecule. Nondestructive techniques are made possible by using atomic ions as probes. The fluorescence of the Doppler cooled atomic ions can be observed by a CCD camera, allowing the presence of non-fluorescing molecular ions to be inferred from the positions of fluorescing ions. The molecular ion can then be perturbed with a probe laser, and this perturbation can be mapped onto the coolant atomic ion's fluorescence via the Coulombic interaction between the two ions.

One interesting aspect of this spectroscopy is the dependence of vibrational and rotational transition frequencies on the ratio of electron mass to the mass of the nuclei [13]. In the simplest case, a diatomic molecule, the fundamental vibrational and rotational transition frequencies scale as:

$$v_{vib} \sim \sqrt{m_e/\mu} R_\infty, \; v_{ro} \sim m_e/\mu R_\infty. \tag{1}$$

Here, μ is the reduced mass of the two nuclei and R_∞ is the Rydberg energy. Proposals suggest that vibrational spectroscopy of CaH^+ could demonstrate time-dependence of the ratio of electron to nuclear mass (β) [54]. It has been predicted that a possible variation of m_e/m_p (and of the quark masses and the strong interaction constant) over time might be larger than a possible time variation of the fine structure constant, α [55, 56, 57]. Variations in α and β provide important information for the development of theories beyond the standard model [54]. As each atomic transition has a different dependence on α, variation in α can be detected by measuring the variations in the ratios between different atomic transition frequencies. However, it is difficult to detect variations in β with atomic transitions, because the electronic energy states depend only weakly on the nuclear mass. In contrast, the vibrational and rotational transition frequencies in molecules are proportional to $\beta^{-1/2}$ and β^{-1}, respectively. Recently, an indication of a variation of m_e/m_p over billion-year timescales was reported [58]. Initial REMPD experiments will help to identify vibrational transitions within the molecular ion so that future experiments may probe the fundamental

physics.

Resonance enhanced multiphoton dissociation (REMPD) works by first populating a vibrational state of the molecular ion that is otherwise unpopulated under normal experimental conditions. A second laser can then selectively dissociate the molecule. The consequent loss of molecular ions from the trap is interpreted as a signature of the first photon being on resonance. By using a multitude of controls, including locking the relevant diode laser to a stable frequency comb, 2-ppb relative frequency resolution has been demonstrated [15].

REMPD, in combination with LCFMS, can be used to gain high resolution spectral information as demonstrated with a crystal of HD^+ and Be^+ ions [15]. First, a vibrational overtone line was excited in HD^+ with an IR diode laser locked to a stable frequency comb. An UV laser then transferred the excited population to a dissociative state. The HD^+ population decay can then be monitored by observing the Be^+ fluorescence. The resulting spectral line had a width of 40 MHz, dominated by Doppler shifts due to the micromotion (driven motion) inherent in large crystals in a RF ion trap. Recently, the same rotational state selective dissociation spectroscopy technique has been utilized to map the state populations of translationally and vibrationally cold molecular ions and achieve a high degree of rotational cooling [59, 60, 61].

Narrower linewidths can be achieved by limiting the ions to a linear chain. Quantum Logic Spectroscopy (QLS) transfers information between two trapped ions, a logic ion and a spectroscopy ion, through the quantized vibrational motion of the crystal. The logic ion serves as a quantum sensor for detecting transitions in the spectroscopy ion [27]. The reported absolute frequency measurements on single trapped ions using QLS have been performed on narrow transitions [32, 33] where the secular frequency of the ions in the trap exceeded the transition linewidth. In this strong-binding limit [62], the absorption spectrum consists of a carrier and a number of motional

sidebands separated by the secular frequency. Initialization in QLS experiments requires cooling of the vibrational modes of the crystal to the ground state, which is achieved by addressing the motional sidebands [63].

Quantum logic spectroscopy (QLS) was developed to indirectly detect the state of one or more "spectroscopy" ions by coupling them to a "control" ion of a different species [27]. The QLS detection sequence begins by cooling the ions close to the ground state. Subsequent motional sideband transitions implement a quantum gate between the spectroscopy ion and the control ion whose state is then detected. One drawback of QLS is the requirement of ground-state cooling, which adds significant experimental complication. Moreover, QLS cannot be applied in general to complicated atomic systems because it relies on narrow optical transitions in the spectroscopy ion, which must be accessible by continuous-wave laser sources. For most ion systems, such a resonance is unavailable or, through spontaneous emission, leads to dissociation away from the measurement basis [64].

1.4 Sympathetic Cooling

By simultaneously having a laser-cooled ion species trapped together with another ion species, it is possible, through the Coulomb interaction between the two species, to sympathetically cool the whole ion ensemble into a crystalline state [7, 65]. The technique of sympathetic laser cooling can be used to cool any ion species to sub-kelvin temperatures [5]. Sympathetic cooling has the advantage that it does not depend on the internal level structure or on the electric or magnetic moment of the particles, only their mass and charge. The process is equally applicable to both atomic and molecular ions, and has been implemented using a multitude of atomic coolants in both electrostatic and electrodynamic ion traps. Also, this indirect cooling method has the additional advantage that adverse level-perturbing effects caused by lasers are avoided - particularly desirable in spectroscopic experiments [2].

Sympathetic cooling does not cool the internal degrees of freedom of molecular ions. Instead, significant work has been done within the literature in an attempt to prepare molecules in certain rotational states [60, 66]. Shen *et al.* were able to demonstrate the spectroscopy on a dipole-allowed rotational transition in HD^+ ions by utilizing rotational laser cooling to increase their signal. Staanum *et al.* showed a nearly 15-fold increase in the rotational ground-state population of the $X^1\Sigma^+$ electronic ground-state of MgH^+ [60]. The final ground-state population was equivalent to a thermal distribution of $\sim$ 20 K. These advances could bring the benefits of cryogenic temperatures to molecular ion experiments in a room-temperature set-up.

1.5 Spectroscopy with Resolved Sidebands

This thesis describes the use of resolved sidebands of trapped ions to identify co-trapped atoms and molecules with sub-amu precision, to cool a single calcium ion to the ground state of motion, and to monitor the excitation of a second ion via the heating of the cold calcium ion. To achieve these goals required a number of preliminary steps which are outlined in this thesis. Chapter 2 discusses the theory behind trapping and laser cooling atomic ions. Chapter 3 chronicles the process behind the design and construction of the ion traps used, in addition to basics of the experimental setup. Compensation of stray fields is reviewed in Chapter 4. Chapter 5 contains the use of the dipole forbidden $S_{1/2} \rightarrow D_{5/2}$ transition at 729 nm to sideband cool an atomic ion to its vibrational ground state. Chapter 6 discusses mass spectrometry techniques employed by ion trapping experiments, as well as a description of a new method of identification based off of resolved sideband spacing. Chapter 7 describes a new spectroscopic technique developed in the Brown Lab to connect the frequency-dependent laser induced heating of a sympathetically cooled spectroscopy ion with changes in the fluorescence of a laser-cooled control ion. A description of how this technique can be extended to the sideband cooled regime is also discussed. Finally,

Chapter 8 previews future experiments in molecular ion spectroscopy of CaH^+.

CHAPTER II

THEORY OF ION TRAPPING AND LASER COOLING

While a thorough understanding of ion traps and the physics behind their operation is essential to becoming an expert in the field, a complete derivation of the Mathieu equations is not necessary to understand the data presented within this thesis. As such, the reader is advised to examine any of a number of fine resources [2, 67] for further investigation; here we will present only a brief discussion.

2.1 Operation of Ion Traps

Linear Paul traps operate by creating an oscillating electric quadrupole field between an array of four opposing electrical poles. The shape of the electric field is a function of the geometric arrangement of these four surfaces and the magnitude of the DC potentials. This field is generated by RF potentials applied to two opposing electrodes, creating two-dimensional confinement of the ions (x- and y-directions). Axial confinement along the axis of cylindrical symmetry (z) is achieved by potentials applied to the separate endcap electrodes [68].

RF voltages are necessary because the electric potential required for trapping is a saddle potential; this is a manifestation of Earnshaw's theorem which states that electrostatic potentials cannot have local minima or maxima in freespace [69]. Therefore, a charged particle can not be held by electrostatic forces alone, because any set of potentials that bound a charged particle in two dimensions would necessarily cause the particle to be unbounded in the third dimension.

The saddle potential in the region between the electrodes can be written as:

$$\mathbf{\Phi}(\mathbf{r},t) \;=\; \phi(t)\frac{y^2-x^2}{2r_0^2} \tag{2}$$

where r_0 is the effective radius of the trap. Ion motion within the trap can be described by the Mathieu equation:

$$\frac{d^2u}{d\xi^2} + (a - 2q\cos 2\xi)u \;=\; 0 \tag{3}$$

with variables, a and q, defined by:

$$a = \frac{4QU}{mr_0^2\Omega_{RF}^2};\; q = \frac{2QV}{mr_0^2\Omega_{RF}^2}, \tag{4}$$

where U is the DC bias on the RF electrodes (if any), V is the amplitude of the RF potential, and Ω_{RF} is the RF angular frequency. Not included in the Mathieu parameters but also relevant for Paul traps is the distance from the center of the trap to the apex of the endcap electrode, z_0. This set of equations has been studied in detail in the literature [2, 70], and it is known that depending on a and q there are stable and unstable solutions. Stability diagrams in (a,q) space can be used to indicate which conditions give rise to stable/unstable solutions [3, 68].

If the quadrupole is operated with a and q parameters that give stable trapping in both the x- and y-directions, the ion is said to have a stable trajectory and may be held without loss. For operation outside of this region in (a, q) space the trajectories are unstable in x, y, or both, and the ions are lost. For the experiments presented here, no DC bias is added to the RF drive, so the stability region is specified along the abscissa (the a parameter is assumed to be very close to 0 by setting U $\equiv$ 0). This gives stable trapping for $0 < \mathrm{q} < 0.908$.

It has been shown that the Mathieu q value should be low in order to efficiently realize laser cooling and to suppress RF heating [6, 71]. Furthermore, the Mathieu equation describes only the motion of a single ion and does not include the effects of a large number of ions, isotopes, and laser cooling. The motion of an ion is generally complex, but when $q < 0.4$ a single ion not too far from the trap center will feel an effective harmonic potential (pseudopotential) [3, 7]. Parameters for V and Ω_{RF} are chosen so that the q value for $^{40}Ca^+$ is between $0.3 - 0.4$, allowing heavier isotopes

and molecules (with smaller q values) to remain within the trapping region. When working with ions of different masses, especially molecular ions which may be much more massive than their atomic counterparts, it is important to be cognizant of the respective q values as it is important to know areas where all of the ions are stable, not just the main cooling ion.

At any position in time, the ion's velocity can be decomposed into harmonic motion with frequency ω_i, called *secular motion*, and an amplitude modulated fast driven motion with frequency Ω_{RF}, called *micromotion* [72]. The solution, when stable, will consist of a slow vibration upon which is super-imposed a smaller ripple due to the drive. When the particle is stably bound, the micromotion is 180° out of phase with the drive. Then, in the absence of any applied DC fields, the trap can be thought of as providing the ion with a harmonic pseudopotential well, undergoing simple harmonic motion at the secular frequencies [5]. The micromotion term arises from the ion sampling fast, driven motion at the RF frequency [2]). The axial secular frequency of the ion is given by:

$$\omega_z = \sqrt{-2a_{end}}\frac{\Omega_{RF}}{2},\ a_{end} \ = \ \frac{4Q\kappa U_{end}}{mr_0^2\Omega_{RF}^2} \tag{5}$$

where U_{end} is the DC endcap voltage and κ is a geometric factor. The radial secular frequencies are defined by:

$$\omega_x = \omega_y = \frac{QV_0}{\sqrt{2}mr_0^2\Omega_{RF}}. \tag{6}$$

The depth of the trap is a measure of the confining strength, or maximum energy an ion can obtain before escaping. An ion trap has well-depths in the radial (r) and axial (z) directions, given by [5]:

$$\bar{D_r} \ = \ \frac{qV^2}{4mr_0^2\Omega^2} \ = \ \frac{\bar{D_z}}{2}. \tag{7}$$

Common trap depths for the ion traps used in this thesis are on the order of several eV. The effect of a DC bias (external field) would be to alter the well depth along

the direction of the applied field, and could lead to the ion trajectories becoming unstable.

2.2 Principles of Laser Cooling

One of the characteristics of optical control of atomic motion is that the speed of atoms can be dramatically reduced. Since the spread of velocities of a sample of atoms is directly related to its temperature, the field has been dubbed laser cooling [4]. Use of the term "cooling" does not imply that the ions are in thermal equilibrium with each other nor that they have a well-defined temperature, but rather that the velocity of the ion is reduced [5]. The first example of ions laser-cooled in a Paul trap was in 1978 in an experiment by Neuhauser *et al.* [73] where 50 Ba^+ ions were confined in a miniature trap and laser cooled. They were first collisionally cooled by helium buffer gas [2].

2.2.1 Saturation

The ultimate resource for laser cooling and trapping is the book by the same name by Metcalf and van der Straten [4]. The reader is advised to utilize that reference for a proper derivation of the saturation parameter and for further reading on the topic. The absorption or scattering of radiation is described as a reaction or scattering process and the probability of absorption or scattering is given in terms of a cross section [74]. When discussing intensity of lasers, saturation is the more relevant parameter (instead of directly measured power), as knowledge of a laser power is irrelevant without a proper beam size measurement. The more relevant parameter in lab is the saturation intensity, given by:

$$I_s \equiv \frac{\pi hc}{3\lambda^3\tau} = \frac{\pi hc\Gamma}{3\lambda^3} = \frac{\pi hcA}{3\lambda^3}. \tag{8}$$

Here the lifetime of excited state is defined as $\tau \equiv 1/\Gamma$, where Γ is the rate of decay, and A is the Einstein coefficient for spontaneous emission, related to the "strength" of

a transition. For Ca^+, the saturation intensities for the main transitions in this text are: $I_{sat,397} = 465.977\ W/m^2$, $I_{sat,866} = 3.393\ W/m^2$, and $I_{sat,729} = 6.976 \times 10^{-7}\ W/m^2$. This is a parameter with physical meaning in lab, since power and beam size can easily be measured.

2.2.2 Lamb-Dicke Regime

When ions are localized to spatial dimensions smaller than the optical wavelength of the laser they are said to be within the Lamb-Dicke regime [75]. Comparing the size of the ion's wave function, Δx, and the laser wavelength, λ, allows for the characterization of the Lamb-Dicke parameter

$$\eta \equiv k\Delta x = 2\pi\Delta x/\lambda = \sqrt{\hbar k^2/2m\omega_v}. \tag{9}$$

If the ion is confined to the Lamb-Dicke regime:

$$\eta \ = \ k_{i,j}/\sqrt{\hbar/2M\omega_v} \ll 1. \tag{10}$$

In other words, for $\eta < 1$, interaction with higher-order sidebands gets weaker for smaller values of η [75]. The wave vector k associated with monochromatic radiation of wavelength λ is $k = 2\pi/\lambda = 2\pi\nu/c = \omega/c$, where ω is the angular frequency of radiation [2].

For a tightly bound atom, a more natural energy scale is given by the quantized vibrational level, n, where the energy for an atom confined in a harmonic potential of frequency ω_v is:

$$E \ = \ \hbar\omega_v(n + 1/2). \tag{11}$$

In this case, the fundamental cooling limit is the $n = 0$ zero-point energy of the binding potential [63]. Attainment of the 3D ground state is significant as it is the fundamental limit of cooling for a bound atom and approaches the ideal of an isolated particle at rest [63]. In the Lamb-Dicke regime, both stimulated and spontaneous processes are unlikely to change the vibrational quantum number, which is important

in the context of sideband cooling. In order to satisfy the Lamb-Dicke criterion, the motion of the ion must first be cooled to a small vibrational state [76].

2.3 Doppler Laser Cooling

The weak binding limit is defined as the region where the trap drive frequency, Ω_{RF}, is much lower than the decay rate, Γ, of the transition being used for cooling. This implies that the sideband spacings are much smaller than the natural linewidth of the transition. Due to the confining potential of the trap, the velocity of the ion changes much more slowly than the timescale it takes for the ion to absorb or emit a photon. Therefore, these processes can be assumed to change the momentum of the ion instantaneously [76]. This is best demonstrated by Doppler laser cooling.

The notion of a "virtual level," as opposed to a "real level," is encountered when dealing with a nonresonant atomic (or molecular) excitation process - a process for which there is a mismatch, or detuning, between the atomic energy difference ΔE, and the excitation energy $\hbar\omega$ [77]. Doppler laser cooling is achieved by repeated absorption and spontaneous-emission cycles on a closed optical transition, whereby the transfer of momentum upon the absorption of a photon is used to slow down the atoms [4, 8]. Cooling can be achieved by slightly red-shifting the frequency of the laser beam with respect to the optical transition frequency.

The energy of the secular motion can be reduced by cooling the ion, and as the amplitude is reduced the micromotion and its corresponding energy are also reduced. The lowest translational temperature which can be achieved via Doppler cooling, due to secular motion in one direction, is the characteristic temperature corresponding to the energy associated with the natural linewidth of the atomic cooling transition. It is given by:

$$T_D \approx \frac{\hbar\Gamma}{2k_B}, \tag{12}$$

where Γ is the linewidth of the laser-cooling transition. Because it corresponds to the

limit of the laser cooling process, it is often called the Doppler limit. The minimal temperature results from balancing the cooling due to dipolar forces and recoil heating due to scattering of light [75]. For the 397 nm cooling transition in Ca^+, the Doppler limit is 540 μK.

2.4 Detection of the $S_{1/2} \leftrightarrow D_{5/2}$ transition

As early as 1986, Blatt *et al.* suggested that with a narrow-band source it would be possible to perform extremely high-resolution spectroscopy on the $D_{5/2}$ level [78]. They proposed that it would be necessary to alternate the Doppler cooling lasers and the spectroscopy laser in order to avoid AC Stark broadening of the narrow transition, and that the narrow-laser pulse would ideally approximate a π pulse (on resonance) to invert the population [78]. Such spectroscopy would be free from Doppler shifts to all orders (because of sideband laser cooling) and would not be subject to collisional or transit time broadening. In fact, with adequate magnetic shielding, the principal broadening mechanism would be the laser linewidth. Even with an extremely low optical transition rate, virtually every transition to the metastable level would be detected due to the electron shelving technique [78].

2.4.1 Quantum Jumps

In 1913, Bohr suggested that the interaction of light and matter happens in such a way that an atom undergoes instantaneous transitions of its internal state upon the emission or absorption of a photon [79, 80]. These transitions have become known as "quantum jumps," an artifact of Bohr's model of the atom [80]. The typical concept for this observation is based upon a weak absorption line, coupled, via the ground state or a metastable state, to a strong resonance line in a V shaped three-level system of an individual atomic particle.

The narrow transition at 729 nm makes initial laser alignment more difficult than with the Doppler cooling lasers. Instead of increased fluorescence counts, it is now

easier to detect dips in fluorescence. A first step in finding the $S_{1/2}$-$D_{5/2}$ transition frequency does not require the 729 nm laser to be stabilized with a cavity. Instead, quantum jumps can be observed by monitoring the quenching of the resonance fluorescence at 397 nm of individual trapped ions when they are put into a level not affected by the laser light which excites the ion [80, 81]. Successful excitation at a fixed laser frequency can be been monitored via the induced dark periods (quantum jumps) in the UV fluorescence light. Whenever the atom is excited to the metastable level, the UV fluorescence stops until a quantum jump to the ground state is made [82].

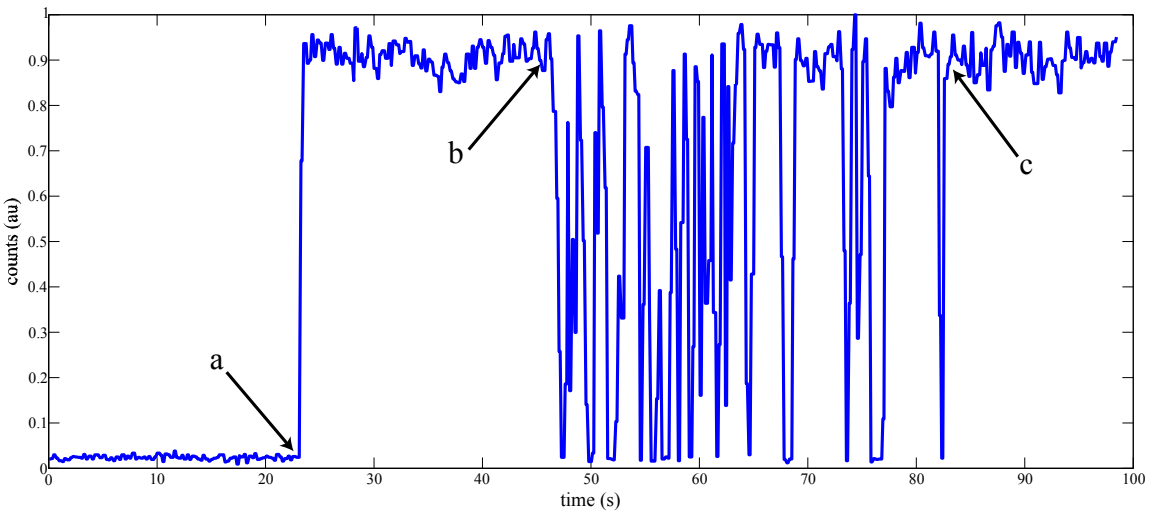

Figure 1: Quantum jumps, or blinking, in the 397 nm fluorescence caused by excitation at 729 nm. The scan begins with only 397 nm light present (the 866 nm laser is blocked) so only background scattering is observed. When the 866 nm repumper is unblocked (a) the ion fluoresces normally. Turning on the 729 nm laser (b) allows for observation of quantum jumps, which are then extinguished (c) when the 854 nm laser is applied.

On the strong line (397), resonance fluorescence is laser excited, leading to continuous photo-scattering. Occasional excitation of the weak transition (729), and the concomitant presence of the atomic system in the corresponding upper state, will

initiate immediate quenching of the strong resonance fluorescence. Since the absorption of classical radiation involves the excitation and synchronization of the induced atomic dipole, the response may be slightly less abrupt [80]. It is possible to coarsely align the 854 nm laser once quantum jumps have been observed. Having the 854 nm laser near resonance will eliminate all jumps since any population transferred to the $D_{5/2}$ level will immediately be transferred to the fast-decaying $P_{3/2}$ level.

2.4.2 Electron Shelving Technique

The strong fluorescence on the 397 nm transition is a monitor of the quantum state of the atom, termed electron shelving by Dehmelt [78, 81]. The technique requires an atom with two excited states, both of which are radiatively coupled to the same ground state but with vastly different transition rates [78]. The strong transition fluoresces brightly, allowing it to serve as a probe of the ion's state, and can also be used for cooling. If the highly metastable state has a lifetime longer than the detection time, a transition to it will result in the complete suppression of the strong resonance fluorescence during that window. The resulting loss of fluorescence photons produces an easily observed signal. Thus, the transition to the metastable level can be detected with near-unity fidelity, providing robust detection of forbidden optical transitions in an individual ion [78, 81].

For calcium, after incidence of the 729 nm light, the quantum state of the ion is interrogated using the 397 nm laser; if the clock transition has not occurred, the ion fluoresces at 397 nm, otherwise it does not fluoresce because the ion is "shelved" to the meta-stable $D_{5/2}$ state [83]. If the collected 397 nm fluorescence exceeds a preset value during the measurement time, it is assumed that the ion was laser cooled and cycling between the $S_{1/2}$ and $P_{1/2}$ states [84]. This very sensitive method of detecting weak transitions works because, temporarily, the optically active electron is stored on another energy level [2]. The measurement cycle is repeated many times for statistics

before setting the probe laser to a different frequency and repeating the experiments all over again [85].

By using photon counts it is possible to distinguish between "bright" and "dark" numbers of counts using histograms. Many experiments ($\sim 50-100$) are run, binning the data into a histogram (Figure 2). Bright and dark peaks are obtained by blocking or unblocking the 866 nm laser with an ion present. Dark counts exist due to 397 nm scatter. It is preferred to have the shortest measurement time that still gives well resolved peaks for bright and dark. The peaks need to be well resolved so that a threshold value can be determined for shelving experiments. During a shelving experiment, counts are compared to the histogram values to determine if the ion was in the bright or dark state. For the majority of the one ion experiments, 2 ms was used for detection due to clear separation. For experiments using two bright ions it is important to take new histogram measurements for proper separation of one and two bright ion counts.

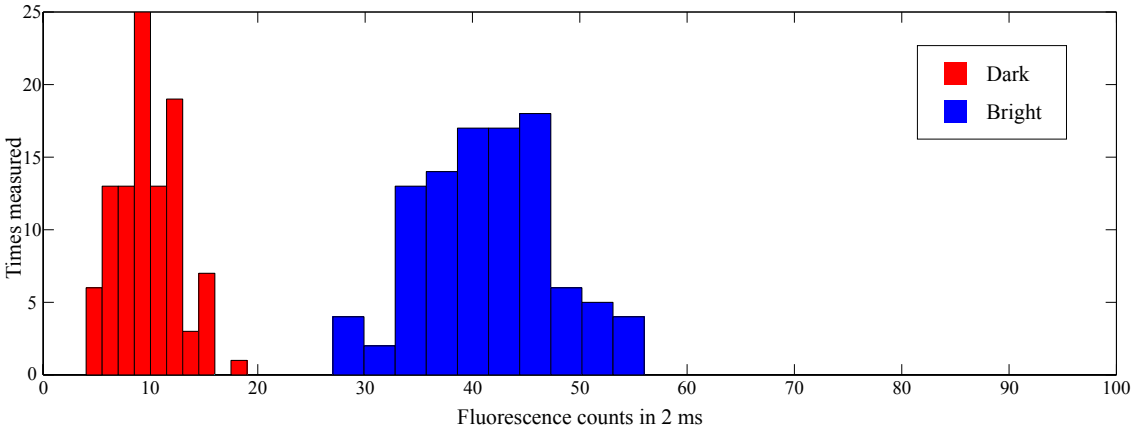

Figure 2: Histogram showing dark and bright peaks with a 2 ms measurement time.

2.5 The Zeeman Effect

In the absence of any applied magnetic field, the Zeeman sublevels are degenerate. Application of an external field lifts the degeneracy, splitting each atomic state with

angular momentum j into $2j+1$ states [4]. The projection of the angular momentum along B is equal to $m_j = -j, -j+1, ..., j-1, j$. At low fields the energy level shifts ΔE are proportional to the field strengths according to $\Delta E = g\mu_B B m_j$, where $\mu_B \equiv e\hbar/2m_e c$ is the Bohr magneton, and g is the Landé g-factor. A table of the Landé g-factor values for the different energy levels in calcium is given in Table 1.

Table 1: Landé g-factor values for calcium energy levels

	$S_{1/2}$	$P_{1/2}$	$P_{3/2}$	$D_{3/2}$	$D_{5/2}$
g_j	2	2/3	4/3	4/5	6/5

A magnetic field of approximately 0.36 mT (3.6 G) is applied perpendicular to the direction of propagation of the 729 nm laser. This is still in the low field regime, as the high field limit for Ca^+ is several orders of magnitude larger. This field strength was chosen to provide sufficient separation between the Zeeman sublevels to easily resolve them, while being small enough to not degrade Doppler cooling.

2.5.1 Normal Modes and Motional Sidebands

Multiple ions confined in a linear configuration interact via the Coulomb force, so their motion will be strongly coupled. The ions' oscillations are best described in terms of normal modes, each of which can be treated as an independent harmonic oscillator [11]. The lowest mode is the center-of-mass mode (ω_c), in which the ions oscillate as if rigidly clamped together [11]. The second mode corresponds to each ion oscillating with an amplitude proportional to its equilibrium distance from the trap center, called the breathing mode [14]. The breathing-mode angular frequency scales as $\omega_b = \sqrt{3}\omega_c$.

Once a 729 nm frequency scan across the Zeeman levels has been obtained, it is possible to zoom in on the respective transitions to monitor the motional sidebands (as shown in Chapter 5). Even without proper optimization of alignment or polarization,

laser alignment can be improved by changing the interaction time of the laser on resonance with a carrier transition and monitoring shelving (referenced as a Rabi scan since it provides information on the Rabi frequency); continuing to align the 729 nm laser with blinking/quantum jumps is not sufficient. This experiment allows for small variations to be made showing increases or decreases in the Rabi frequency corresponding to alignment.

CHAPTER III

EXPERIMENTAL SETUP

3.1 Ion Traps

Experiments reported in this thesis make use of Paul traps, specifically as used in spectroscopic experiments. Ion traps are useful tools for spectroscopy because the ions can be held for long periods in a well-controlled environment. The three traps utilized here are similar in that they are linear Paul traps, but with distinct differences explained below. The traps to be described are the Urabe, Berkeland, and Goeders traps, each named for their designer. This chapter also discusses basic information about the laser systems, vacuum chambers, and imaging optics. Though much of the equipment used is standard for all ion trapping experiments, a fundamental understanding is still necessary.

3.1.1 Urabe Trap

The Urabe trap, used exclusively in the experiments described in Chapter 7, was machined at Osaka University under the supervision of Professor Shinji Urabe. The trap is a five-segment version of the three-segment trap characterized in Ref. [86] and a duplicate of the trap used in Ref. [87, 88], with $r_0 = 0.6$ mm and $2z_0 = 4$ mm. The RF electrodes are made of stainless steel plates with a thickness of 1 mm, and the plates are mounted on insulation spacers. Compensating DC voltages are applied to a compensation rod, which runs the length of the trap, and the center segments of the segmented electrodes to minimize ion micromotion [89]. The top compensation rod was removed to avoid blocking any ion fluorescence, though this was done before an ion was ever trapped and was probably unnecessary.

The trap is housed in a 4.5" spherical octagon vacuum chamber at 1.3×10^{-8}

pascals. It is driven at $2\pi \times 14.5$ MHz achieving secular frequencies for $^{40}Ca^{+}$ of $\omega_z = 1.01 \times 2\pi$ MHz and $\omega_r = 1.4 \times 2\pi$ MHz. A schematic of the trap is shown in Figure 3, and an image of the Urabe trap in the vacuum system can be seen in Figure 4.

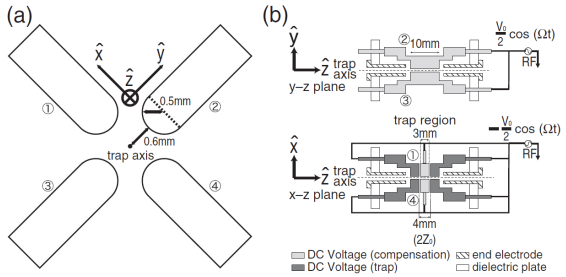

Figure 3: Schematic from Ref [86] of a three-segment version of the five-segment linear Paul trap used in the Atomic Chamber. On the left side is the cross section of the RF electrodes with the shape of the electrodes in x-z and y-z planes displayed in the image on the right.

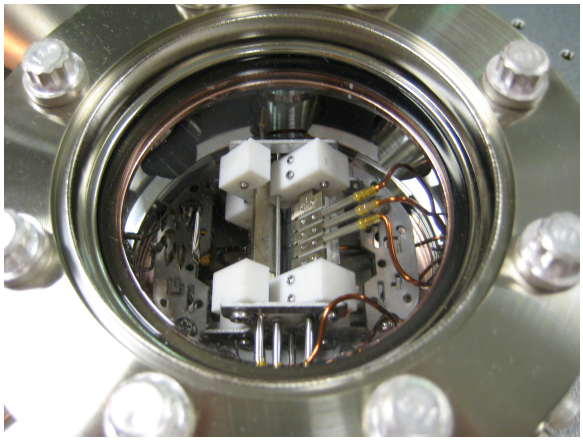

Figure 4: View of the Urabe trap within the vacuum chamber used in the Sympathetic Heating Spectroscopy experiments. The oven used for storage and sublimation of neutral calcium is visible just to the left of the ion trap.

3.1.2 Berkeland Trap

Although ion trapping experiments can be highly technical, they do not require a precisely machined ion trap to be performed. Ion traps can instead be made with little actual machining using parts bought directly from manufacturers. The Berkeland trap

was initially designed as an ion trap that could be simply constructed almost entirely with commercial, off-the-shelf components [90]. A schematic of the trap is shown in Figure 5.

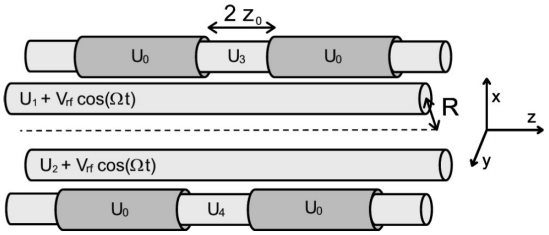

Figure 5: Schematic of the trap described in Ref [90]. Image is taken directly from the text of that reference. U_0 are the endcaps used for axial confinement.

The description that follows is for a trap built based upon the Berkeland trap design. All electrodes are made of 316 stainless steel (McMasterCarr) and consist of four hollow rods (OD = 0.813 mm and ID = 0.508 mm). RF is introduced onto two diagonally opposed rods while the other two rods are grounded (U3 in Figure 5) during experiments (but could be used for micromotion compensation). For axial confinement, two slightly larger diameter hollow rods (OD = 1.067 mm, ID = 0.889 mm) are placed over the smaller rods spaced 6 mm apart ($2z_0$) to serve as endcaps. Electrical connections are provided by spot welding 0.25 mm stainless-steel wire onto tabs on the endcaps (Figure 6). The larger rods are cut with a Dremmel tool to a length of 1 cm. Polyimide tubing (Small Parts, Inc) is used to electrically isolate the endcaps from the grounded rod. Unfortunately, the polyimide tears easily and it can be difficult to keep the larger endcaps in place over the polyimide. The original Berkeland trap used friction to hold in place the tightly fitted parts, but we found it necessary to use Torr-seal epoxy to adhere the endcaps onto the polyimide (Figure 6). It is also important to ensure that polyimide is not present in the trapping region where charges may build up, modifying the trapping potentials. Electropolishing the smaller rods was useful before trying to slide the thin polyimide over the electrodes.

To simplify construction, the Berkeland design was modified to include two Macor

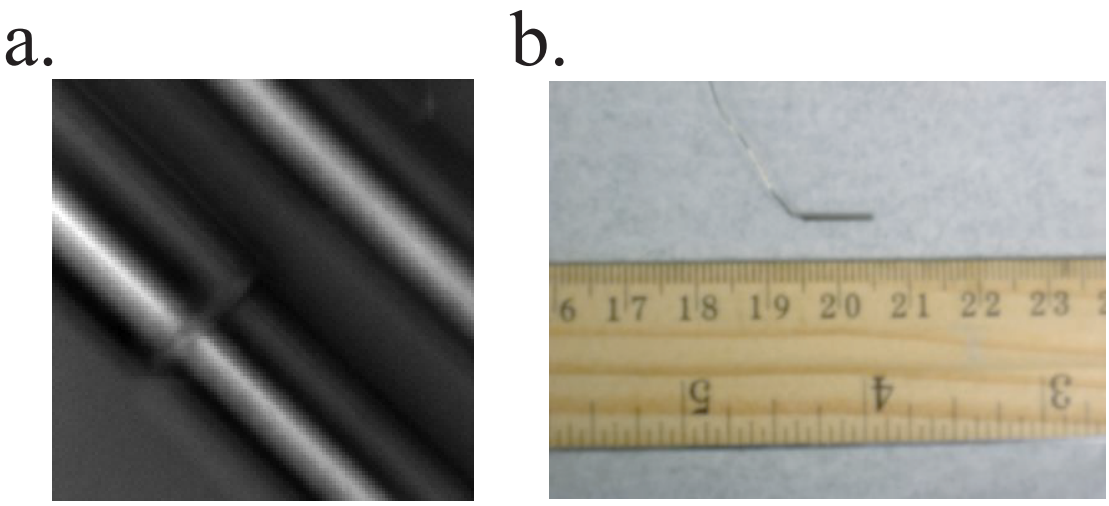

Figure 6: Endcap wiring and polyimide. (a) Image of the top endcap viewed from the CCD. (b) The endcap with spot welded wire.

cubes to align the rods and set the distance between the rods and the center of the trapping region (r_0 = 0.5 mm). Though Macor is a ceramic that works well as an insulator, the material is difficult to machine, and several cubes were broken during installation. For future iterations, a different material should be considered (perhaps polyether ether ketone or alumina). Alternatively, the spacing between the rods could be increased so as to not require such thin walls be machined in the ceramic. Stainless steel end pieces were also machined to hold the cubes in place. These rounded plates were then suspended in the central part of the vacuum chamber by long threaded rods which screwed into groove grabbers (Kimball Physics) placed in opposing viewports of the chamber (the long threaded rods can be seen in Figure 11). Another improvement to this design would be to attach the end pieces to the chamber with a breadboard, eliminating the sag allowed by long threaded mounting rods. A mock-up of this proposed design is shown in Figure 7.

While there are design flaws in the configuration that was used, they are simple enough to correct in subsequent builds. This trap can be constructed in only a few

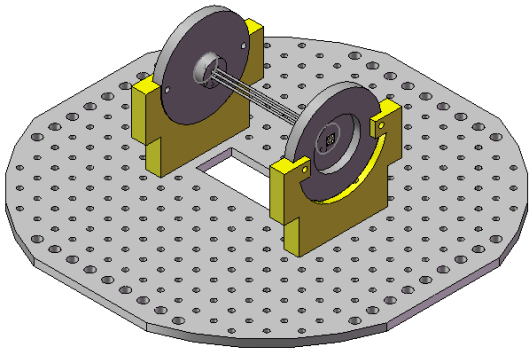

Figure 7: Proposed modifications to the implemented Berkeland-style trap.

days with parts on hand, much faster than the time required to machine components. It certainly has uses in experimental groups trying to build a macro trap cheaply or quickly, such as a group that plans to use planar traps exclusively but need a test trap for initial loading, or undergraduate universities where funding is scarce.

3.1.3 Goeders Trap

After difficulty loading ions with newer versions of the Berkeland trap (including failed attempts to include a lens into the apparatus) it was decided to design and machine a new ion trap. The goals for this ion trap were to make it easy to introduce molecular ions, to maintain large trapping depths so that collisions would not lead to ion loss, and to maintain sufficiently low heating rates to reduce Doppler broadening of transitions. The idea of being able to trap in distinct trapping zones and then merge different ions together, often accomplished in planar ion trap experiments [91], was also an inspiration for the trap design. By changing the operating voltages of these traps, it is possible to confine a few ions in each zone, or shuttle ions between zones. Multi-zone traps also permit isolated cooling, and one could imagine different massed atomic ions being used to best sympathetically cool the different molecular ions of interest.

At this stage, the Urabe trap had been the most robust ion trap used in the

lab, so many considerations were adopted from its design. The Goeders trap design follows the same segmented form, using insulators to hold the electrodes. Increasing the number of DC electrodes from five to eleven increased the number of distinct trapping regions to five [92]. These additional trapping zones could be used to trap different species in the outer regions and then merge the ions together in the central region. Care was taken to make positioning of the electrodes simple yet robust so as to try and avoid anharmonicities in the trapping potential from poorly aligned electrodes. In the initial design the electrodes were screwed into insulating backing pieces (first made of PEEK), and had ribbed grooves machined into the piece so that the electrodes could slide into place and stay separated. The area of the electrode where the screws were inserted was made thicker to allow for threads to be included (Figure 8).

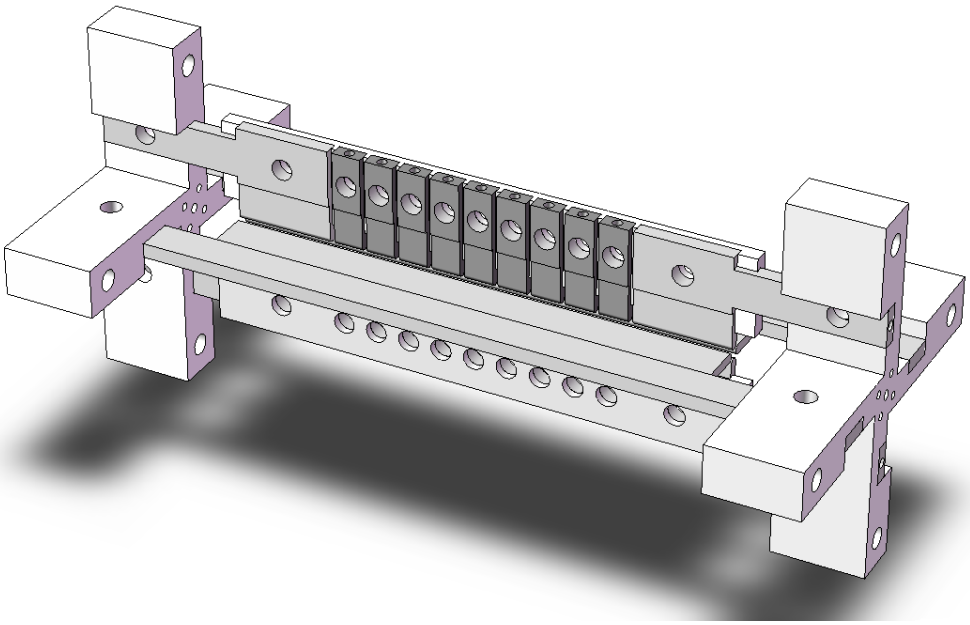

Figure 8: Initial schematic of an 11 segment trap, as fabricated by the GTRI machine shop. No electrical connection pins are shown in the image, but instead the holes in the tops (or side) of the electrode are where the pins would be placed. PEEK components are white, DC electrodes are dark grey (though the endcaps are light grey), and the RF electrodes are light grey.

There were several issues with this ion trap, both in the design and the machining process, so it was never installed in a vacuum chamber. It is unlikely that ion trapping would have been possible even if it had been installed. There were difficulties with aligning the electrodes with the ribbed parts of the PEEK, and upon screwing them in place the back piece began to flex. The pins put in place for electrical connections were added into blind holes so pockets of air were left that would have made proper evacuation of the vacuum chamber difficult. In addition, because the parts were made with electrical discharge machining (which works by removing material from a workpiece by a series of rapidly recurring current discharges between two electrodes), many of the components had surface roughness or other impurities (perhaps oxidation) that were visible to the naked eye, and would likely have resulted in stray electric fields on the atomic scale.

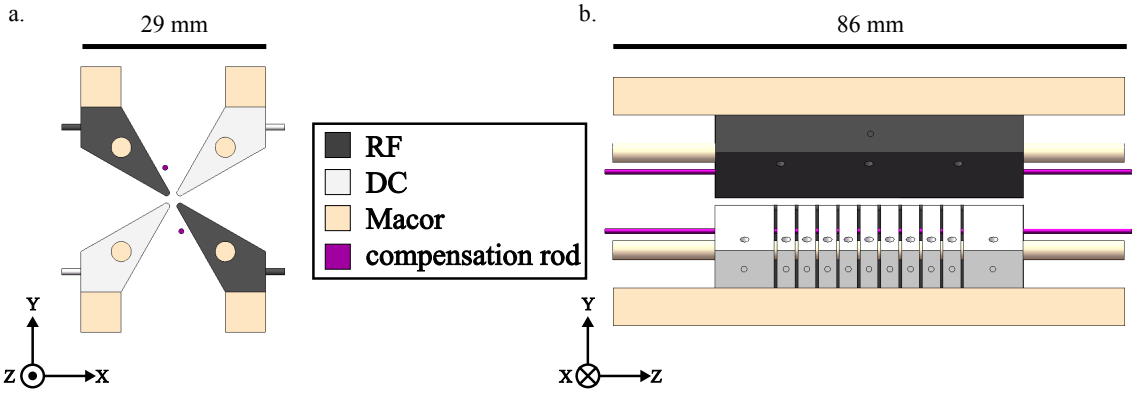

Figure 9: False color schematics of the Goeders ion trap. (a) Axial cross-section of the trap. The RF electrodes are colored dark grey while the DC electrodes are shown in light grey. The small, circular electrodes colored purple are the compensation rods which run the length of the trap. The larger, cream colored circles are the Macor rods used for alignment and stability. Macor blocks are placed along the top and bottom of the electrodes for further alignment. (b) Side view of the trap showing the Macor holders (cream) and the segmented DC electrodes (shown as light grey).

Figure 9 shows schematics for the second version of the eleven segment trap which was used in all of the resolved sideband experiments. Instead of standard 316 stainless

steel, the electrodes were machined from NITRONIC® 50 stainless steel by Wiesmantool, Inc, of Roswell, GA. The switch to NITRONIC® 50 was done because unlike many austenitic stainless steels, NITRONIC® 50 does not become magnetic when cold worked [93].

The idealized quadrupole field is realized when the four-rod structure has a hyperbolic surface [2]. With this in mind, each electrode was designed in a wedge-shape, tapered to a rounded edge with a 0.5 mm radius of curvature. The electrodes are located a distance r_0=1.0 mm from the trap axis. Diagonally opposed RF electrodes span the entire length of the trap (52 mm total). Adjacent DC electrodes consist of nine 3 mm wide segments arranged at 0.5 mm intervals, plus two 10 mm wide endcaps. Additionally, two 52 mm long stainless steel rods of 0.8125 mm diameter are placed 5.15 mm from the trap axis for applying compensation voltages. Macor rods inserted into each electrode run parallel to the trap axis to mechanically constrain the electrodes. Macor bars lay along the top and bottom of the trap and screw into each electrode and the mounted end pieces for further stabilization. No voltage is applied to the end pieces; they connect the trap to the vacuum chamber mechanically and electrically. By altering the dimensions of these endpieces, the distance from the trap axis to the edge of the electrode (r_0) can be controlled with no change to the rest of the trap or the mounting components. End pieces to change r_0 from 1 mm to 2 mm have already been constructed should a future change be desired. Schematics can be found in Appendix A.

Although the trap consists of five distinct trapping regions, only the center region has been used to date. Instead of the standard electrical feedthroughs used on the chamber with the Urabe trap, a 25 pin D-subminiature (D-sub) connector was used to apply DC voltage via Kapton insulated wires to the 22 DC electrodes and 2 compensation rods. This allows low-pass filters to be placed on a printed circuit board directly outside the chamber instead of a cumbersome set of filters on each incoming

line. RF potentials of $V_{RF} \sim 100$ V_{pp} and $\Omega_{RF} \sim 2\pi \times 11$ MHz provide strong radial confinement ($\omega_r = 2\pi \times 1$ MHz). By varying the voltage on the endcaps it is possible to change the axial secular frequencies (Table 2). The cause of the mismatch in endcap voltages is for compensation of residual pseudopotential.

Table 2: Axial secular frequency dependence on endcap voltage

Left Endcap (Fluke 1)	Right Endcap (Fluke 2)	ω_z (MHz)
30	63	0.52
59	124	0.73
118	247	1.04
150	343	1.20

3.2 Vacuum System

The ion traps are housed in vacuum chambers maintained at ultrahigh vacuum. Low pressure is required to avoid ion loss from collisions with residual background gas. The vacuum chambers are constructed from spherical octagons (Kimball Physics) which provide optical access to the ion along each edge. Four octagon ports attach anti-reflection (AR) coated windows, providing axial and radial laser access to the trap. A large viewport directly above the trap is used for fluorescence collection. A 55 L/s ion pump is used to maintain the vacuum of 2.7×10^{-8} Pa. The pumping section of the chamber attaches via a five-way cross, which also houses a hot-filament ion gauge and a residual gas analyzer, for monitoring pressure and background gasses, respectively, as seen in Figure 10.

Electrical connections are wired to various feedthroughs in the vacuum chamber. DC pins connect to a 25 pin CF-flange feedthrough via Kapton© coated wires. A pair of wires connect the RF pins to a feedthrough attached to an octagon port. The molecular vacuum chamber is a 203.2 mm diameter spherical octagon, which is larger than the atomic chamber to allow for a larger ion trap. Future additions could include

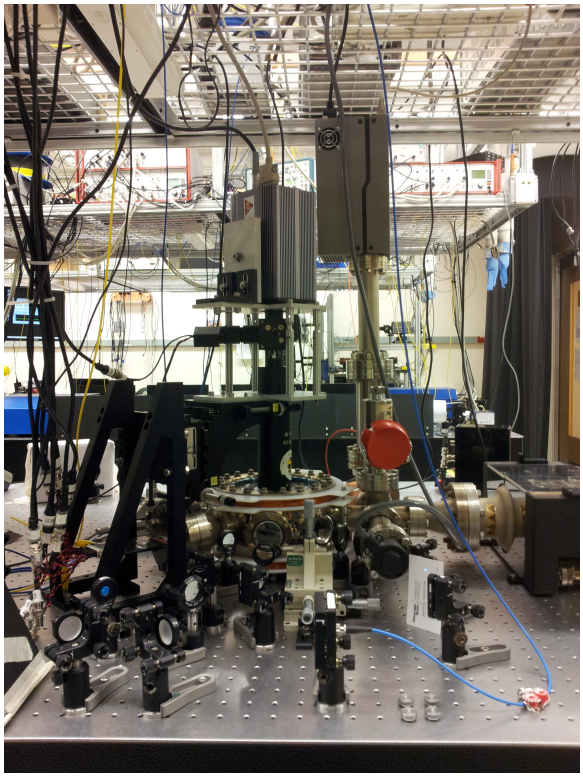

Figure 10: Experiment table with vacuum chamber, optics, camera, PMT, ion pump, and RGA

a Zeeman or Stark slower for reaction rate experiments [8]. The increased volume could also be useful to allow for alternative methods of introducing molecular ions (i.e., housing of ablation targets).

The magnetic field at the center of the trap is controlled by a set of coils arranged in Helmholtz configuration, mutually orthogonal to the **k** vectors of the lasers. The current supplied to the coils was provided by a triple output power supply (Agilent) which has a stability of $0.1\% + 3$ mA ($0.05\% + 1$ mA) for the +6 V (+25 V) configuration [94]. Most experiments were conducted using the +6 V output. The magnetic field value was optimized using the resolved sidebands of the 729 nm transition to prevent spectral overlap.

Molecular ions are formed by inducing a reaction between one of two $^{40}Ca^{+}$ ions initially loaded into the trap and H_2 or O_2 gas introduced into the chamber using a manual leak valve (Kurt J. Lesker VZLVM267). At partial pressures of 2.4×10^{-6} Pa

reactions are observed within 300 s [95]. The leak valve is closed and the experiment begins once the chamber has returned to base pressure.

3.3 Lasers

One advantage of using calcium for ion trapping experiments is that all of the necessary laser diodes for ionization and laser-cooling are commercially available. Using external cavity diode lasers (ECDLs) has many advantages, as they are efficient, reliable, relatively inexpensive, and compact sources of coherent light. Through the use of frequency stabilization techniques, such lasers may be narrowed to < 100 Hz [82]. Furthermore, the intensity noise present in diode lasers can be small compared to other laser systems.

Since all of the experiments described in this thesis depend on ion fluorescence and efficient Doppler cooling, it is important to maintain frequency stability. Unfortunately, the wavemeter (High Finesse WS7) is not a stable reference, so a transfer cavity was built to stabilize the ECDLs to a stabilized HeNe. This is a difficult undertaking since it is necessary to stabilize the frequency of multiple ECDLs at different wavelengths. The cavity was constructed by Ncamiso Khanyile and Gang Shu based on a design previously implemented at the Georgia Tech Research Institute and elsewhere [96, 97]. Many groups have demonstrated frequency stabilization of ECDLs < 2 MHz using similar cavities with a stabilized He-Ne laser [97].

The final and most important laser for resolved sideband spectroscopy is the 729 nm laser. The laser, a stabilized cavity, and all related electronics are housed in a temperature ($\pm 1^{\circ}$C/hour) and humidity stabilized room adjoining the main lab. The laser is locked to a temperature stabilized Fabry-Perot etalon (Advanced Thin Films) via a Pound Drever Hall (PDH) circuit. The idea behind the PDH method is simple in principle: a laser's frequency is monitored by a Fabry-Perot cavity, and this measurement is fed back to the laser to suppress frequency fluctuations. The

measurement is made using a form of nulled lock-in detection, which decouples the frequency measurement from the laser's intensity [98]. An additional benefit of this method is that the system is not limited by the response time of the Fabry-Perot cavity; measurement and suppression of frequency fluctuations can occur faster than the cavity can respond. The etalon is made of Corning Code 7972 and has a finesse of $\sim 100,000$. An electro-optical modulator (EOM) is used for the necessary frequency modulation. A Toptica Fast Analog Lock Circuit (FALC) is used to provide feedback to the laser diode to narrow the linewidth of the laser from ~ 500 kHz to < 1 kHz. The majority of the work done to set up the laser, cavity, and locking electronics was done by Grahame Vittorini, with assistance from Ken Wright and Aaron Buikema. A detailed description can be found in Ref [99, 100].

3.4 Optics

3.4.1 Table Optics

Currently, all of the lasers (except for the 729 nm laser) are housed on a single optics table. Each laser is split into several components so that it can be simultaneously fiber coupled to multiple experimental setups, frequency stabilization optics, and a wavemeter. Optics are used to combine multiple lasers into optical fibers on the "laser" table, simplifying the optics required at the ion trap. In all, the seven lasers on this optical table are sent to the molecular experiment with only three fibers. The combinations include two lasers utilized for photoionization (423 and 377 nm), three near-IR (two 866 nm and an 854 nm) lasers, and the two 397 nm producing lasers (a cavity-enhanced frequency-doubled ECDL at 794 nm with a tapered amplifier at 397 nm (Toptica TA-SHG 110) and a simple ECDL). Because of the low laser light power typically emitted by laser diodes, frequency doubling in an external power-enhancement cavity is a convenient way to achieve greater power in the first-harmonic [82]. The additional 397 and 866 nm lasers are only used during multiple

isotope experiments. Doppler cooling lasers are introduced to the trap 45° off-axis to cool transverse as well as axial modes of the atomic ion.

Also present on the laser table are acousto-optical modulators (AOMs) which are used for fine control of the laser frequency and also fast shuttering. The AOMs are driven by a direct digital synthesizer (DDS) controlled by a programmable function generator. The first DDS controller built in lab had the ability to control three channels (and thus three AOMs) in addition to three transistor-transistor logic (TTL) pulses, and was constructed by Yatis K. Dodia. The second iteration of the DDS controller, designed and constructed by C. Spencer Nichols, increased the number of available AOM channels to five and added greater frequency resolution for one channel to be used with the 729 nm AOM. A complete description of this DDS controller can be found in Reference [101]. The DDS controller contains an FPGA (field-programmable gate array) which stores an instruction set (pulse program) that schedules experimental events. During an experiment, the FPGA controls DDS sources using a high-speed parallel port to reprogram the AOM amplitude, frequency, and phase as well as sequentially triggering devices using TTL pulses. One input pin receives signal from the PMT, allowing for the FPGA to record the number of detected photons during a measurement event. This DDS controller has eight TTL outputs for controlling shutters or RF switches; RF switches are necessary to properly shutoff the output of an AOM to prevent bleedthrough of power and guarantee the lasers are effectively "off."

3.4.2 Fluorescence Optics

When an ion emits a photon it has equal probability of going in any direction. It is not normally possible to detect a single photon with high reliability due to the 4π steradians of solid angle into which the photon is scattered [102]. Of this sphere of fluorescence, it is only possible to collect a small cone due to distance of the optics

from the ion. In order to improve the collection efficiency, a lens system should be designed with the goal of obtaining as large of a solid angle as possible; as such, ideally the lens will be very close to the ion. The imaging optics used were constructed with off-the-shelf components by Curtis Volin of the GTRI QIS group. All of the cameras and imaging optics in lab were setup to be completely vertical. This restricted the total length of the optics since the entire apparatus had to fit in the space between the table and an overhanging shelf. In order to reduce the back focal distance, a telescope was included to reduce the total distance of the lens from 720 mm to 320 mm.

Ion fluorescence is simultaneously collected perpendicular to the incoming light with both an electron-multiplied CCD (EMCCD) camera (Princeton Instruments or SBig) and a photon counter (Hamamatsu $H7360-02$ or Hamamatsu $H10682-210$). A beam splitter directs 30% of the light to the EMCCD to monitor ion position and potential ion loss by distinguishing one bright ion and one dark ion from a single bright ion via position of the bright ion [18]. The Hamamatsu $H10682-210$ has a peak sensitivity at 400 nm (and a count sensitivity of 6.1×10^5 at 400 nm) leading to an improvement over the previously used Hamamatsu $H7360-02$ (centered at 420 nm with a count sensitivity of 4.1×10^5 at 400 nm). Higher collection efficiencies (the number of photons detected of all of the photons emitted by the ion during a set time) are important so that scans can be run faster. The increase in time is due directly to the ability to distinguish bright ion counts from background scatter counts for determining the excited state population. The PMT is also used for compensation of micromotion [90], which is explained further in Chapter 4.

Experimental groups often will include a fast lens mounted near the trap to ensure photon detection in a large solid angle [82]. In the initial Berkeland-style trap reference, the authors included an aspheric lens above the trap, but within the vacuum system, to collect and collimate ion fluorescence [90]. The lens was housed inside of a threaded ring which allowed for fine adjustment of the positioning relative to the

center of the trap. Ideally, the fluorescence from the ions can be collimated inside the vacuum chamber, simplifying the external optics [90]. However, a drawback to placing the lens within the vacuum system (which was also true for the updated design shown in Figure 11) is that by placing a lens inside the vacuum chamber it cannot be adjusted once the system has been sealed. There also exists the probability that charging will occur with the dielectric lens. Unfortunately, no ions were trapped in the Brown Lab with the additional lens in place. Subsequent tests were abandoned in order to construct the trap described in Section 3.1.3.

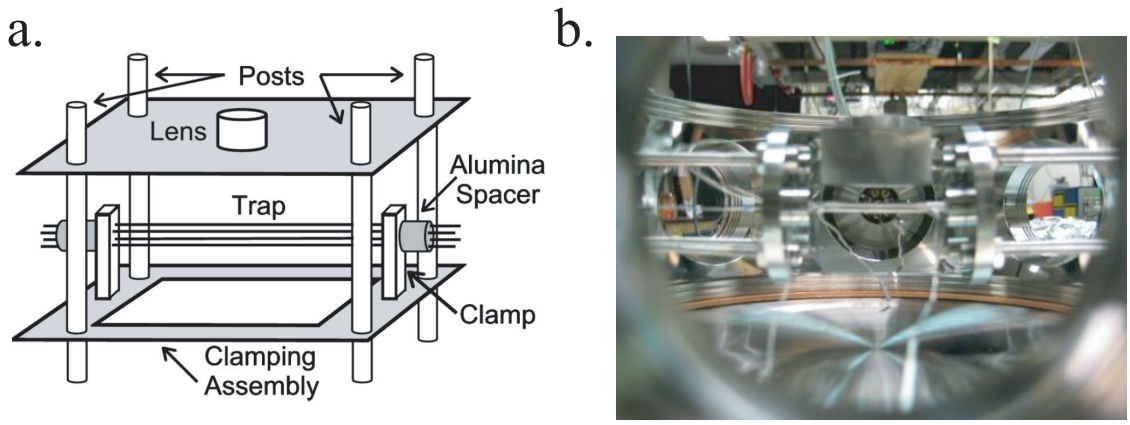

Figure 11: (a) Berkeland trap assembly showing the ion trap mount and lens (image taken directly from Reference [90]). (b) View of the trap in the vacuum chamber with the lens above it.

3.5 Sublimation and Ionization of Calcium

A proper ion candidate must satisfy a number of requirements. First, the ion of interest needs a hydrogenic electronic structure providing a closed cycling transition for laser cooling [4]. Second, a dipole transition that is not too far in the UV (to prevent electrode charging) and an electric quadrupole transition that is not too far in the red is ideal since there are readily available diodes for laser cooling and coatings for these frequency ranges are available on optics. Another requirement is that it is easy to generate an atomic beam; alkaline earth metals have large vapor

pressures at modest temperatures. Heating alkaline earth metals in an oven with a small opening produces an effusive beam of atoms that can be readily manipulated by laser light [4]. Finally, with a mass of 40 amu, calcium can be used for sympathetic cooling of molecular ions of the range $\sim 10 - 160$ amu.

The first step in an ion trap experiment involves loading the ion into the trap, beginning with producing ions from a neutral flux. This is done by sublimating solid calcium metal and directing the neutral flux into the trap. Small chips of calcium are first filed down (to remove an outer-layer of calcium oxide that is always present on solid calcium in ambient conditions) and then quickly placed into stainless steel pouches approximately 10 mm^2 in size. The pouches are then spot-welded shut and a small hole is pierced in one face to allow for the gaseous calcium to later escape (Figure 12). Flaps of stainless steel are added to the outside of the oven along the wire leads to increase the surface area so that the entire apparatus can be resistively heated by running a current through the steel. A current of approximately 2.5 A is generally applied to produce adequate flux.

Having produced a flux of neutral atoms, ions are generated in one of two ways. Electron bombardment requires running a current through a tungsten filament, generating a beam of electrons which then can collide with the neutral calcium to form ions. The main drawback to this technique is that it is not isotope selective (there are six stable isotopes of calcium); it has also been shown that electron and ion bombardment of the electrodes during the loading procedure can cause long-term charging, causing stray electric fields that contribute to excess micromotion and high heating rates [103]. Although initial trapping in the Urabe trap was done using electron bombardment, and all chambers do contain a tungsten filament e-gun, currently all experiments employ a two-step photoionization scheme for calcium ion production.

An advantage of photoionization is that the 423 nm line may be used to confirm the presence of neutral calcium in the trapping region (Figure 13). This is accomplished

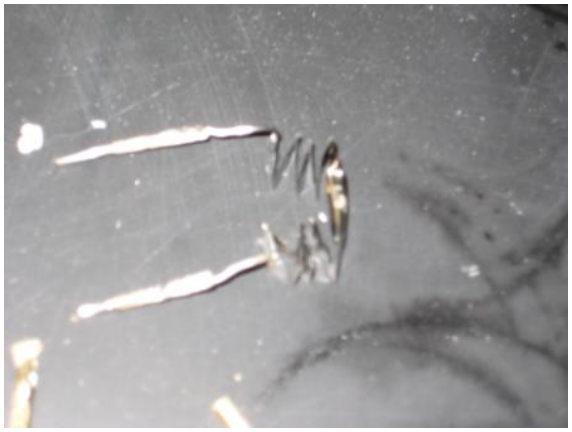

Figure 12: Calcium "burrito-style" oven used in the experiments presented in this thesis.

using a cavity-enhanced ECDL frequency-doubled to 423 nm (Toptica). The first step of the two photon process isotopically selects calcium by exciting the $^1S_0 \leftrightarrow ^1P_1$ transition at 423 nm, which is the strongest in relative intensity of the neutral atom. The first ionization energy of calcium is 6.11316 eV (49305.95 cm^{-1}) [104], so a single 423 nm photon is not sufficient to ionize the atom. Instead, a second excitation step requiring light with a wavelength shorter than 390 nm is necessary to connect the $4p^1P_1$ state to the continuum [85]. For this, a free-running 377 nm laser diode (Nichia) is used. To aid in laser alignment, and also in an attempt to improve trap loading rates, the ionization lasers are sent into the chamber both axially and at 45°. It must be mentioned that although trapped ions do not experience Doppler shifts, the neutral flux does, which requires frequency adjustment of the 423 nm laser depending on the propagation direction. A shift on the order of $\sim$ 800 MHz has been observed when comparing axial and 45° due to the angles relative to the neutral calcium flux.

3.6 Energy level scheme of $^{40}Ca^+$

The isotope $^{40}Ca^+$ has a single valence electron and no hyperfine structure. Doppler cooling is done the via the $S_{1/2} \rightarrow P_{1/2}$ transition at 397 nm (Figure 14). A light field resonant to the $P_{1/2} \leftrightarrow D_{3/2}$ transition prevents optical pumping to the metastable

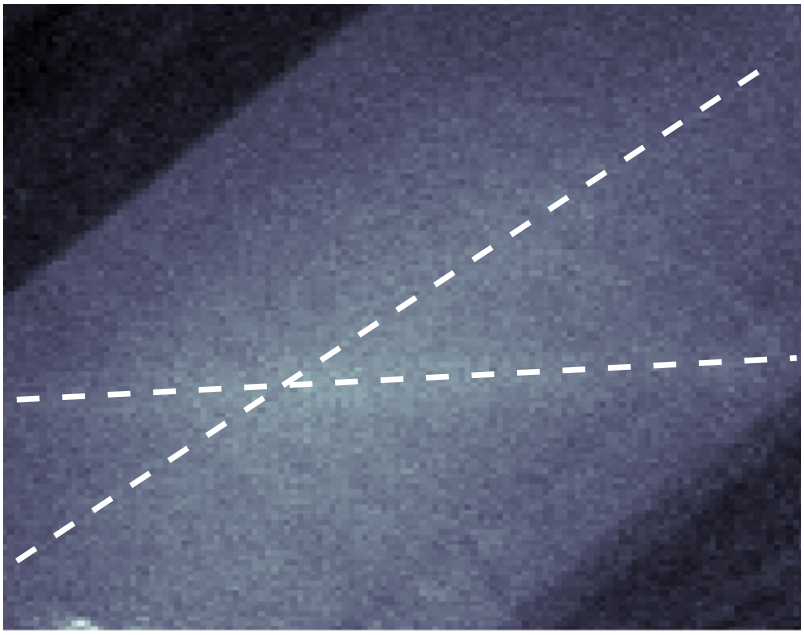

Figure 13: Neutral calcium fluorescence, excited by lasers propagating along the axis of the trap and at 45°. The dark regions in the top left and bottom right corners are trap electrodes. Dashed lines are to guide the eye.

$D_{3/2}$ state [105]. Without the laser at 866 nm, the $D_{3/2}$ state would become populated once every 15.88 cooling cycles (due to the branching ratio between the two transitions) [76]. Coherent population trapping (CPT) is avoided by lifting the degeneracy of the Zeeman sublevels with a magnetic field [85]. CPT occurs when the ion is in a coherent superposition of states (i.e., the detunings of the 397 and 866 nm lasers are equal) so that it becomes effectively transparent to the incident field even in the presence of resonant transitions [102]. This process effectively shuts off Doppler cooling

Efficient Doppler cooling is dependent on detuning, saturation, and polarization of the two cooling lasers. Such cooling is imperative for sideband cooling efforts (Chapter 5). While calcium is a three-level system (so the 866 nm repumper laser must also be optimized for efficient cooling, as shown in Section 5.3), the 397 nm is most imperative (as if a two-level system). Optimal Doppler cooling occurs for a 397 nm detuning of $\Gamma/2$, or 11 MHz red-detuned from resonance. At this detuning

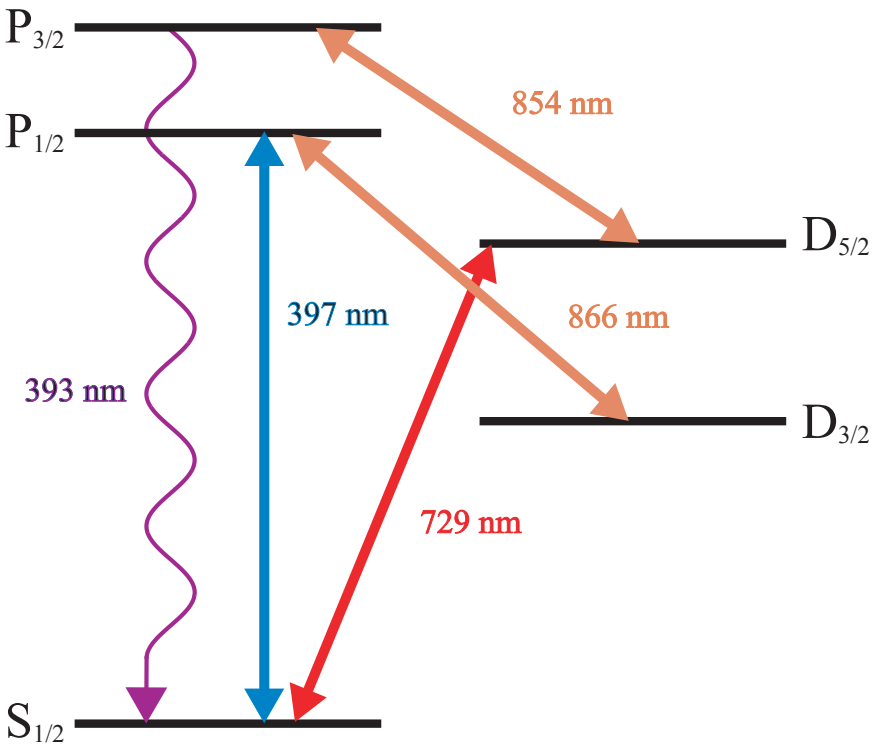

Figure 14: Relevant energy level diagram of Ca^+ with transition wavelengths.

the cooling profile is steepest, resulting in the strongest force profile. If the saturation is increased above 1, power broadening of the transition occurs, leading to decreases in Doppler cooling. This is due to a flattening of the transition lineshape, decreasing the steepness of the peak and also the cooling rate. Too small of saturation values also leads to decreased cooling as not enough scattering occurs. Additionally, excess micromotion can lead to irregular lineshapes due to broadening of the transition. For larger values, the line shape can develop structure that causes the laser to heat, rather than cool the ion, even when red detuned from resonance [89]. Steps to minimize the effects of micromotion are described in Chapter 4. For efficient Doppler cooling it is also important to pay attention to the detuning and saturation parameter used for the 886 nm laser. Over saturating the transition can still lead to Doppler broadening and cause less efficient cooling.

3.7 Trapping Ions

Once the neutral calcium flux has been imaged the Doppler cooling lasers can be coaligned with the ionization lasers to attempt trap loading and laser cooling. It is important to remember that with such varying wavelengths the lasers will not behave the same through a set of lenses, so coalignment should be done before the lenses if possible. In general it is simpler to load a large cloud of ions and then use the fluorescence of the cloud to improve laser alignment until single ions can be loaded. With this in mind, this section will discuss large ion clouds and crystals and then move to smaller numbers of ions, including chains and then single ions.

3.7.1 Ion Clouds and Large Crystals

Ion Coulomb crystals have been studied experimentally in Penning and Paul traps [7]. Large numbers of ions, or ion clouds, can be preferable over few ions so as to obtain a high signal to noise ratio. Other positives include not being concerned with excess micromotion and thus compensation; however, with large crystals you can see Doppler

shifts and proper identification of closely related masses can be more difficult.

For a first attempt at trapping, it is often much simpler to attempt to load a large cloud of ions rather than a single ion. With large, hot clouds of ions, the cooling lasers can be several hundred megahertz red-detuned and still achieve a level of fluorescence that can be detected on a standard camera (Figure 15). Additionally, trapping electrodes can be set to a low voltage without any consideration of minimizing micromotion. Finally, large clouds can be loaded with poor laser alignment and also be imaged with the EMCCD camera even when the focus of the camera is not fully optimized. These are generally the two most difficult components of trapping ions. A camera with too low of resolution also makes initial loading difficult because the cloud may be indistinguishable from background with any focus misalignment. Large clouds of ions are not only used for initial trapping, but can also be useful in spectroscopy experiments [41, 44, 53].

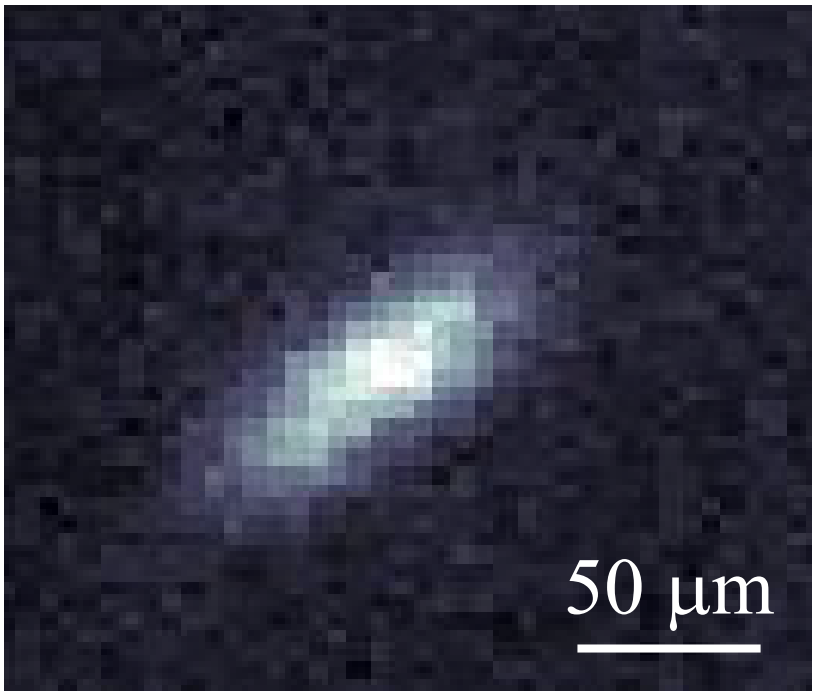

Figure 15: An ion cloud within the Goeders trap. These were the first ions trapped in this trap, July 14, 2010

Ions cooled to sufficiently low temperatures will form spatially ordered states due

to the combination of the trapping potentials and the Coulomb repulsion between ions with the same sign of charge. For normal trapping conditions, crystallization occurs for temperatures below 10 mK [7]. With sufficient laser cooling, so that the Coulomb potential energy between nearest neighbors is much greater than their average kinetic energy, ordered, crystal-like ionic systems of a single sign of charge can be formed [2, 106]. In this novel form of condensed matter, the ions are held together against their mutual Coulomb repulsion by the external fields of the ion trap [107]. Coulomb crystals do not exhibit the same type of long-range order as solid-state crystals, because the trap potential plays a crucial role. As the RF voltage is increased, the volume of the trapping region decreases [6], so often the RF is lowered when first tying to load a cloud. Upon loading, the voltage can be increased to attempt to form a Coulomb crystal.

3.7.2 Single Ions and Ion Chains

At low axial voltages (so that the axial confinement is weak compared to the radial confinement), low numbers of ions will arrange in a chain or string, forming the simplest Coulomb crystal [106]. In this configuration the ions are strongly localized. By increasing the radial voltage, a Coulomb crystal can be forced into this linear arrangement. An image showing the first linear chains trapped in the Urabe and Goeders trap can be seen in Figure 16.

By controlling the RF voltages, the linear chain can be manipulated into several different forms (Figure 17). These images all contain five $^{40}Ca^{+}$; axial voltages were held constant while the RF was slowly increased. Phase transitions of ions between ordered and disordered states have also been studied, especially with regard to classical chaos [5]. A string of trapped ions at zero temperature exhibits a structural phase transition to a zigzag structure, tuned by reducing the transverse trap potential or the interparticle distance [106].

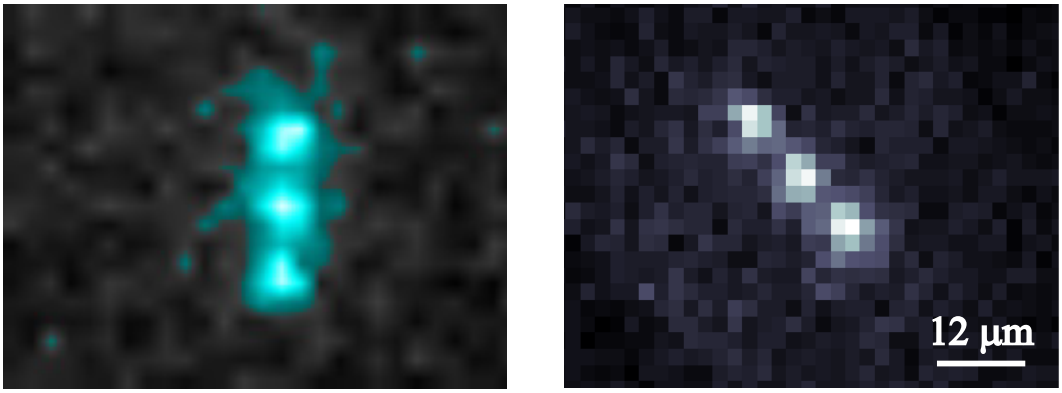

Figure 16: False color image of the first ions trapped in the Urabe trap (September 24, 2007) and the Goeders trap (July 14, 2010)

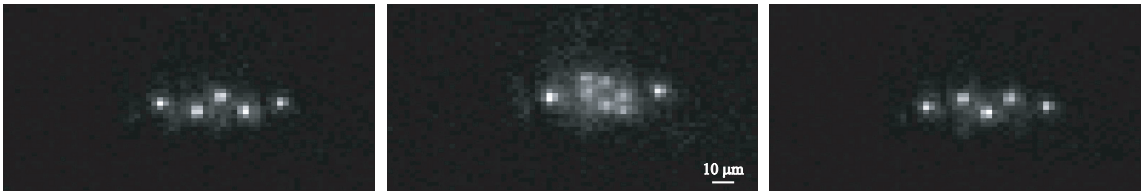

Figure 17: Interesting dynamics with ions in a stray field. As the RF voltage is changed the ions can be pushed into different arrangements.

Once an ion chain is loaded, smaller and smaller numbers of trapped ions can be produced by optimizing laser alignment, compensation voltages, and neutral flux. For high resolution spectroscopy, the idealized experimental condition is that there is only one single ion, so that it experiences no interference from other sample ions; further, it is at rest, so that there are no first- or second-order Doppler shifts. Such an ideal system is nearly realized by confining a single atomic ion in a trap and subjecting it to laser cooling (Figure 18), which leads to an ion temperature on the order of 1 mK [2]. In 1978, Dehmelt was able to demonstrate the first isolation and uniform confinement of an individual atomic ion in a small Paul trap [108]. Space charges due to the simultaneous presence of multiple ions, is a limiting factor, and hence low density or single particle experiments are preferred

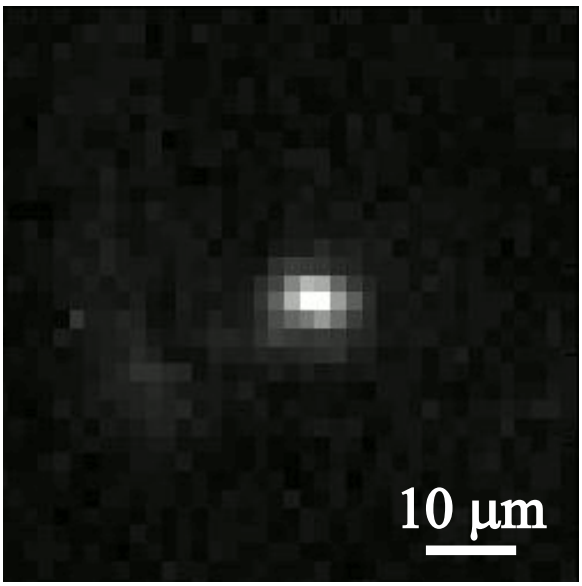

Figure 18: A single $^{40}Ca^{+}$ ion.

3.8 Micromotion

Micromotion refers to rapid ion motion at Ω_{RF} due to the oscillating RF fields. Excess micromotion can occur due to electric fields that force the ion away from the RF minimum of the ion trap, phase shifted RF pick-up on DC electrodes, or phase shifts between the RF electrodes causing RF fields even at the pseudopotential minimum [89]. In an ideal Paul trap, the ion is confined to a position at which the electric field caused by the oscillating drive voltage on the RF electrodes is zero [5]. Micromotion along the trap axis should not occur in a perfectly linear Paul trap, but imperfections in the ion-trap geometry can lead to axial micromotion.

Phase shifts in the RF fields can be caused by asymmetries in the electrical impedances of the electrodes (i.e., if the leads to the trap electrodes have different inductances due to different lengths or geometrical arrangements). Often the RF leads are made as short as possible so as to minimize inductance and to avoid additional electrical noise pick-up. Effusive ovens and electron-emitting filaments can cause contact potentials of a fraction of a volt, or cause trap electrodes to become unevenly charged when this coating or other dielectric or oxide layers are charged by

the emitted electrons [89]. Additionally, patch effects due to different crystal planes at the surface of the electrodes can produce surface potential variations of roughly 100 mV. These are all common methods of stray field production within the vacuum chamber.

Regardless of the cause, micromotion leads to broadening of the electronic transitions of the ion, a higher temperature limit for Doppler cooling, and can cause effective temperatures orders of magnitude greater than the temperature associated with the secular motion at the Doppler-cooling limit [89, 103]. The first-order Doppler shift due to excess micromotion can significantly alter the excitation spectrum of an atomic transition. The spectrum can even change so that a laser heats the ions at frequencies where laser cooling is normally expected [70, 109]. Other adverse effects include alterations of atomic transition line shapes, significant second-order Doppler shifts in high-accuracy studies, and limited confinement time in the absence of cooling. The AC electric field that drives the micromotion may also induce significant Stark shifts in atomic transitions [89] or cause a change in the effectiveness of laser cooling [70].

For spectroscopic experiments, the presence of micromotion makes the experiment inherently flawed. Much work has been done to eliminate this excess motion. Unlike secular motion, excess micromotion cannot be significantly reduced by cooling methods because it is driven. Instead, compensating the ion trap consists of positioning the ion on the RF node by carefully adjusting the DC potential to minimize the micromotion. Under favorable circumstances, the second-order Doppler and AC Stark shifts from excess micromotion can be made to cancel [89]. Chapter 4 discusses methods of detecting micromotion and the presence of stray fields as well as different techniques to compensate ion traps.

CHAPTER IV

COMPENSATION OF ION TRAPS

Excess micromotion refers to rapid ion motion driven at the trap frequency (Ω_{RF}). In a perfect linear Paul trap, excess micromotion along the trap axis does not occur. In practice, it is caused by electric fields that force the ion away from the RF minimum of the ion trap (whether from external factors or imperfections in the ion-trap geometry). In addition, phase shifts between trap electrodes can cause the RF fields to be nonzero at the pseudopotential minimum [110]. Micromotion of ions in Paul traps has several adverse effects, including the alteration of atomic transition line shapes and significant second-order Doppler shifts in high-accuracy studies. The AC electric field that causes the micromotion may also induce significant Stark shifts to atomic transitions [89]. With the appropriate application of auxiliary potentials these undesirable static stray electric fields can be negated, at which point the micromotion is minimized and the trap is considered compensated [103].

Different techniques can be used to detect excess micromotion caused by a uniform static field or phase difference between the trap electrode potentials. The photon correlation method relies on correlating ion fluorescence to the phase of the RF field [89]. Monitoring ion position while changing the strength of the pseudopotential well is often useful in tandem with photon correlation. Resolved sidebands can be used to compare the RF (or micromotion) sidebands of a narrow atomic transition with the carrier transition to estimate the micromotion modulation [89]. Additionally, the characteristic shift of the secular frequency of different massed ions can be monitored by looking at the position of resolved sidebands on a narrow transition [95]. Within

the presence of a stray field, these shifts are altered from their normal position. Finally, by applying an offset RF "tickle" voltage to the drive frequency it is possible to excite micromotion at the secular frequency and monitor dips in ion fluorescence. Generally the axial (**z**) micromotion is compensated before moving to the radial (**x**,**y**). Often, iterations are required since compensating voltages in one dimension often will decompensate one of the other directions. For instance, compensating one dimension (i.e., **x**) may lead to the other dimension (**y**) becoming uncompensated, as the position of the ion has been moved.

4.1 Photon Correlation

In our experimental setup, the photon correlation method is a coarse technique often used for baseline compensation of excess micromotion. However, it is only useful for the axes in plane with ion fluorescence. Due to the overall simplicity, the RF-photon correlation method is often cited as the prime means of eliminating excess micromotion in the literature [83]. In practice, once an ion is trapped, the fluorescence is collected and sent to the CCD and PMT. The PMT collection software is synced to the RF source, allowing for correlation between the ion fluorescence and the RF drive.

In this technique, the correlations of photon arrival times at the PMT with the phase of the driving RF field are minimized. The correlations are caused by the Doppler effect; micromotion modulates the scattering rate of the cooling transition by changing the velocity of the ion. If the cooling laser is red-detuned, the absorption probability is maximized when the ion is moving towards the laser and minimized when the ion is moving away from the laser (each occurring once per cycle) [76]. For excessive micromotion, the detuning (and saturation) of the cooling laser must be monitored because the ion can experience heating for laser detunings that are red-detuned from resonance. As the micromotion is decreased (and thus the velocity of

the ion), the laser should be brought nearer to resonance.

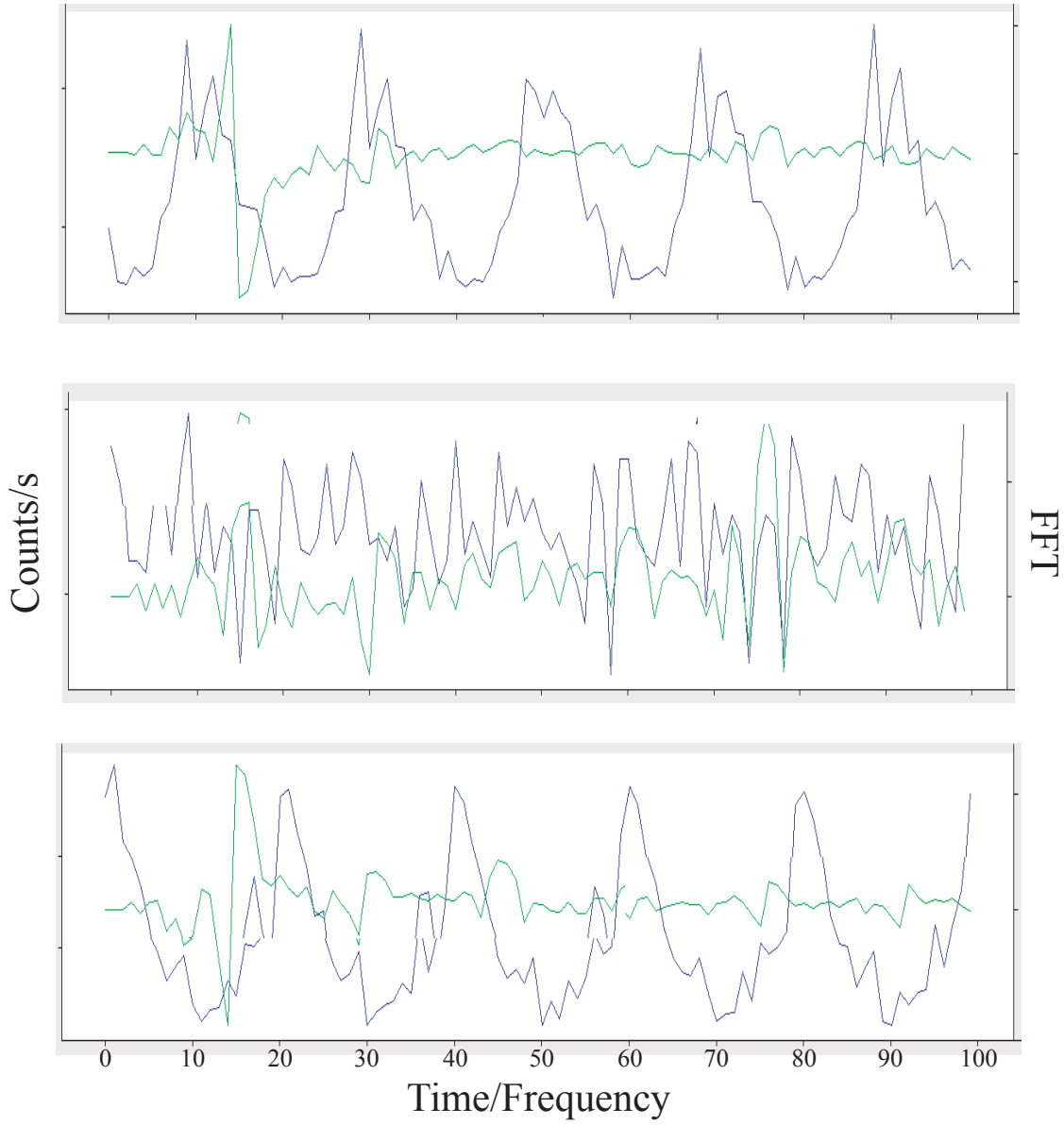

Figure 19: Time lapse of the counts/s (blue) and a Fast Fourier Transform showing the phase (green) synced to the RF drive frequency. As the ion is moved via the compensation voltages the phase between the RF and fluorescence is monitored looking for a "phase-flip." This is most discernable in the FFT which has a noticible change in phase.

The excitation spectrum acts as a transfer function for the translation of the velocity modulation into the corresponding variations of fluorescence intensity [70]. For a small velocity modulation amplitude the response in the fluorescence intensity is harmonic. Asymmetries in the trap field cause the signals from the individual ions to have different amplitudes. The combined signal is then asymmetric. By applying suitable compensating voltages, this asymmetry can be equalized.

4.2 Time Averaged Ion Positions

An alternative method for micromotion compensation involves monitoring the time-averaged position of the ion as the pseudopotential is modulated. An ion in an uncompensated trap will move (for the case of micromotion along the **x** dimension and with the current camera setup this motion is either "up" or "down" on the camera screen) as the voltage is lowered. By monitoring this motion it is possible to change the voltages applied to the compensating electrodes until no further motion is detected. Using the camera to view the ion as it is translated allows the ion position (within the plane of observation) to be determined to the resolution limit of the optics [103]. Ion motion can also be detected in any direction by monitoring the distance that a focused laser beam must be translated to maintain the maximum photon scattering rate from the ions. This is not seen as often in experiments utilizing planar trap geometries due to the higher trap frequencies causing ion motion to be negligible on the scale of the laser focus.

In practice, this method is an excellent complement to the photon correlation scheme. By first obtaining a local minimization point for a particular axis, it is possible to then look for micromotion by monitoring the position of the ion while changing the magnitude of the pseudopotential. This is accomplished by changing the frequency of the RF drive (Ω_{RF}), which necessarily lowers the voltage being applied (since the applied frequency is no longer on resonance with the helical resonator the

Table 3: Example of a compensation table for a single $^{40}Ca^{+}$ ion with endcap values of 59 V and 124 V (secular frequency along **z** of 0.73 MHz). The DC electrodes used for compensation are the top compensation rod (CTop) and the middle bottom electrode (MBot)

Volts on (CTop)	Volts on (MBot)	Direction of Ion Motion
105	0.5	up
95	0.45	up
50	0.239	up
150	0.78	down
125	0.59	slight down
115	0.6	small down
110	0.51	hint up
112	0.55	hint down
111	1.54	no movement

amplification is lowered). Generally, the voltage applied to the compensation rod is varied with large jumps in voltage ($\sim 50 - 100$ V) until the ion motion flips (i.e., instead of going down it now moves up on the EMCCD image). At each step the Mid Bottom electrode is corrected to give a compensated signal for the photon correlation scheme (Table 3).

The main disadvantage to this technique is that it is not sensitive to excess micromotion caused by a phase shift between the potentials applied to the trap electrodes [89]. If there is no static DC field but the phase is nonzero, the average ion position will not change as the pseudopotential amplitude is varied. Techniques that sense the magnitude of the first-order Doppler shift caused by the excess micromotion will eliminate this problem.

4.3 Observation of Stray Fields via Resolved Sidebands

It is also possible to measure the amplitude of micromotion by observing motional sideband strength in all three directions and comparing the ratio of the sideband and carrier Rabi rates. Micromotion due to stray electric fields is compensated by

applying voltages to two compensation electrodes. The correct compensation voltages are found by minimizing the Rabi frequency of the first micromotional sideband of the quadrupole transition for two different laser beam directions [85]. It is also possible to use resolved sidebands for detection of micromotion via the 397 nm transition if the saturation is much lesss than 1 and $\Omega_{RF} > \Gamma$ (i.e., $\Omega_{RF} > 22$ MHz); however, for the secular and drive frequencies used in these experiments, the sidebands are not resolved on the 397 nm line.

In Chapter 6, a novel mass identification scheme will be presented to identify nonfluorescing atomic and molecular ions. For the harmonic potential of an ion trap it has been shown that for two equally charged ions close to their equilibrium positions, the two eigenfrequencies for their motion along the axis of alignment can be related to the secular frequency along **z** of a single ion . Unfortunately, if several ions are stored in the same trap, excess micromotion can also increase the magnitude of the secular motion [70, 109, 111]. The micromotion and secular motion of a single ion in a Paul trap are highly decoupled, so excess micromotion will typically not increase the secular motion. However, if two or more ions are in the trap, the energy of the excess micromotion of any ion can be parametrically coupled into the energy of the secular motion of the other ions (i.e., micromotion interruption). Since the micromotion is driven by the AC field, this heating is continuous and can limit the lowest temperature attainable by cooling methods. In the absence of cooling mechanisms, the ions can gain enough energy to leave the trap. Because of the Coulomb interactions between the ions, the displacements of different ions will be coupled together [14].

For the case of two species of ions, the standard eigenfunction for normal modes breaks down in the presence of a static, stray electric field as seen in Figure 20. With a stray field, ions are displaced from the trap center, which strongly affects the motional frequencies by coupling the axial and radial modes [112]. Since the radial potential is a pseduopotential, this displacement increases with ion mass. This results in heavier

ions being more strongly affected by the static stray field, mixing the axial and radial modes and shifting the normal mode frequencies.

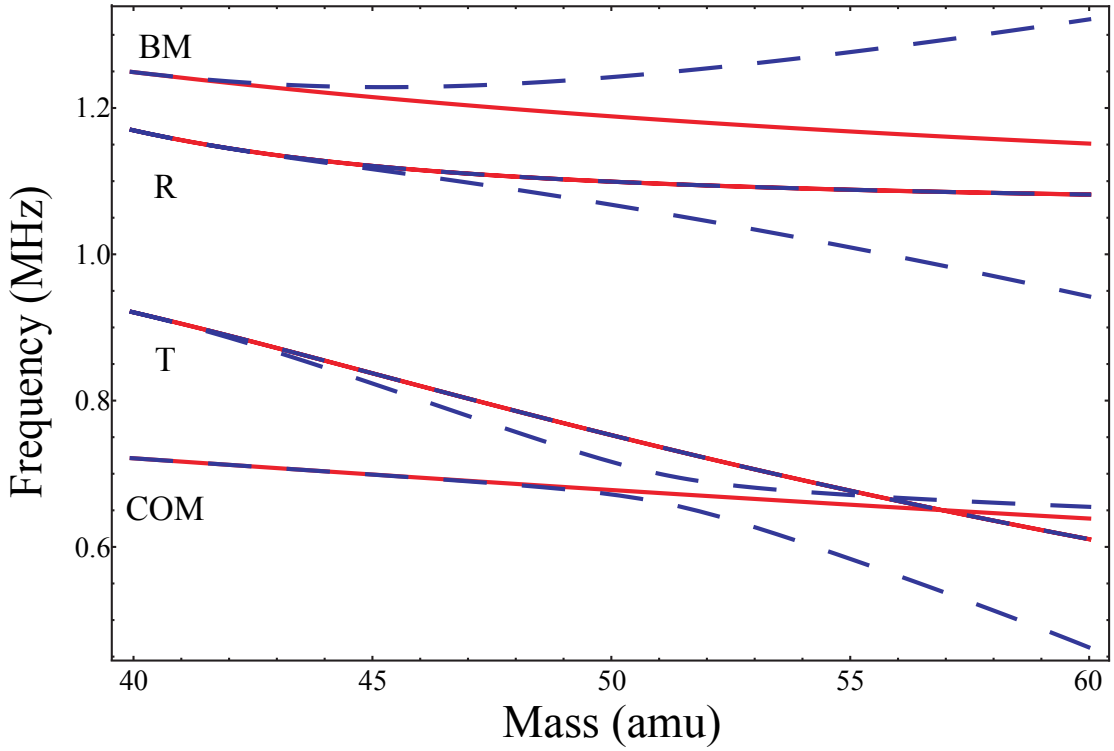

Figure 20: Mixing of normal modes in the presence of a 100 V/m stray field along **x**. Red lines represent the expected normal modes without a stray field. Blue dashed lines represent the normal modes in the presence of a stray field. Labels correspond to the center-of-mass (COM) and breathing (BM) modes along **z** in addition to the radial center-of-mass mode (R) and radial breathing (or tilt, T) mode.

4.4 RF Tickle

Conventional methods to sense and compensate stray electric fields quantify Doppler shifts in ion fluorescence induced by micromotion [103]. A different approach makes use of the fact that when an ion is displaced from the RF node, any bias voltage applied on the RF electrode creates an electric field at the ion position. If this voltage

contains a frequency component that is in resonance with one of the ion's secular frequencies, the ion will be excited in the direction of that secular mode (provided that the driving field from the RF electrodes has some projection onto the mode). The method requires that the mode have an overlap with both the laser direction and the RF excitation direction. Experimentally, it is found that large oscillation amplitudes of the secular motion can be detected as changes in ion fluorescence if the mode has a component along **k**. Minimizing micromotion is achieved by shifting the ion position via DC potentials until the ion is in the RF minimum and cannot be excited by driving the RF electrode at any of the secular frequencies [103].

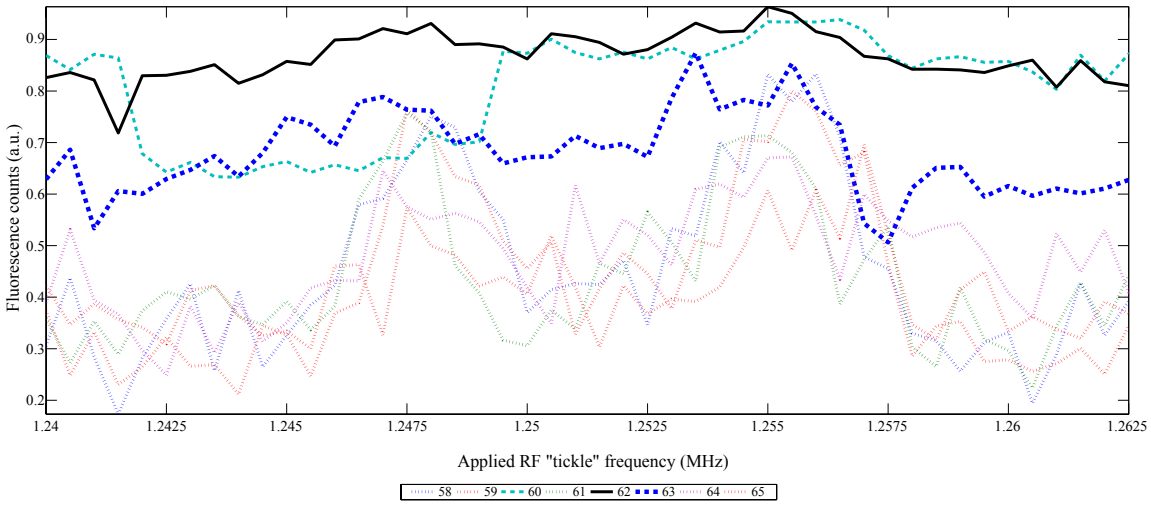

Figure 21: Plots of fluorescence dips with RF tickle. Voltages listed are those applied to the CTop compensation rod. At each CTop voltage the voltage applied to the Mid Bottom compensation electrode is updated to give a compensated value using the photon correlation method. For uncompensated values, characteristic bumps and dips can be seen in the ion fluorescence. The trap is compensated for CTop = 62 V, where the fluorescence stays constant across the applied tickle frequencies. The two voltages on either side of the compensated value also show reduced changes in fluorescence intensity. Electrode labels defined in Figure 9 in Section 3.1.3

Instead of exciting at the secular frequency ω_i directly (as in the case of the mass measurement seen in Chapter 6), excitation is applied at a frequency $\Omega_{RF} + \omega_i$. To achieve this, the excitation signal from a function generator is mixed with the trap

drive Ω_{RF} before amplification with a helical resonator, and scanned about $\Omega_{RF} + \omega_i$ [103]. When the frequency of the excitation becomes resonant with one of the secular frequencies the ion motion is driven, resulting in a decrease in ion fluorescence (Figure 21). For this method, one selects the frequency of the Doppler cooling laser to be close to the 397 nm transition, thus maximizing sensitivity of the ion fluorescence to the ion kinetic energy (at the expense of Doppler cooling). Between successive scans, the voltages of the DC electrodes are adjusted such that the static electric field minimum moves predominantly in the direction of the secular mode being excited. The compensated position is reached when resonance of the excitation does not result in a decrease in fluorescence [103].

CHAPTER V

GROUND STATE COOLING OF CALCIUM

Prior to 1989, all laser cooling experiments were done with the oscillation frequency of the particle in the weak binding limit. When an ion bound in the resolved sideband regime is cooled it can be made to occupy the ground state of its confining potential most of the time [64]. In 1989, laser cooling of a single trapped ion to the motional ground state was demonstrated with ground state cooling of an ion string [84].

For a confined particle, the periodic motion in a trap leads to sidebands in the absorption spectrum at the trap frequency. Sideband cooling results from optical pumping to states with a lower vibrational energy. This requires the vibrational states to be separated by more than a linewidth of the cooling transition, such that the motional sidebands can be spectrally resolved (strong confinement). Widths of dipole-forbidden transitions are usually small enough to meet this requirement [75]. Hence, absorption on a lower sideband is dominantly followed by emission on the carrier frequency; i.e., the atom's transition frequency and therefore an energy transfer is achieved resulting in very efficient cooling (sideband cooling). The ion may be brought to a "state of complete rest in free space" by sideband cooling. As a consequence, all Doppler shifts vanish [108].

Sideband cooling is the process of driving the resolved sidebands of a transition (i.e., the $S_{1/2} \rightarrow D_{5/2}$ quadrupole transition in calcium [113]) to bring the ion to its motional ground state. The narrow cooling laser is detuned to the lower motional sideband so that the ion absorbs photons of energy $\hbar(\omega - \omega_{sec})$ and reemits photons of energy $\hbar\omega$. Hence, on average, each scattered photon reduces the atom's vibrational energy by $\hbar\omega_{sec}$ and the atom's vibrational quantum number, n, by 1. In this way,

it is possible to reduce the mean quantum number, $\bar{n}$, to much less than 1 [5]. Once the motional ground state has been reached, all Doppler shifts vanish [108], which is invaluable for molecular spectroscopy. Reaching the ground state with a molecular ion will require sympathetic sideband cooling via the atomic ion [114]. This will make ultracold ion chemistry possible, where novel quantum effects are expected at temperatures in the microkelvin range [115]. This chapter covers sideband cooling of a single $^{40}Ca^{+}$ ion in the Goeders trap, with preliminary results towards sympathetic sideband cooling of a second ion ($^{44}Ca^{+}$). Only the axial mode is cooled as the 729 nm laser propagated axially in these experiments. Cooling of the radial mode would require the laser to have some component of its k-vector along each radial secular axis.

5.1 State Preparation

A 729 nm laser interacting with an ion in the presence of a non-negligible magnetic field will populate the ten Zeeman sublevels (as seen in Figure 22 and Section 2.5). Quadrupole transitions couple only specific states, depending on the magnetic field direction, laser $\mathbf{k}$ vector, and laser polarization $\hat{e}$. For the 854 nm dipole repumper, selection rules allow $\Delta m_j = \pm 1, 0$. In the current experimental setup, the k-vector of the 729 nm laser is always perpendicular to the direction of the magnetic field. Due to selection rules, this eliminates the $\Delta \mathrm{m}_j = 0$ levels from the spectrum.

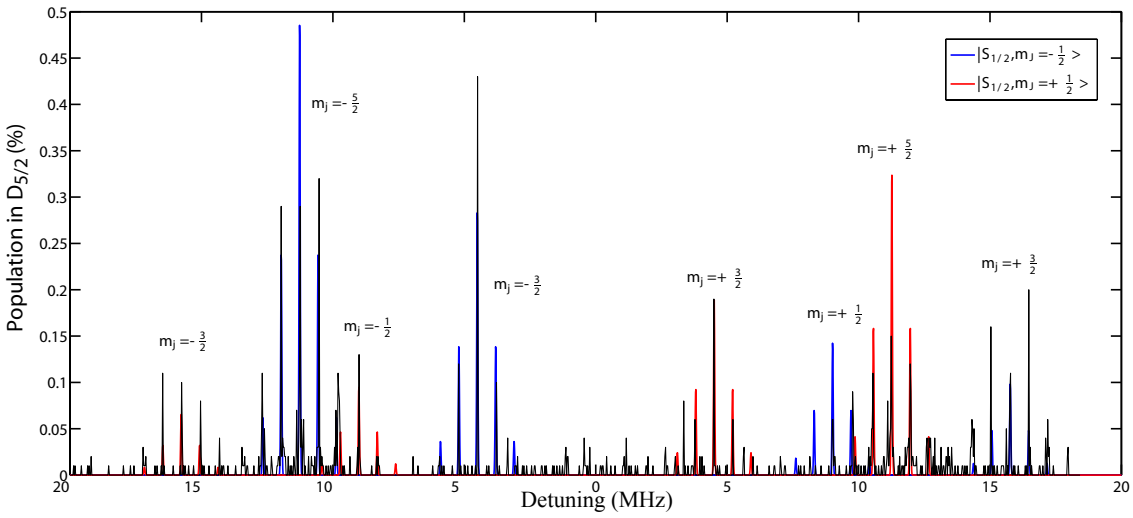

Figure 22: Frequency scan of the 729 nm transition of a single Doppler laser cooled $^{40}Ca^{+}$ ion versus population in the $D_{5/2}$ state. The legend is of the $S_{1/2}(m_j = \pm 1/2)$ states with the individual sets of peaks representing the $D_{5/2}(m_j)$ states. The $\Delta m_j = 0$ transitions are not populated in the current experimental setup.

By controlling the polarization of the 729 it is possible to control the populations in the $\Delta m_j = \pm 1$ and $\Delta m_j = \pm 2$ transitions, as seen in Figure 23. The mass spectrometry and compensation experiments discussed within this thesis did not require substantial state preparation of the Zeeman sublevels; additional transitions being populated was not important, as no additional cooling was being applied nor was peak height relevant above a threshold such that detection was easily obtained. For sideband cooling it is necessary to start in a pure state, so polarization is used as a tool to eliminate population in unwanted transitions.

For sideband cooling a closed system is necessary, so that the electron will necessarily decay to the initial state after cycling, enabling pumping. The polarization of the 729 can be controlled so that the selection rule for the electric-quadrupole-allowed transitions to the various Zeeman states is $\Delta m_j = \pm 2$. The $\Delta m_j = 2$ transitions are chosen so that the $S_{1/2}(m_j = -1/2) \leftrightarrow D_{5/2}(m_j = -5/2)$ transition can be used for sideband cooling, though the symmetric transition will also work. This system is (nearly)

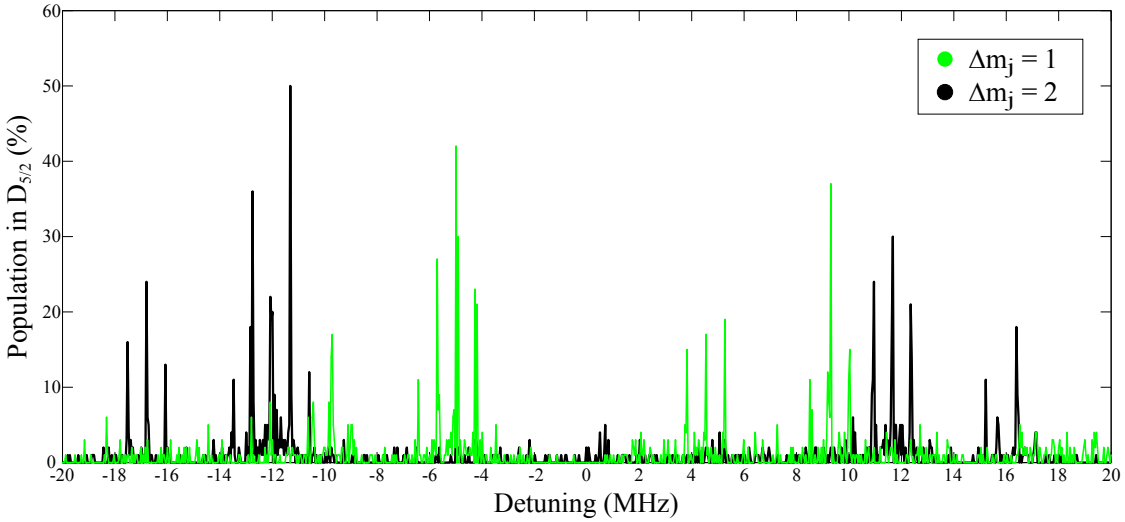

Figure 23: By using a half waveplate between the fiber coupler and the ion it is possible to control the polarization of the 729 nm light and select which transitions are populated. When $\mathbf{k} \perp \mathbf{e} \perp \mathbf{B}$, only $\Delta m_j = \pm 2$ transitions are populated. By rotating the polarization 90°, only $\Delta m_j = \pm 1$ is populated. Between these two extremes will be a mixture of $\Delta m_j = \pm 1$ and $\Delta m_j = \pm 2$ (Figure 22).

closed because the $D_{5/2}(m_j = -5/2)$ state will necessarily return to $S_{1/2}(m_j = -1/2)$ after pumping to $P_{3/2}$ via the 854 dipole transition ($\Delta m_j = \pm 1, 0$) then decaying to the $S_{1/2}$ state again via a dipole interaction. The system is almost closed since the $P_{3/2}(m_j = -3/2)$ state can fall to $D_{5/2}(m_j = -1/2, -3/2$ or $-5/2)$ states (see Figure 30 in Section 5.4).

After the proper geometric concerns are taken into account, only four Zeeman sublevels are populated. Before beginning sideband cooling experiments, it is necessary to initialize the ion in a well defined electronic state, which is chosen to be the $S_{1/2}(m_j = -1/2)$ ground state. This requires an additional state preparation step. One method involves optical pumping with σ^- polarized 397 nm light along the quantization axis [76]. Unfortunately, this method of optical pumping leads to restrictions related to the freedom of choosing the orientation for the quantization axis, and can be cumbersome to realign the σ beam path each time the angle of the magnetic field is changed [116]. Rather, a slower (in terms of pulse timings to reach

the initialized state) but simpler process is available using the 729 to optically pump out of the $S_{1/2}(m_j = +1/2)$ state.

This state preparation technique, termed "spin polarization," pumps the ion out of the $S_{1/2}(m_j = +1/2)$ state during initialization through use of the $S_{1/2}(m_j = 1/2) \leftrightarrow D_{5/2}(m_j = -3/2)$ transition [117]. Because the transitions starting from $m_j = +1/2$ and $m_j = -1/2$ have different Zeeman shifts they are resolved (a magnetic field lifts the degeneracy), the population in the $m_j = +1/2$ state can be selectively pumped to the $D_{5/2}$ state, and subsequently returned to the $S_{1/2}$ state via the $P_{3/2}$. The decay from the $P_{3/2}$ state is not selective, and returns the electron to either of the $S_{1/2}$ states, with the exact ratio dependent on the polarization of the 854 nm laser. After a number of cycles the entire population can be pumped to the $S_{1/2}(m_j = -1/2)$ state (Figure 24). Using the Clebsch-Gordon coefficients it can be shown that it only takes 6 cycles to reach $> 99\%$ state initialization, but for most of the experiments presented in this thesis 10 spin polarization loops were utilized.

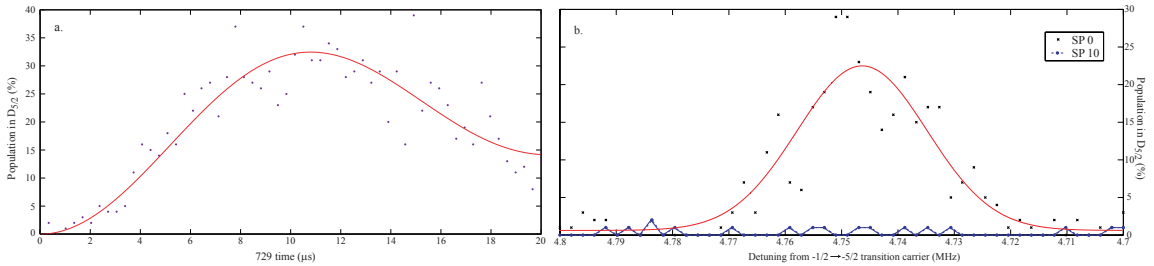

Figure 24: (a) Rabi scan demonstrating how to determine the length of a π pulse for the $S_{1/2}(m_j = 1/2) \leftrightarrow D_{5/2}(m_j = -3/2)$ transition (fit using Eqn. 13 in red). (b) Effects of spin polarization loops on the $S_{1/2}(m_j = 1/2) \leftrightarrow D_{5/2}(m_j = -3/2)$ transition showing the population driven from the $S_{1/2}(m_j = 1/2)$ level (Gaussian fit of the peak in red, blue dashed line is to guide the eye).

Optimization of spin polarization loops is fairly simple. Since each Zeeman sublevel has a different dependence on the magnetic field, changing the strength of the field will shift the separation between adjacent peaks. It is important to guarantee that the sidebands of adjacent peaks do not overlap. Once the location of the

$S_{1/2}(m_j = 1/2) \leftrightarrow D_{5/2}(m_j = -3/2)$ transition is known, it is worth running a Rabi scan on the carrier. This form of scan varies the length of the 729 nm pulse while leaving the detuning constant. By mapping the transition from the ground state to excited state it is possible to get out the relative frequency (Rabi frequency, Ω) of the transition for a given saturation. Spin polarization should be performed with a π-pulse (so named for a pulse that will make a π rotation on the Bloch sphere, but more generally will take the population in one state and necessarily move all of it to the opposite state, i.e., from $S_{1/2}(m_j = 1/2)$ to $D_{5/2}(m_j = -3/2)$). To efficiently pump out the $S_{1/2}(m_j = 1/2)$ state, full power is used. By monitoring the height of the $S_{1/2}(m_j = 1/2) \leftrightarrow D_{5/2}(m_j = -3/2)$ transition with increasing numbers of spin polarization loops, the ideal number of loops can be determined.

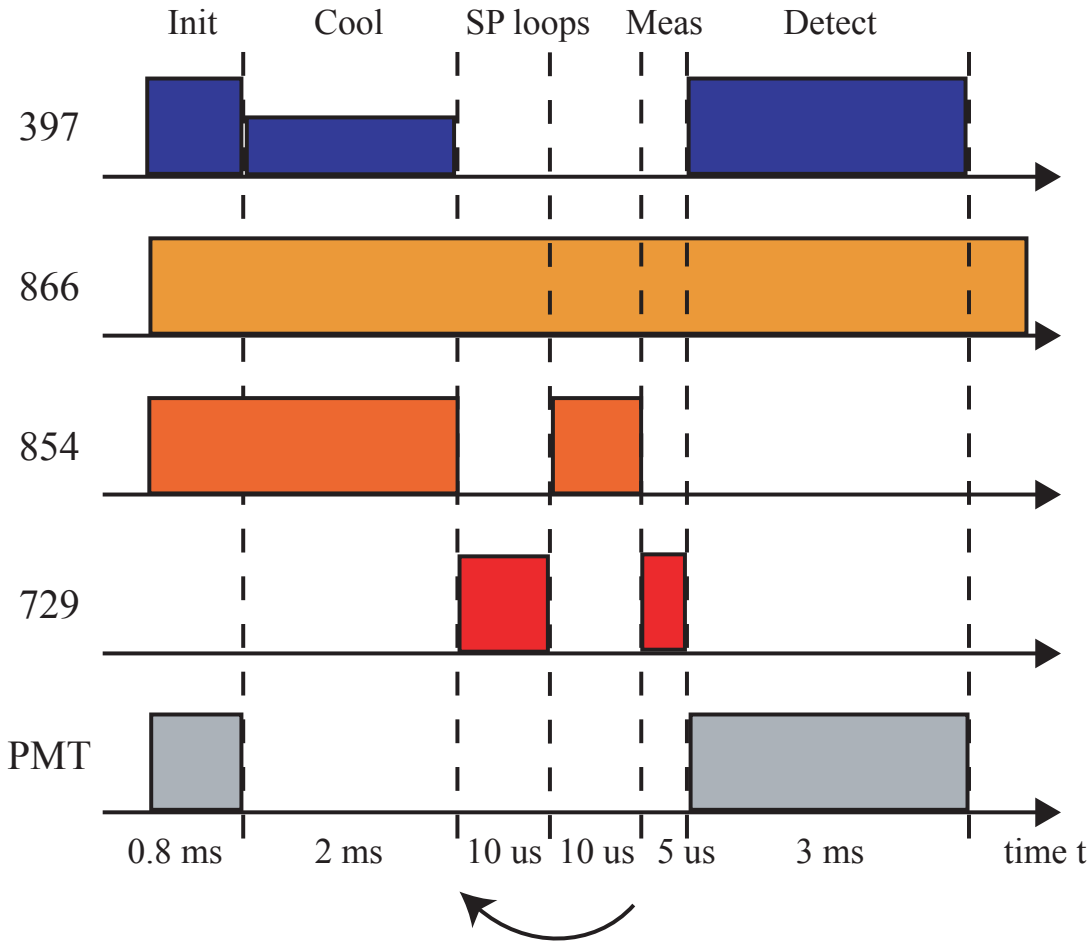

Figure 25: Pulse sequence used for spin polarization. For all steps the 866 nm laser is left on at the ideal saturation and detuning for optimal cooling, discussed in Section 5.3. Detection measurements are made with the 397 nm laser at full or "detection" saturations and detunings (the detuning is chosen to be near resonance and with saturations above the ideal cooling limit). This step is to initialize the electron shelving experiment by confirming the presence of an ion. The Doppler cooling step has the 397 nm laser detuned from resonance and lowered in power to achieve optimal Doppler cooling for a set time. The π-pulse is implemented at high 729 nm laser power on resonance with the carrier of the $S_{1/2}(m_j = 1/2) \leftrightarrow D_{5/2}(m_j = -3/2)$ transition. The 854 nm laser is used to reinitialize the system. After all of the spin polarization loops are complete, a final detection step is implemented to determine percent shelving.

5.2 Coherent Dynamics after Doppler Cooling

After determining the appropriate frequencies of the carrier and sidebands, additional information is obtained by varying the interaction time of the laser with the ion at a fixed frequency. Figure 26 shows the oscillation of the ion's population between the ground and excited states after Doppler cooling and state preparation (i.e., no sideband cooling loops). Rabi experiments done on the carrier transition are useful in optimizing Doppler cooling because initial temperatures can be determined from fits to the data. Generally, motional state occupancy is evaluated by comparing the heights of the first order sidebands while ensuring that the interrogation time, t, is the same for the blue and red sidebands [63, 118]. Unfortunately, for large n, this measurement fails (though the ratio of higher order sidebands can be used). The function used for all Rabi fit calculations, which gives population in the excited state, is:

$$\rho_{DD}(t) = \frac{1}{2}(1 - \frac{1}{\bar{n}+1}\frac{cos(2\Omega_0 t)(1 - xcos(2\Omega_0 t\eta^2)) + xsin(2\Omega_0 t)sin(2\Omega_0 t\eta^2)}{1 + x^2 - 2xcos(2\Omega_0 t\eta^2)}), \quad (13)$$

where x = $\bar{n}/(\bar{n}+1)$, η is the Lamb-Dicke parameter, and Ω_0 is the Carrier Rabi frequency [76]. The Rabi scan shown in Figure 26 has an initial temperature value of $\bar{n} \sim 28$ quanta using the fit from Eq. 13, which is higher than the Doppler limit for the current trap parameters.

The theoretical Doppler limit was discussed in Chapter 2; this value is not always reached in practice. Instead, the number of quanta in a given mode is dependent on the secular frequency by:

$$\bar{n} \approx \frac{\Gamma}{2\omega_{sec}} \quad (14)$$

So for the 397 nm transition ($\Gamma = 22$ MHz) and an axial secular frequency of 0.73 MHz, an initial $\bar{n}$ of 15 is achievable. This demonstrates that for Figure 26 Doppler cooling was not being performed efficiently. With sideband cooling, the more quanta that must be removed from the system, the more pulses are necessary, and therefore more

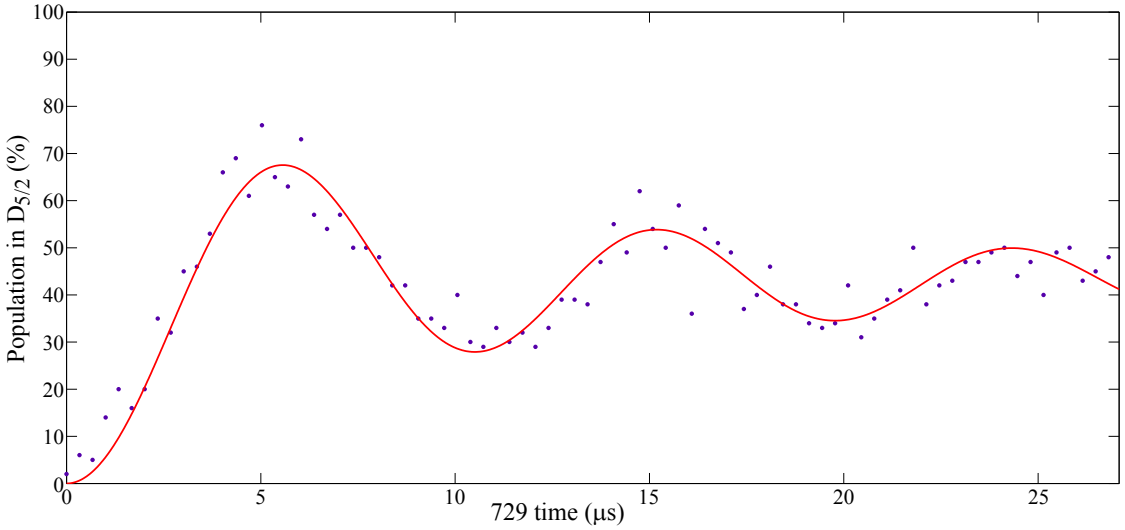

Figure 26: Rabi scan with state preparation after Doppler cooling.

time. The true limit to how cold a system can get is the balance between the heating rate of the ion trap and the cooling rate. If it takes longer to remove a quanta than for the system to regain a quanta through anomalous heating, no more cooling will occur. Therefore, achieving efficient Doppler cooling is one of the most important steps in sideband cooling [119]. Techniques for optimizing Doppler cooling are now presented.

5.3 Optimization of Doppler Cooling

It is important to reduce the vibrational quantum number as low as possible in the Doppler-cooling stage, because the cooling rate for Doppler cooling on the dipole transition is higher than that for sideband cooling on the quadrupole transition. Efficient Doppler cooling is also necessary to deeply confine the ions into the Lamb-Dicke regime. The parameters that can be controlled to optimize Doppler cooling are the intensities and detunings of the 397 and 866 nm cooling beams and the magnitude of the applied magnetic fields [120]. In addition, as discussed previously, excess micromotion cannot be reduced by laser cooling, but rather leads to a decrease in the cooling efficiency, preventing the ion from being cooled to the Doppler limit.

To demonstrate the effects of detuning and saturation on temperature, a number of Rabi experiments were run with different values for the 866 nm (Figure 27) and 397 (Figure 28) lasers. Although $^{40}Ca^{+}$ has a three-level configuration for Doppler-cooling, it can be approximated as a two-level system when the $P_{1/2} \leftrightarrow D_{3/2}$ transition is saturated. Therefore, the final temperature of the ion is mainly determined by the parameters for the 397 nm laser; however, experimental results have demonstrated that the detuning of the 866 nm laser can affect the cooling efficiency as seen in Figure 27. For the 866 nm laser, the most important factor seems to be avoiding coherent population trapping, so detunings near resonance or slightly blue of resonance are preferred, with saturations chosen near 1 so as to not overly broaden the transition.

The optimum value of the 397 nm detuning is known to be $\Gamma/2$, which gives a value of -11 MHz (in absolute units, the AOM value is -5.5 MHz due it being in a double pass configuration). The saturation parameter is chosen by first detuning the laser the appropriate amount while at full power, and then reducing the power until the PMT counts are cut in half [76]. The least efficient cooling is present in the data for -50 MHz 866 detuning. At this detuning, coherent population trapping occurs, shutting off Doppler cooling since few photons are being scattered. Over-driving the 397 and putting it too close to resonance also leads to poor cooling, much more so than being over driven and further red detuned.

The magnetic field can also play a role in Doppler cooling. At low levels, the effect of the ambient magnetic fields (due mostly to the ion pump and partially the the Earth's magnetic field) predominates. In this case, the repumping efficiency of the 866 nm laser, and subsequently the cooling efficiency, is reduced. Large magnetic fields broaden the $S_{1/2} \leftrightarrow P_{1/2}$ transition, and as a result the temperature is raised [120].

A simple way to monitor Doppler cooling efficiency is to vary the different laser

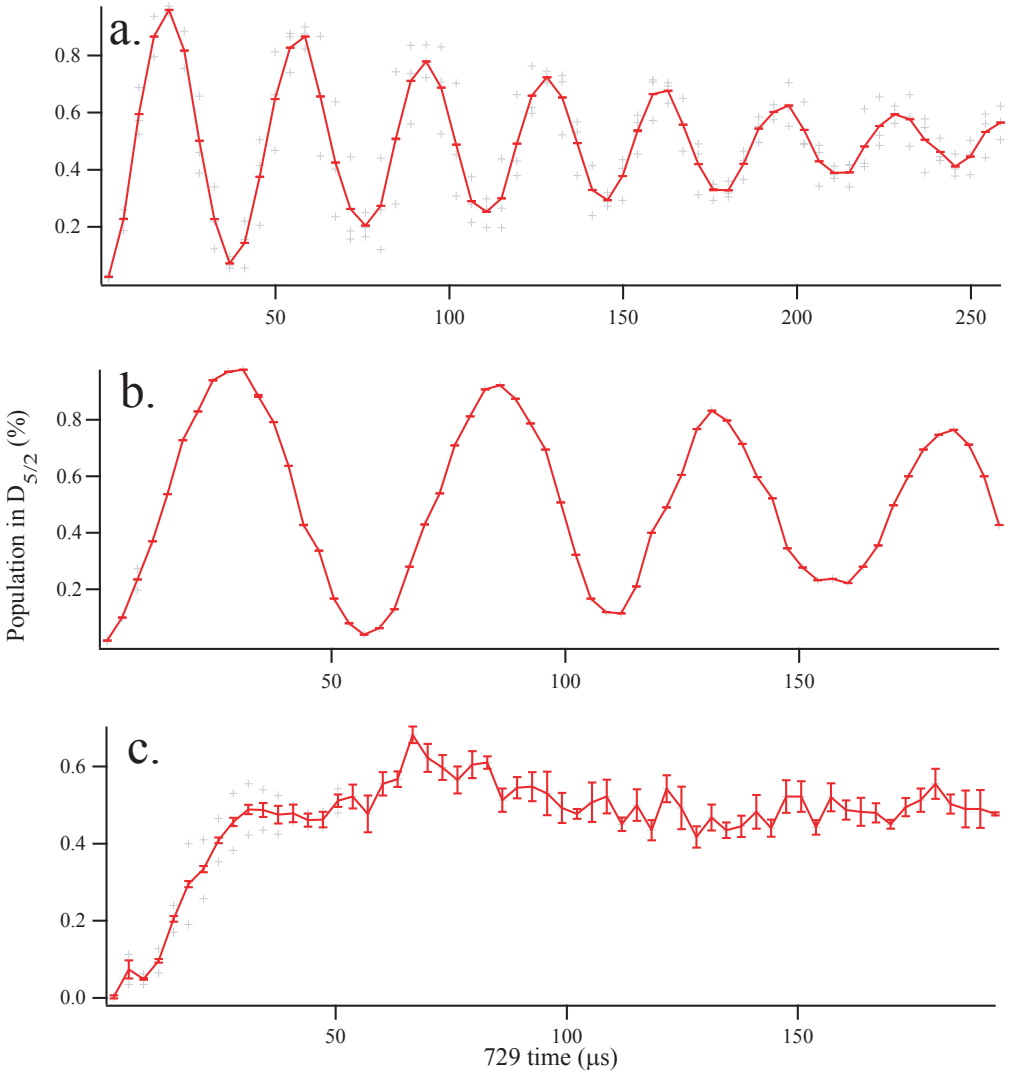

Figure 27: Effect of varying the detuning and saturation of the 866 nm laser on Doppler cooling. (a) Normal trap conditions. (b) Normal 397 saturation and detuning, $\Delta_{866} + 50$ MHz. (c) Normal 397 saturation and detuning, $\Delta_{866} - 50$ MHz. The saturation of the 729 nm laser was purposely attenuated by ~ 50x from max to reduce the Rabi frequency; with full laser power, off-resonant coupling to other states causes increased decoherence. Scans taken by S. Charles Doret at GTRI

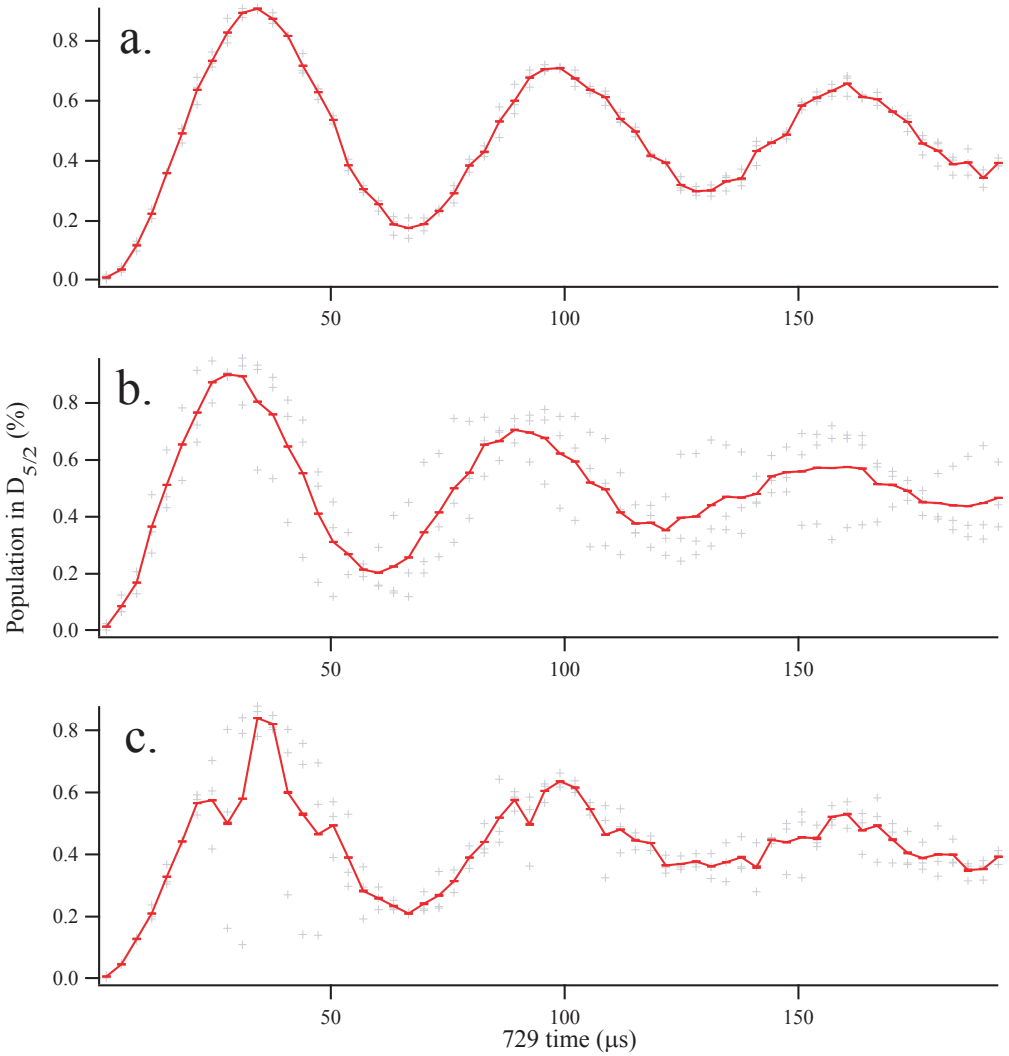

Figure 28: Effect of varying the detuning and saturation of the 397 nm laser on Doppler cooling, visible in the Rabi scans. (a) Normal 866 saturation and detuning, 397 saturation 10× normal values. (b) Normal 866 saturation and detuning, 397 saturation 10× normal values and detuned 10 MHz closer to resonance. (c) Normal 866 saturation and detuning, 397 saturation 10× normal values and detuned an additional 10 MHz away from resonance. Scans taken by S. Charles Doret at GTRI

parameters and observe how the Rabi flops change, mostly seen in the ratio of exponential decay time to π-time (decoherence). Changes to the actual π-time are subtle, though they do occur, while watching for more flops prior to decoherence is more dramatic. Estimates of $\bar{n}$ should be calculated, until the experimental results are close to the expected value ($\bar{n} = 15$). Once the ion is cooled near the Doppler limit, sideband cooling can be attempted.

5.4 Ground State Cooling of a Single Ion

Once it is possible to prepare the initial state of the ion with near-unity precision in the $S_{1/2}(m_j = -1/2)$ state while also cooling to the Doppler limit, sideband cooling is a simple extension. Including the sideband cooling loops makes the pulse sequence more complex, so a diagram is presented in Figure 29. The major change is that after initialization, the 729 nm laser is detuned so it is on resonance with the red sideband and a π-pulse is implemented. Values necessary for the different pulses are extracted from the fit given by Equation 13, including the initial motional occupancy, $\bar{n}$, the π-time of the hottest phonon of the red sideband (which gives the initial π-time to be used), and the final π-time. As the ion gets colder, the necessary Rabi time applied on the carrier decreases while on the sidebands increases. By starting at $2 \times t_\pi$, and doing a linear extrapolation out to the longest π-time, the number of loops can be calculated; currently ~ 40 loops are standard. These parameters can all be optimized to allow for faster cooling.

While the current method of state preparation is sufficient for purely driven transitions, spontaneous emission can cause the series of transitions to no longer be a closed cycle. From the $D_{5/2}(m_j = -5/2)$ state, the 854 nm laser necessarily will populate the $P_{3/2}(m_j = -3/2)$ state (because of selection rules for a dipole transition) which must fall to the initial $S_{1/2}(m_j = -1/2)$ state. However, the $P_{3/2}(m_j = -3/2)$ state can also spontaneous emit back to the $D_{5/2}$ manifold, where the electron can also populate the

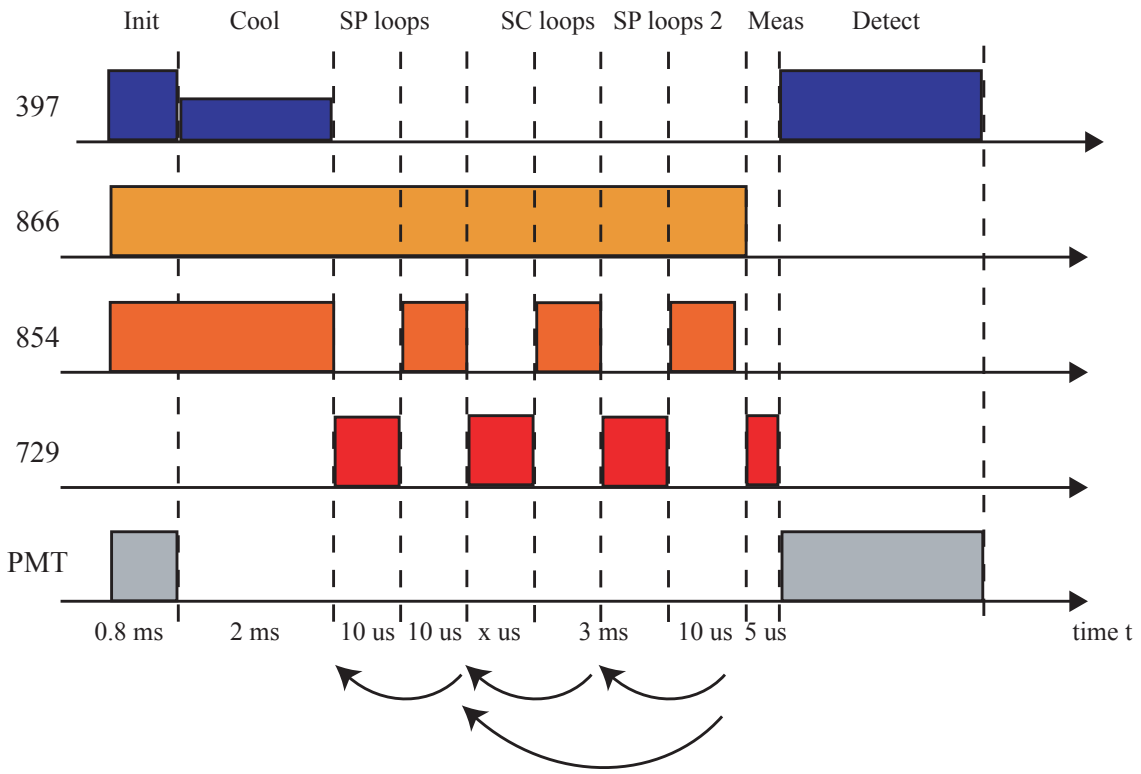

Figure 29: Pulse sequence used for sideband cooling. As with state preparation, for all steps the 866 nm laser is left on at the ideal saturation and detuning for optimal cooling, discussed in Section 5.3, and detection measurements are made with the 397 nm laser at full or "detection" saturations and detunings. After an adequate number of spin polarization loops are applied to initialize the system, the 729 nm laser is put on resonance with the red sideband of interest (generally the first order axial sideband) and a pulse of appropriate length is applied at full laser power so as to cool as quickly as possible. As the system gets colder the length of this pulse is increased as determined by Eqn. 13. Additional spin polarization cycles (labeled SP loops 2) are necessary due to population loss from spontaneous decay of the $P_{3/2}$ level to $D_{5/2}$ as seen in Figure 30. After all loops are complete the 729 nm laser is scanned across the relevant sidebands to determine percent shelving and motional quanta of the system.

$D_{5/2}(m_j = -3/2)$ or $D_{5/2}(m_j = -1/2)$ states. Unfortunately, this allows the 854 nm laser to then drive to additional sublevels of $P_{3/2}$ allowing for the $S_{1/2}(m_j = +1/2)$ state to become repopulated, ending all sideband cooling (Figure 30). This process is dependent both on the branching ratio of the $P_{3/2}$ level as well as the Clebsch-Gordon factors which determine how often each of the $D_{5/2}$ sublevels become populated. On average, the state becomes mixed after $80 - 160$ cycles [76]. This cannot be fixed with polarization of the 854 nm light, but rather additional spin polarization cycles must be placed within the sideband cooling sequence to reinitialize the experiment. Currently extra state preparation is done after every 20 sideband cooling steps.

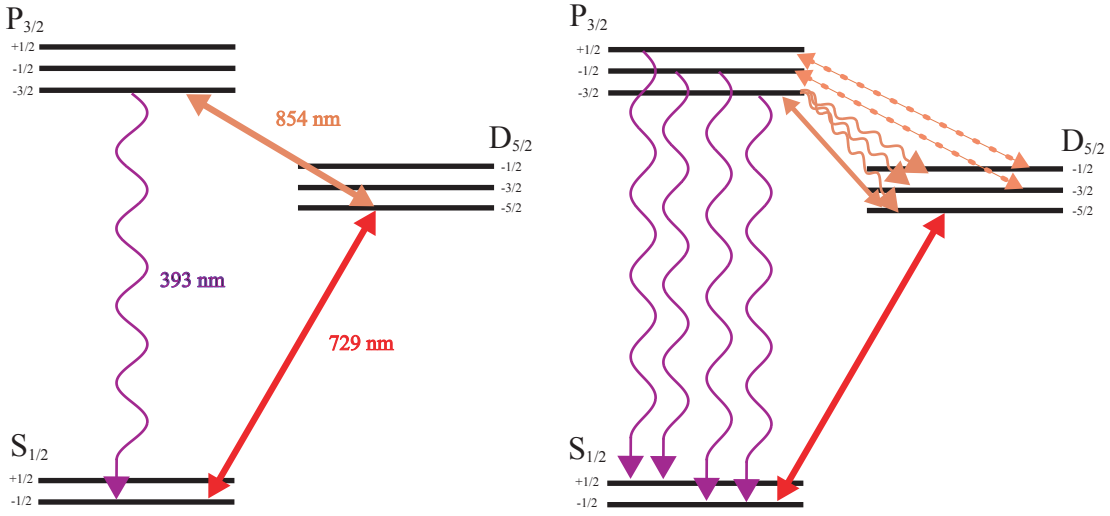

Figure 30: Normal closed cycle for sideband cooling and the decay channels that can eliminate state preparation and open the cooling cycle. Note that not all sublevels are shown in this diagram.

After sufficient sideband cooling (Figure 31), the motional state of the ion can be determined by comparing the ratios of the first order sidebands by the following equations [118]:

$$R = Intensity_{RSB}/Intensity_{BSB} \; ; \; \bar{n} = \frac{R}{1-R}. \tag{15}$$

Thus, if t is the same for the blue and red sidebands (the Rabi frequency is now much slower with the ion cold so the π-time must be adjusted to get large transition

probability) the ratio of red to blue sideband strength gives $\bar{n}$ [63]. Additionally, to avoid AC Stark effects and non-resonant coupling of Zeeman levels, the laser powers are reduced when scanning across the peaks.

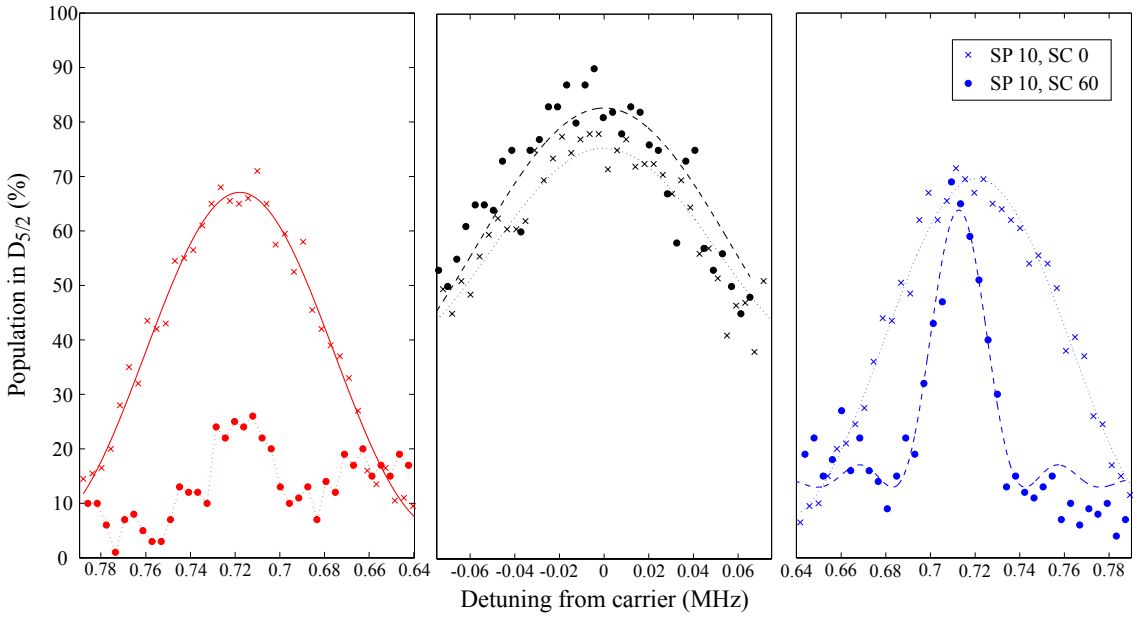

Figure 31: The red and blue sidebands in addition to the carrier transition before (crosses) and after (circles) sideband cooling loops were applied. Notice the carrier and blue sideband do not reduce in height while the red sideband is nearly eliminated. The baseline appears to be shifted up to $\sim 10\%$ shelving which is most likely due to poor consideration when selecting the threshold value. From Equation 15 a value of $\bar{n} = 0.3$ quanta is acheived.

After sideband cooling, Rabi oscillations on the carrier (Figure 32) show notably higher contrast than seen after only Doppler cooling (Figure 26). The following section discusses optimization methods for increasing coherence times and decreasing the cooling time.

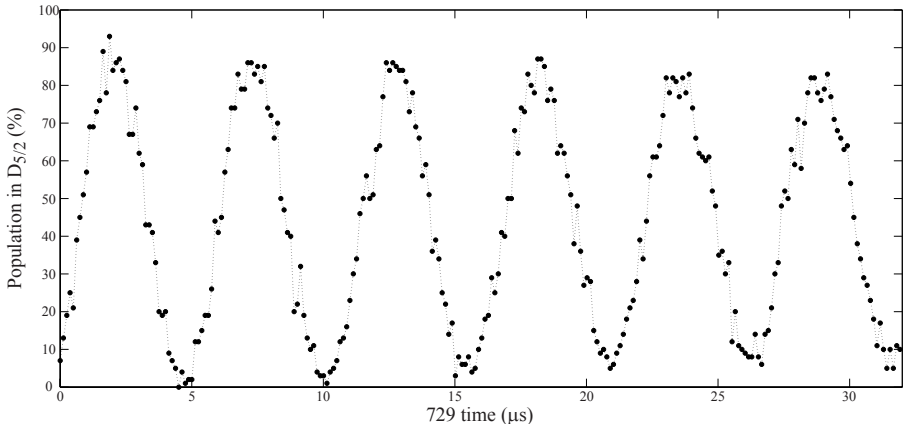

Figure 32: Rabi scan on the carrier transition after sideband cooling.

5.5 Optimization of Ground State Cooling

The coherence time of the system can be estimated based off of the contrast seen in the decoherence envelope of a Rabi scan (Figure 33). For these experiments, an estimated coherence time of 150 μs is reasonable. Generally, longer coherence times are necessary for quantum computation. Longer coherence times are also useful in molecular spectroscopy experiments because lower 729 nm saturations utilize longer π-times which give narrower peaks (due to being Fourier limited) for identification; however, if the system has decohered during this time scale, peaks will be reduced in height.

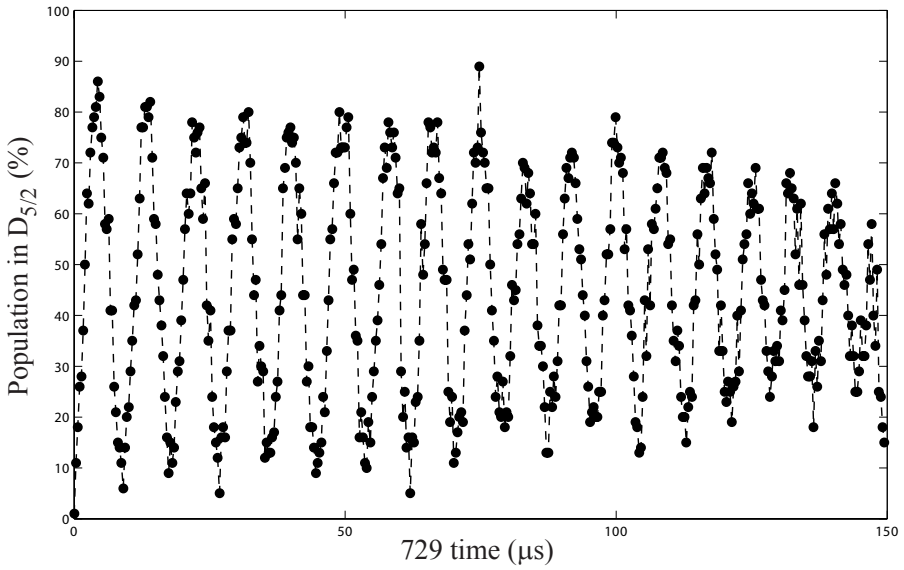

Figure 33: Rabi scan on the carrier transition showing the coherence time

In this instance, the most likely cause of decoherence is magnetic field fluctuations. Scans over the carrier transitions of the $S_{1/2}(m_j = -1/2) \leftrightarrow D_{5/2}(m_j = -5/2)$ and $S_{1/2}(m_j = 1/2) \leftrightarrow D_{5/2}(m_j = -3/2)$ peaks (without sideband cooling) showed splittings at very low saturations and long π-times. The splittings were ~ 7.3 and ~ 10.8 kHz, respectively, which is in good agreement with the relative broadenings (2 and 2.8 Bohr magneton) within the resolution of the scan. These peaks were chosen because they each have a different dependence on the magnetic field. Cavity drift experiments should utilize symmetrically shifting Zeeman components to eliminate magnetic field instability from the scan. The splittings can be seen in Figure 34.

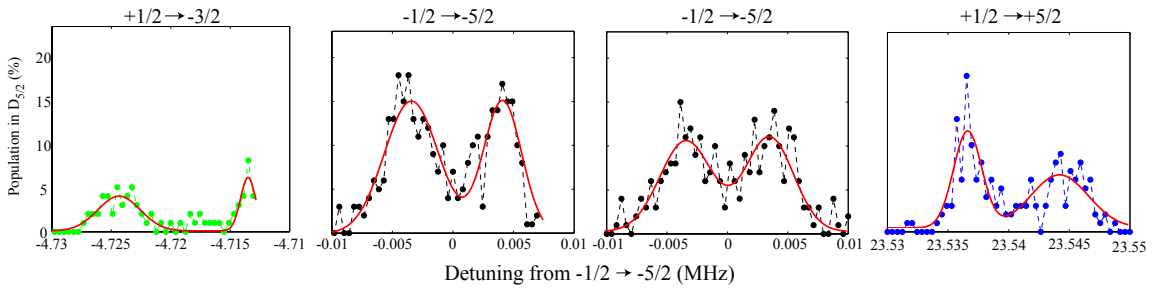

Figure 34: Splitting of different carrier transitions due to magnetic field fluctuations (A fit using the sum of two Guassians is shown in red). For $-1/2 \rightarrow -5/2$ the splitting is ~ 7.2 kHz, $+1/2 \rightarrow -3/2$ had a splitting of ~ 10.8 kHz, and for $+1/2 \rightarrow +5/2$ the splitting is ~ 7.7 kHz. These splittings appear as one large peak at faster π-times, and seem to correspond with the estimated coherence time ($1/7.3$ kHz $\approx 140\mu$s).

The decoherence is likely due to a square wave modulation causing the field to hop between two discrete values. There are several schemes within the literature for minimizing these fluctuations. One involves enclosing the apparatus in a magnetic shield of μ metal, though something must be done to also shield the ion pump which is the largest local source of magnetic field noise. Additionally, synchronizing the system to the 60 Hz AC line fluctuations have shown a reduction in line broadening from about 6 kHz to under 200 Hz [83]. Finally, further stabilization of the AC source could also be implemented by using a stable current generator typically used to drive a laser diode to source the Helmholtz coil instead of the Agilent power supply.

5.6 Sympathetic Sideband Cooling

Cooling atoms, molecules, and even macroscopic objects to the quantum mechanical ground state of their motion represents an important step towards comprehensive control of large or complex quantum mechanical systems [87]. Obtaining a sympathetically sideband cooled molecular ion has been a main goal of the Brown Lab since its inception. This technique would work in much the same way as sympathetic

Doppler cooling where energy is transferred via the Coulombic interaction; however, temperatures 1-2 orders of magnitude below the Doppler limit (540 μK) could be reached. While several species of molecular ions have been sympathetically Doppler cooled, large mass ratios between the atomic cooling ions and the molecular ions can prevent efficient sympathetic cooling of the molecular ions at temperatures near the motional ground state [87]. Therefore, initial experiments will be done on molecules close in mass to $^{40}Ca^{+}$.

Before attempting to sympathetically sideband cool a molecular ion, work was done to optimize sympathetic cooling for a second atomic ion [114]. A co-trapped $^{44}Ca^{+}$ ion was chosen due to ease of loading in the current setup and similar mass. Initial results are only for the axial center-of-mass mode of the two ion crystal. Future work will also cool the breathing mode and relevant radial modes.

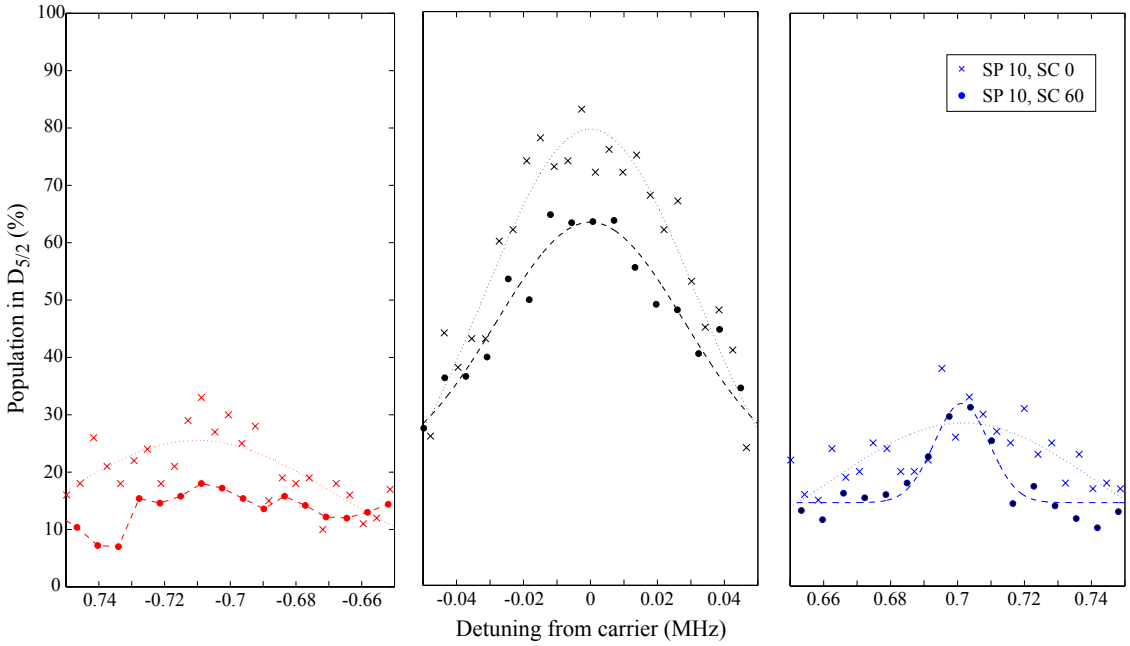

Figure 35: Motional sidebands of a mixed, two ion Coulomb crystal containing a $^{40}Ca^{+}$ and a $^{44}Ca^{+}$ ion before (crosses) and after (circles) sideband cooling loops were applied. The baseline appears to be shifted up to $\sim 15\%$ shelving which is most likely due to poor consideration when selecting the threshold value. From Equation 15 a value of $\bar{n} = \sim 0.3$ quanta is acheived, the same as seen with a single $^{40}Ca^{+}$ ion.

This first step in sympathetic sideband cooling demonstrates that extending the method to a molecular ion is a reasonable goal. The first molecular ion to be attempted should be $^{40}CaH^{+}$, due to its similar mass to $^{40}Ca^{+}$. Additionally, sideband detection experiments (Chapter 6) have shown that lighter molecules are less strongly affected by stray fields and micromotion which result in ion heating and less efficient cooling.

CHAPTER VI

IDENTIFICATION OF SINGLE MOLECULAR IONS

A prerequisite for studies of single molecular ions is an efficient method for identifying individual molecular ion species both before and after an experiment is performed [18]. A nondestructive detection technique is often desirable; in contrast, common mass spectrometry techniques are often destructive, thereby eliminating the possibility for future experiments on the now known ion. One common destructive technique used with ion traps is time-of-flight (TOF) mass spectroscopy [21], where the ions to be measured are extracted from the trap by reducing the radio-frequency amplitude. In the presence of a finite DC quadrupole potential this causes the ion trajectories to become unstable as the Mathieu q parameter enters the instability region [13]. After leaving the trap, the ions are guided to and attracted by the cathode of a channel electron multiplier, allowing the mass to be calculated based upon arrival time.

Techniques such as direct fluorescence detection are generally not applicable to molecular ions due to the lack of closed transitions [18]. Fortunately, strongly fluorescing atomic ions can serve as sensitive probes of co-trapped molecular ions. Atomic ion fluorescence is sensitive to Doppler shifts and can be used to measure the temperature or kinetic energy of a system [88, 121]. One technique, demonstrated previously, relies on a nondestructive mass measurement through the resonant excitation of an oscillation mode of the two-ion system. Within the literature are numerous instances of using the simple relation between masses of the trapped ions and their oscillation frequencies, including the most precise mass measurement of molecular ions today [122]. In contrast to such high-precision experiments, a strong Coulomb coupling between ions (the molecular ion of interest and an additional atomic ion) is essential in the

following identification schemes. The oscillation frequencies of trapped particles have been used extensively to gain information about the mass-to-charge ratio of atomic and molecular ions [7]. Observing the change in total fluorescence while exciting mass-dependent motional resonances of trapped ions is widely used for mass spectrometry of large and small ion clouds [112]. Atomic and molecular species identification via motional resonance-based detection is also possible in more complex systems, such as large multispecies ion crystals of varying size, shape, and symmetry [20, 21, 112].

This method, known as laser-cooled fluorescence mass spectrometry (LCFMS) [12], can be used to follow reactions, e.g., the multi-step photodestruction of the aniline cation ($C_6H_5NH_2^+$) [43] or the slow photodissociation of biomolecules such as glycyrrhetinic acid [44]. LCFMS has also been combined with resonantly enhanced multi-photon dissociation (REMPD) to accurately measure vibrational lines with sub-MHz precision [15, 123]. For two ion chains, LCFMS has been used to non-destructively identify a single molecular ion co-trapped with a known atomic ion by exciting the center-of-mass (COM) mode of their shared axial motion [18].

We have developed a new method for molecular ion detection using resolved sideband spectroscopy of an atomic "reporter" ion ($^{40}Ca^+$) to measure the normal mode frequencies of a two ion crystal. By probing the narrow $S_{1/2} \rightarrow D_{5/2}$ transition at 729 nm it is possible to detect sideband resonances associated with the harmonic motion of the ions. The spacings of the sidebands relative to the carrier transition relate to the ion masses as well as the effective potential in which the ions are trapped. The transitions are detected by the fluorescence depletion technique described in Section 3.3.2 involving shelving into the metastable $D_{5/2}$ state.

This chapter discusses these two methods of mass determination using mass-dependent motional resonances of trapped ions. Section 6.1 discusses using LCFMS on calcium ions and shows how it can be used to determine the mass of a nonfluorescing ion (in this case CaO^+). Section 6.2 describes resolved sideband spectroscopy

and its use in measurements of two molecular ions, CaH^+ and CaO^+.

6.1 Motional Resonance Coupling

Observing the change in total fluorescence while exciting mass-dependent motional resonances of trapped ions has a fundamentally simple methodology, whether the axial or radial mode is used for mass determination. Because they are being laser cooled, the ions are localized to within a small fraction of their equilibrium distance [114]. Due to the stronger radial potential causing the ions to align with the symmetry (z) axis of the trap, a different mass dependence exists for the axial and radial modes. For a single ion of mass m, the axial secular frequency is proportional to $\sqrt{1/m}$, while the radial secular frequencies are proportional to $1/m$ (the ratios of motional frequencies of different singly-charged species are equal to the mass ratios) [13]. In other words, the restoring force axially is independent of m but the restoring force radially is reduced as m increases [95].

The motion of the ions in the trap is excited using an oscillating electric field of variable frequency applied either to the far "endcap" electrodes or to the central trap electrodes. This is in contrast to the RF tickle compensation method described in Section 4.4 where the applied RF was applied in tandem with the RF drive frequency. The middle compensation electrodes are used for radial excitation and the endcaps for axial excitation. It is important to note that the presence of a low-pass filter will negate any tickle voltage applied for electronic perturbation of the normal modes. When the excitation field frequency is resonant with the oscillation mode of the crystal, energy is pumped into this motion. Some of this energy is distributed through the crystal via the Coulomb interaction, leading to an increased temperature of the atomic coolants and a corresponding modification in their fluorescence intensity [13].

6.1.1 Radial Determination

When working with large crystals of ions, interactions between the different ion species can shift the observed motional frequencies by a significant amount. This complicates the analysis of the experimental spectra for mixed-species ion crystals with sympathetically cooled ions that have comparable mass-to-charge ratios. Usually, the observed resonance frequencies are determined by a superposition of several, sometimes opposing, line shifting effects. These shifts can be caused by space charge effects, trap anisotropies, or the finite amplitude of the excitation field [13]. The observed frequency positions also depend on the sweep direction of the excitation field (Figure 36). For strong coupling between the ion species, this can lead to a significant shift and broadening of individual features in the spectrum so that they cannot be resolved experimentally; however, even for weaker coupling, various, sometimes more subtle, line-shifting effects can be present. Often when conducting experiments with large crystals, a comparison with a crystal simulator is necessary to enable a more accurate interpretation [13].

By comparing the radial secular frequency (ω_r) of a known ion (i.e., $^{40}Ca^{+}$) to the shifted frequency of a two-species crystal, the mass of the unknown species can be determined from the formula:

$$(M_{Ca^+})(\omega_r) = (M_{unknown})(\omega_{r,unknown}). \tag{16}$$

This works best with many ions, and requires a reference measurement be taken with the known ion before loading the unknown species. Generally this technique is more applicable for ensembles in the gas state, where the density is low and the ions are weakly interacting. Interactions between the ions in the crystalline state can significantly shift the observed frequencies [13].

Figure 37 shows the measured $^{40}Ca^{+}$ fluorescence as a function of the applied RF frequency. To produce the scan, an oscillating field is applied to the compensation

electrodes at varying frequencies until a change in atomic fluorescence is detected. This can either be a peak of increased fluorescence (where the increased motion of the ion changes the observed frequency of the Doppler cooling laser leading to higher photon counts) or a dip (where the applied field pushes the Doppler cooling lasers into the heating regime so fluorescence counts drop). This method is often used to determine the secular frequency of the trap [88]. Also, since the middle electrodes are closer to the ion than the endcap electrodes, less voltage is necessary to see a shift radially rather than axially. As little as $20 - 30$ mV_{pp} of RF can be used to see a distinct peak versus several hundred mV when the field is applied axially. Experiments consist of 100 fluorescence scans per point with the average brightness reported for each scan.

Once the radial secular frequency has been determined for a single ion, a scan involving two ions of the same species is redundant as it should yield the same value, as can be seen in Figure 38.

Thus, the two ion scan can replace the single ion scan if two ions of the same mass are being used. Here, two $^{40}Ca^{+}$ ions are used so that a molecular ion can later be loaded via reaction. Once the reaction proceeds and the molecular ion is trapped (using previously discussed molecular loading techniques), a similar experiment measure the motional modes of the co-trapped ions. Figure 39 shows how the molecular ion scans have significantly more noise than the single ion scans (as is expected for strongly coupled ion species). This could be due to poor laser cooling, or to micromotion caused by stray fields. All of the scans were done shortly after initial trapping in the Goeders Trap, so full compensation had not been completed. Future experiments performed in a fully compensated trap may yield results with less statistical variance. Additionally, as further discussed in Section 6.2.3 and shown in Figure 46, even a fully compensated trap can experience overlap between different normal modes leading to a broadening of reported peaks.

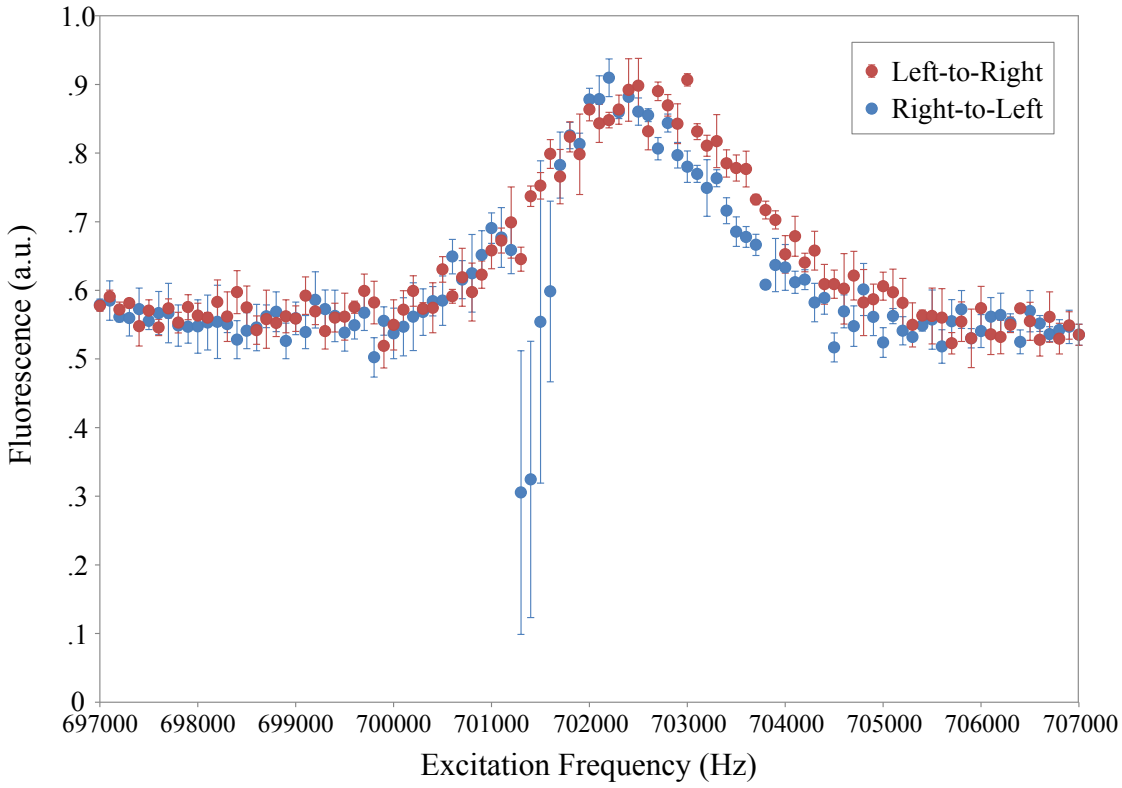

Figure 36: Comparison of the fluroescence of a single $^{40}Ca^{+}$ ion while sweeping the RF tickle frequency applied to the mid electrodes either from red to blue (Left-to-Right) or from blue to red (Right-to-Left). Notice the dip is only present when scanning from blue to red for these particular scans (and is only present in two of the three trials). Error bars are standard error of the mean.

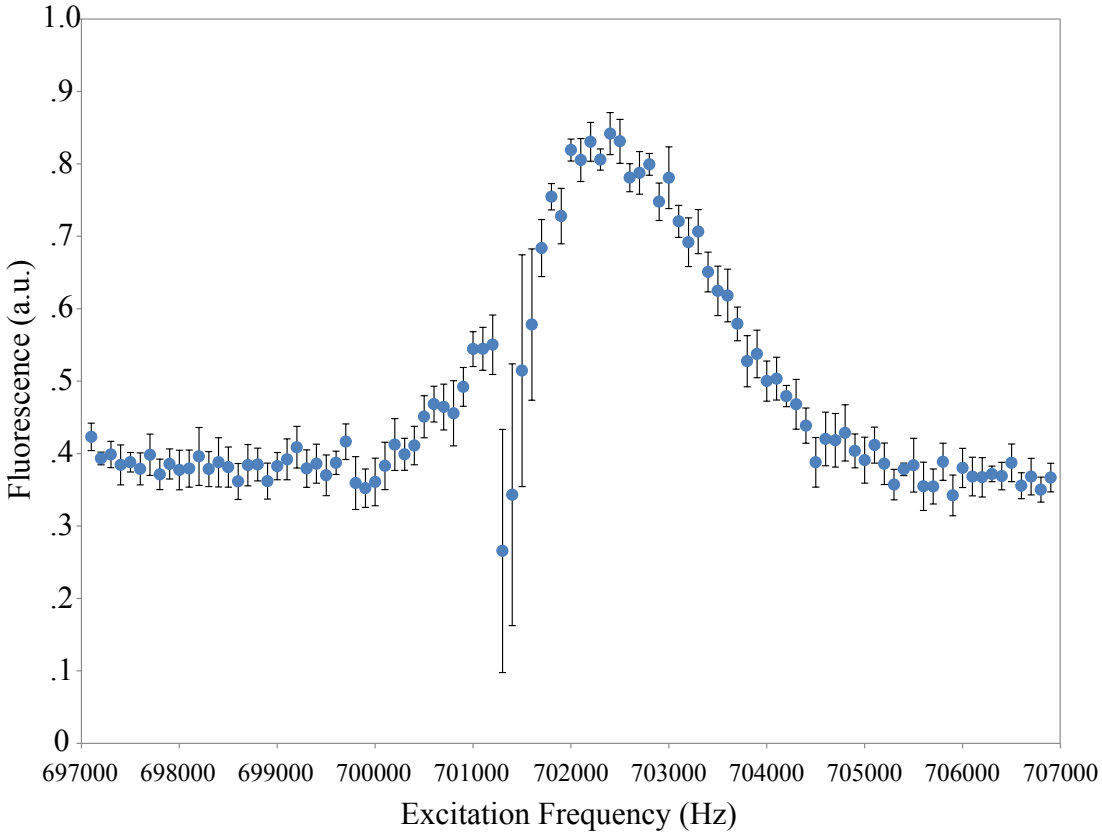

Figure 37: Fluroescence of a single $^{40}Ca^{+}$ ion while sweeping the RF tickle frequency applied to the mid electrodes. The observed peak is at 702.4 kHz. Error bars are standard error of the mean. Again the dip in fluorescence is only seen when scanning from blue to red, leading to larger error bars in this region.

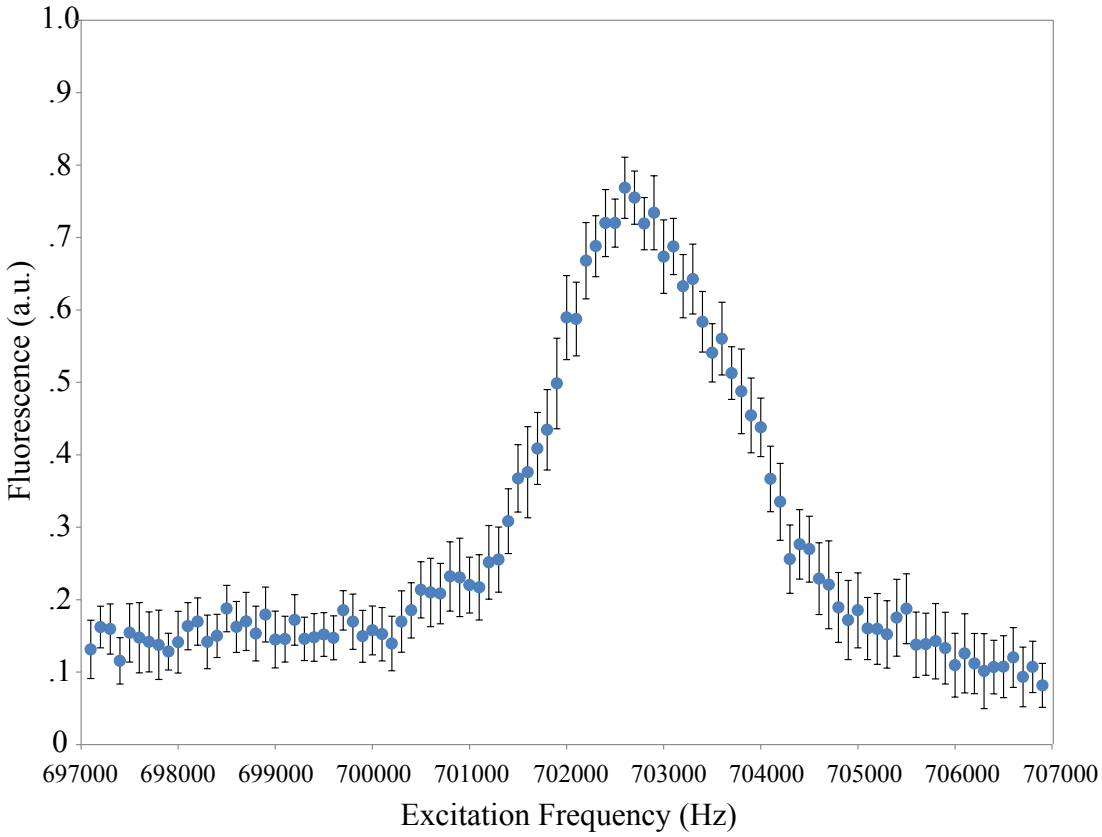

Figure 38: Fluroescence of two $^{40}Ca^{+}$ ions while sweeping the RF tickle frequency applied to the mid electrodes. The observed peak is at 702.6 kHz, as expected for the in-phase radial mode (which should not shift from the one ion case). No effort was made to find the out-of-phase radial mode. Error bars are standard error of the mean.

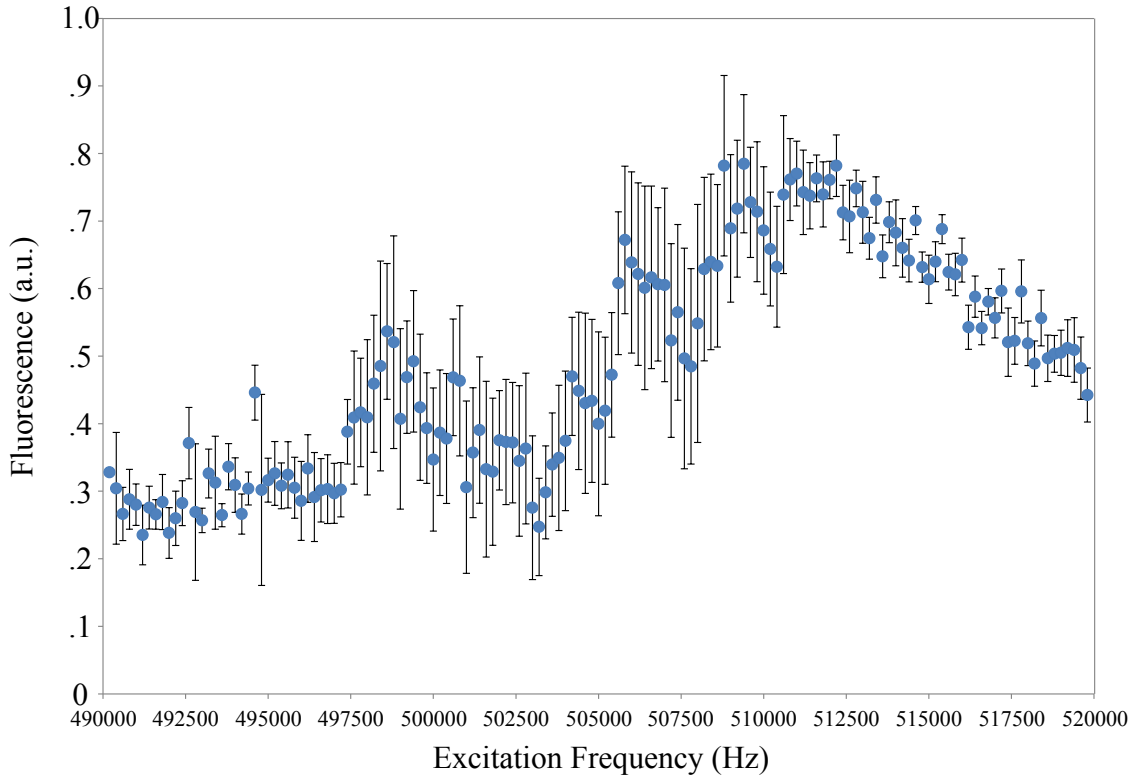

Figure 39: Fluroescence of a $^{40}Ca^{+}$ ion and a dark ($^{40}CaO^{+}$) ion while sweeping the RF tickle frequency applied to the mid electrodes. Error bars are standard error of the mean. The expected frequency for $^{40}Ca^{16}O^{+}$ is 501.6 kHz. Though it is difficult to determine a singular peak from this data, a peak centered about 511.3 kHz would lead to a mass value of 54.9 amu.

Measurements were made with the Doppler cooling lasers set to maximize fluorescence while maintaining a low likelihood of heating due to frequency instabilities ($\Delta_{397} = -40$ MHz). These are not the optimum detunings for the electrical perturbation scheme, as the heating caused by the excitation can lead to ion loss. Instead, a better scheme would be to detect resonantly, followed by a detuned cooling step (where the 397 nm detuning and power are set for optimal cooling) so that the crystal is cooled after each perturbing force experiment. This will be implemented in all future experiments.

6.1.2 Axial Determination

The simplest method of applying this perturbation consists of applying an oscillating electric field along the trap axis by adding an oscillating voltage to two diagonally positioned end electrodes. For two equally charged co-trapped ions close to their equilibrium positions, the axial normal mode frequencies (the center-of-mass mode (ν_-) and breathing mode (ν_+)) can be related to the axial frequency of a single ion, ν_1 [18, 124], by:

$$\nu_{+/-}^2 = \left[(1+\mu) \pm \sqrt{1-\mu+\mu^2}\,\right]\nu_1^2, \tag{17}$$

where $\mu = M_{Ca}/M_{unknown}$ is the mass ratio of the two ions. Then by measuring the axial frequency of a single Ca^+ ion, ν_1 (Figure 40), and the center-of-mass, ν_-, or breathing mode, ν_+, frequencies of the two ion system the mass of the unknown ion may be determined non-destructively. Again, if $M_{Ca} = M_{unknown}$, the center-of-mass mode frequency is equal to ν_1. Since two equally charged ions have identical equilibrium positions independent of their masses (if the chain is aligned axially), it is possible to measure ν_1 and ν_- with ions located at the same positions in the trap, minimizing systematic errors arising from slight anharmonicities in the trap potential (Figure 41).

The first demonstration of this method on a single molecular ion yielded a mass

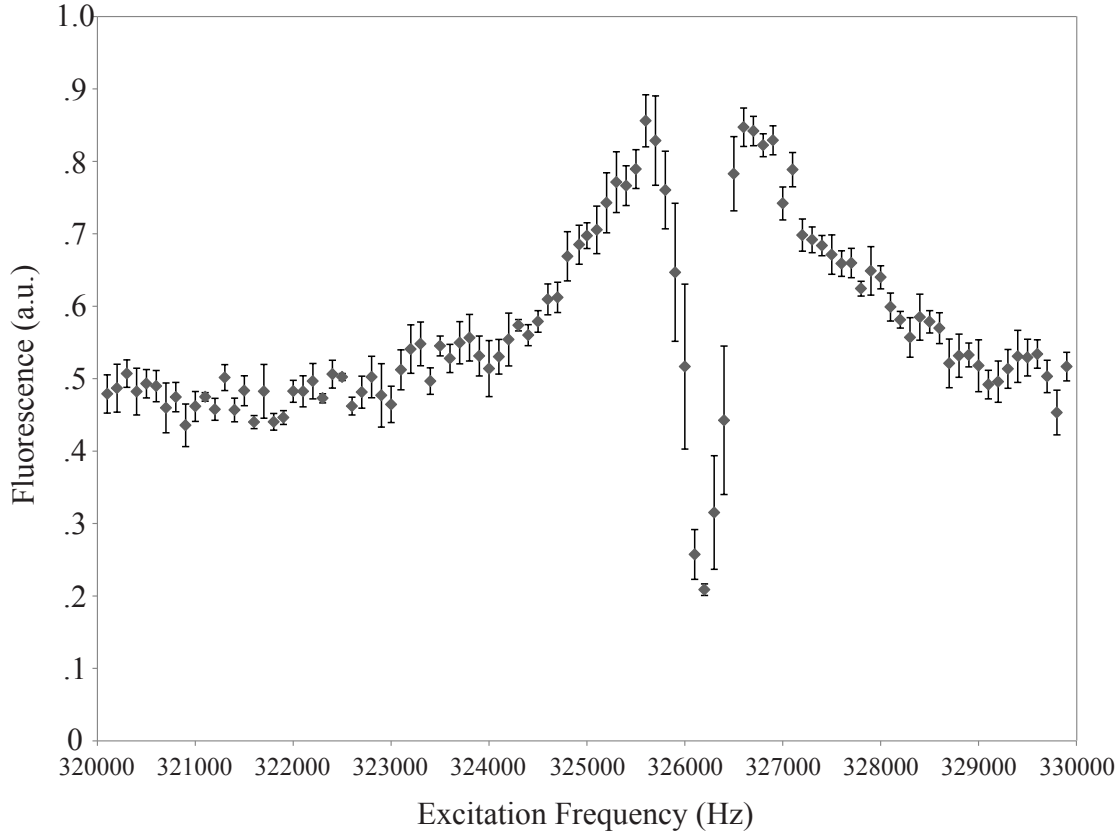

Figure 40: Fluroescence of a single $^{40}Ca^{+}$ ion while sweeping the RF tickle frequency applied to the endcap electrodes. All of the scans resulted in a dip in fluorescence about the resonance frequency. The observed peak is at 326.2 kHz. Error bars are standard error of the mean.

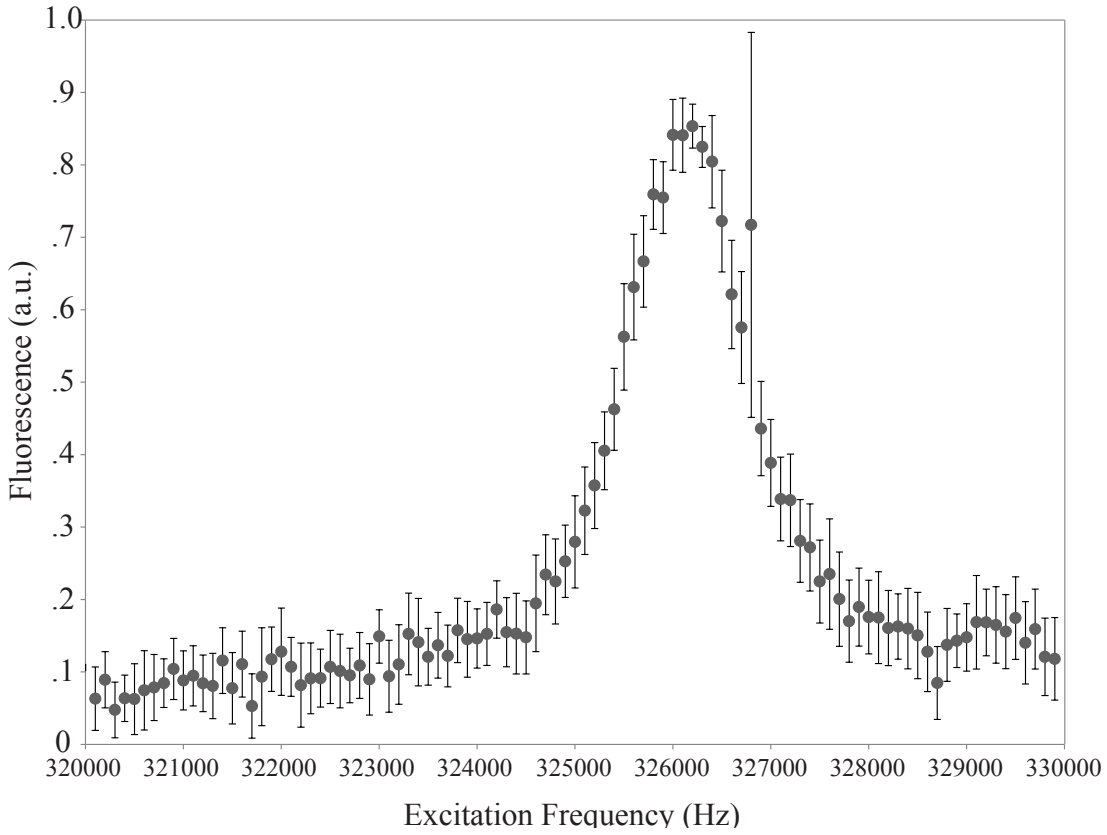

Figure 41: Fluroescence of two $^{40}Ca^{+}$ ions while sweeping the RF tickle frequency applied to the endcap electrodes. The reported peak is at 326.2 kHz (again as expected for the in-phase or center-of-mass mode). Interestingly, the single ion case seems much more likely to experience dips in fluorescence than the two ion case. Since care was taken to choose the lowest RF tickle voltage that led to a change in fluorescence, it could be that this value is not sufficient to heat the two ion pair. Error bars are standard error of the mean.

resolution of 0.18 amu for CaO^+ [18]. Though the authors noted the result was not impressive from a mass accuracy standpoint, this level of precision is sufficient to conclude that the nonfluorescing molecular ion was $^{40}Ca^{16}O^+$ as opposed to another isotopic composition of CaO^+.

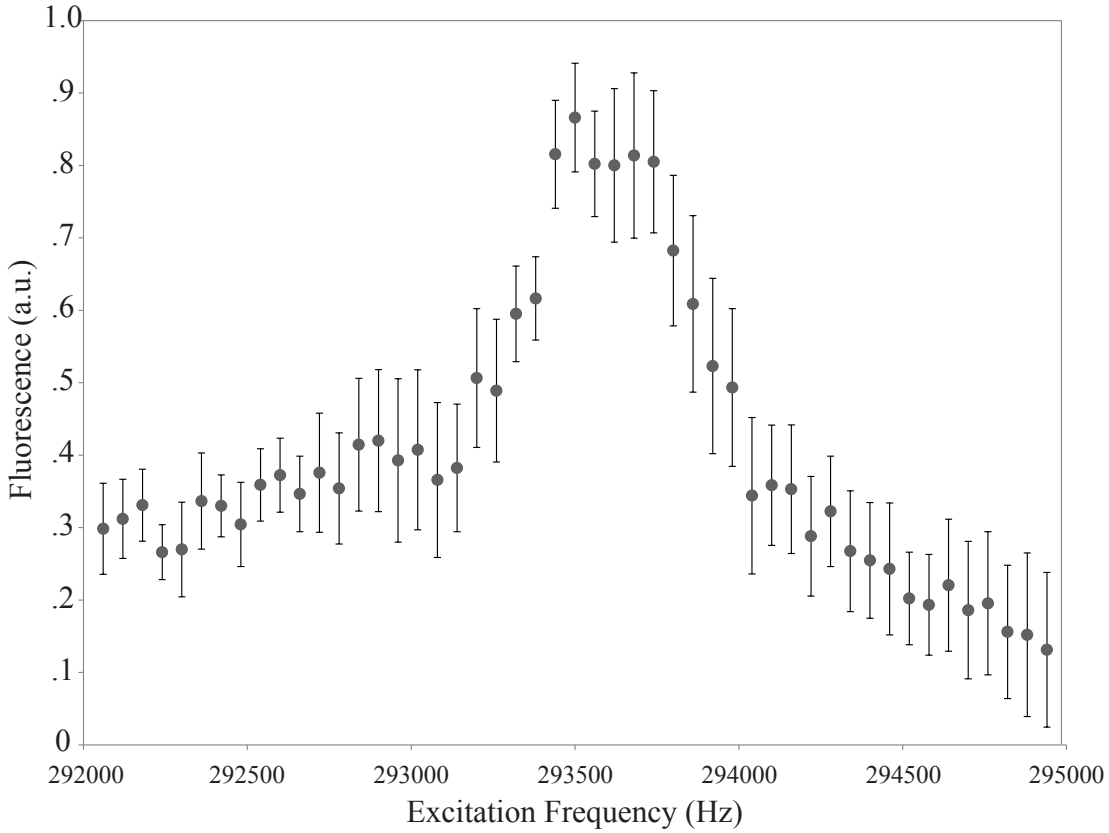

Figure 42: Fluroescence of a $^{40}Ca^+$ ion and a dark ($^{40}CaO^+$) ion while sweeping the RF tickle frequency applied to the endcap electrodes. The observed peak is at 293.6 kHz leading to a mass value of 57.3 amu. The expected frequency for $^{40}Ca^{16}O^+$ is 295.8 kHz. Though the oxygen used was not isotopcally pure, ^{16}O is overwhelmingly the most abundant isotope (99.76% vs. 0.038% for ^{17}O) so it is unlikely that the observed peak was for $^{40}Ca^{17}O^+$. Error bars are standard error of the mean.

Similar experiments carried out in the Goeders trap gave a mass value of 57.3 amu for $^{40}Ca^{16}O^+$, 1.3 amu larger than the literature value for this molecular ion (Figure 42). Several possible reasons why this method failed could include poor cooling leading to a broadening of the spectra, not taking into account the shifts seen when scanning from

different directions, or micromotion within the system mixing the normal modes. This motivated the development of new methods of making mass measurements without external perturbations.

To discriminate between equally charged atomic or molecular ions with the same total number of nucleons, a relative mass resolution of $\simeq 10^{-4}$ is typically needed [18]. This level of accuracy cannot be reached using the simple technique discussed above, since the measured resonance frequency is subject to a systematic shift of up to $\simeq 1\%$, depending on the damping effect of the laser cooling force and the trap frequency. Instead, by detecting only the in-phase component of the motion of the ions with respect to the periodic perturbing force yields a dispersive shaped signature of the trap resonance. The zero crossing of this curve yields the trap resonance frequency free of lowest order damping dependent shifts. In this manner a relative mass resolution better than $\simeq 10^{-4}$ is feasible [18]. It should be noted that, in contrast to the electrical perturbation scheme [125], the laser force modulating technique allows straightforward excitation of both the center-of-mass mode and the breathing mode, such that both the ν_- and ν_+ can be determined. With the knowledge of these two frequencies no reference measurement of ν_1 is needed in order to determine M_2, allowing for direct measurement of the ion of interest.

6.2 Resolved Sidebands

The electric perturbation method is often the preferred means for finding dark ion mass data since it has a simple procedure, is applicable in a large variety of experiments, and has been shown to be a sensitive measurement for a number of experimental conditions [18]. However, to reach sensitivity beyond general isotope differentiation (i.e., the observe the mass difference between $^{42}Ca^+$ and $^{40}CaD^+$ ions) the technique requires the addition of laser force modulation, and even this may not provide the resolution necessary. Additionally, this technique requires the system to be

heated which can lead to ion loss, particularly in surface traps which have lower trap depths. Alternatively, by taking advantage of techniques optimized for sideband cooling experiments, dark ion mass values can be obtained with precision that depends solely on the linewidth of the laser driving the transition, magnetic field stability of the system, and the transition's natural linewidth.

6.2.1 Single Ion Mass Measurements

In this set of experiments, the resolved sidebands of an atomic "reporter" ion ($^{40}Ca^{+}$) are used to measure the normal mode frequencies of a two ion crystal. The narrow $S_{1/2} \rightarrow D_{5/2}$ transition is probed using a 729 nm laser; in addition to the main carrier, sideband resonances associated with a change of the motional state of the ion crystal are also observed. These motional states can be resolved due to the strong confinement of the RF trapping potential relative to the transition linewidth. As with the electric perturbation method, the sideband frequencies relate to the masses ($^{40}Ca^{+}$ and the "unknown" ion) as well as the potential in which the ions are trapped. Since only Doppler cooling is performed on the Coulomb crystal, a value of $\overline{n} \sim 20$ motional quanta can be placed on the motional state occupancy for these experimental conditions, which is approaching the Doppler limit. This mode measurement serves as a first step towards high-precision molecular ion Quantum Logic Spectroscopy [27, 126], and can also be used to determine the mass of an unknown target ion.

Figure 43 shows the resolved sideband spectrum of the $S_{1/2}(m_j = -1/2) \rightarrow D_{5/2}(m_j = -5/2)$ transition for two trapped $^{40}Ca^{+}$ ions. The plot is an average over ten scans. The two-ion system here presented has six normal motional modes: an in-phase mode and out-of-phase mode for each spatial dimension. In the axial direction these are the center-of-mass (COM) and breathing modes (BM), while for the radial modes the in-phase motion is labeled R (radial center-of-mass) and the out-of-phase is labeled T (tilt mode). For the trap parameters used in these experiments, the pairs of radial

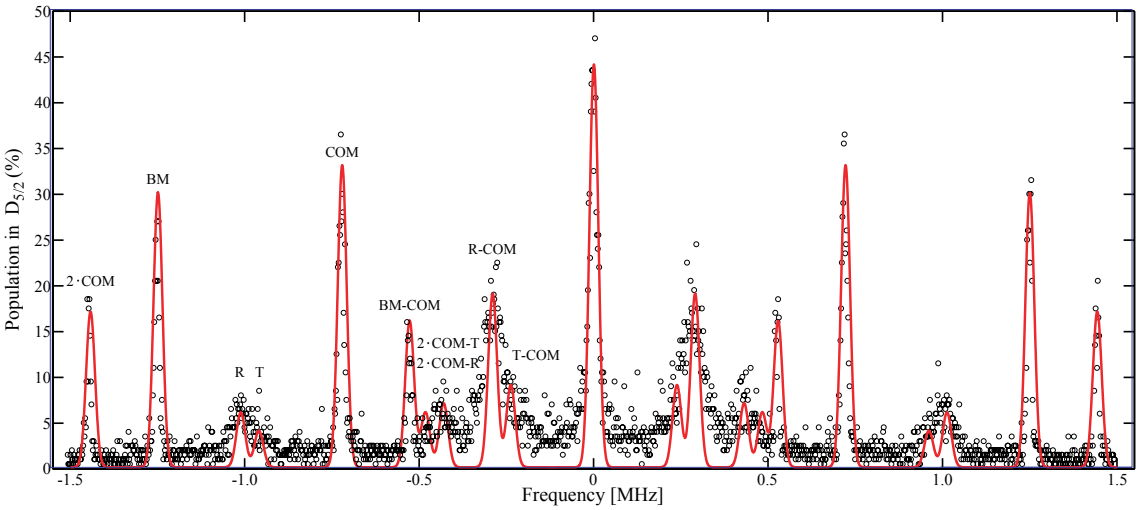

Figure 43: A frequency scan of two laser cooled $^{40}Ca^{+}$ ions with transitions identified. Gaussian peaks are added to guide the eye and highlight the overlap peaks. In addition to the carrier (0 MHz), a series of motional sideband peaks are excited at frequency offsets corresponding to the center-of-mass mode (COM, 0.72 MHz), the radial modes (R, 1.008 MHz), the tilt modes (T, 0.96 MHz), the breathing mode (BM, 1.24 MHz), and combinations of these modes [95].

and tilt modes are nearly degenerate, and the modes often overlap. The harmonics of these modes, as well as combined excitations, can also be identified. The ratio of the breathing mode and axial mode are in experimental agreement with Eq. 17 ($\omega_{BM} = \sqrt{3}\omega_{COM}$).

When a second ion is loaded into a compensated trap, the modes shift according to Eq. 17 due to the change in mass. Given the single $^{40}Ca^{+}$ mode, it is possible to use either the COM or BM of the two ion system to calculate the mass of the dark ion. Alternatively, one can also calculate the mass using the harmonics of either mode. The first axial harmonic for $^{40}Ca^{+}$ and two molecular ions are shown in Figure 44. Combining the data from the first and second harmonics results in a more accurate mass measurement (as shown in Table 4), and a mass accuracy of 0.2 amu is achieved.

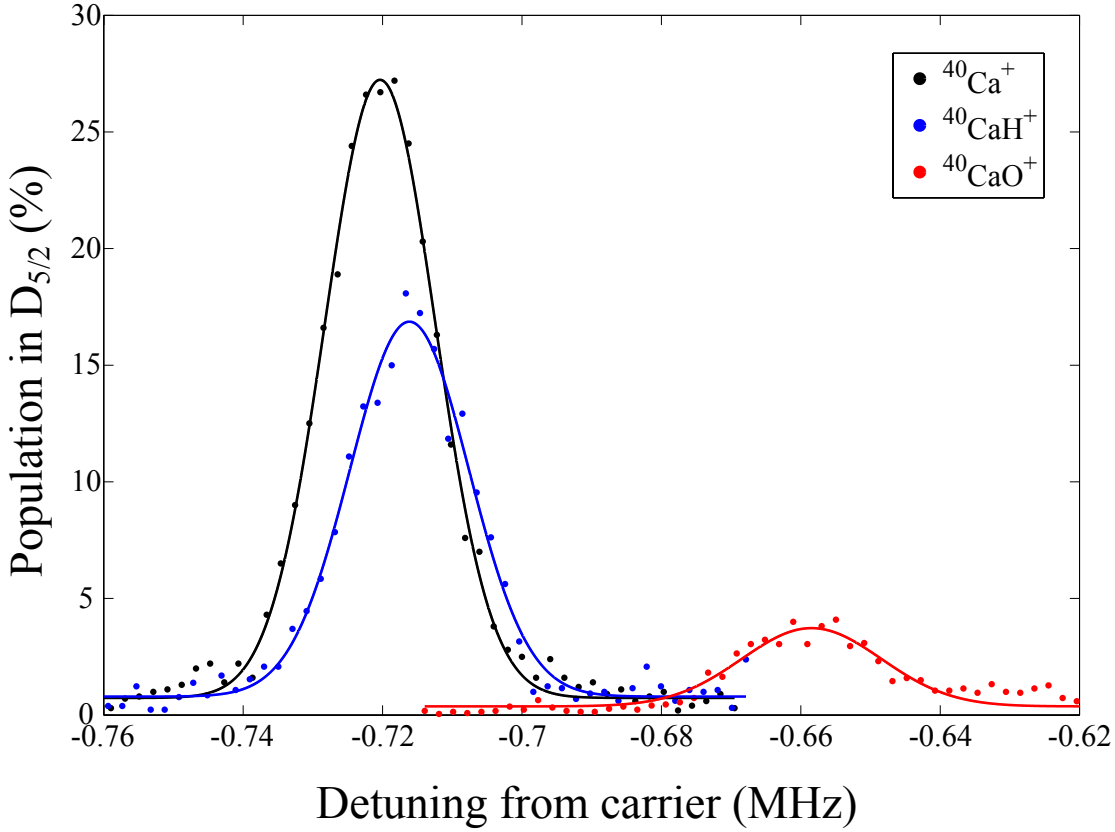

Figure 44: Frequency spectrum of the first-order red axial center-of-mass mode sideband of a Doppler cooled $^{40}Ca^{+}$ with $^{40}CaH^{+}$ or $^{40}Ca^{16}O^{+}$. Solid lines are Gaussian fits [95].

Table 4: Experimental determination of mass for the first, $\nu_{\mathrm{COM},1}$, and second, $\nu_{\mathrm{COM},2}$, harmonics of the axial center-of-mass mode. The experimental mass, m_{exp}, is calculated from the average value of the frequency, $\bar{\nu}_{\mathrm{COM}} = (\nu_{\mathrm{COM},1} + \nu_{\mathrm{COM},2}/2)/2$, using Eq. 17. m is the mass as reported in the NIST Reference Database 144 based on Ref. [127].

Ion	$\nu_{\mathrm{COM},1}$	$\nu_{\mathrm{COM},2}$	$\bar{\nu}_{\mathrm{COM}}$	m_{exp}	m
$^{40}CaH^{+}$	0.71611(8)	1.4326(2)	0.7162	40.97(6)	40.9769
$^{40}CaO^{+}$	0.6582(5)	1.295(3)	0.6527	56.16(6)	55.9570

6.2.2 Limits to Mass Precision

A secular frequency of 0.72 MHz results in an axial center-of-mass sideband spacing of 80.3 Hz for $^{40}CaD^+$ and $^{42}Ca^+$, as the two species have a mass difference of only 0.018 amu. Obviously, by increasing the secular frequency this shift will become larger, but current experimental evidence in the Goeders trap shows ion instability for axial secular frequencies larger than ~ 1.2 MHz (which only increases the separation to 134 Hz). These limitations are due to the applied RF voltage, as the current voltage being applied is nearing the limit for the RF amplifer. Without increasing the radial secular frequencies (currently at 1.008 MHz), the higher axial secular frequencies will begin to dominate. By improving the helical resonator, higher amplification of the RF voltage will be possible allowing for greater axial secular frequencies.

As shown in Section 5.5, the 729 nm transition can currently be narrowed to ~ 4 kHz. Unfortunately, to get a spacing of > 4 kHz between the ions of interest would require increasing the axial secular frequency above 40 MHz, which would lead to even larger radial secular frequencies to keep the same geometry, so this is highly unlikely. Secular frequencies of 5 MHz can be achieved realistically, so in order to distinguish $^{40}CaD^+$ and $^{42}Ca^+$ the width of the peak needs to be > 1 kHz. The linewidth is mainly limited by magnetic field instability and insufficient locking electronics, but with improvements it may be possible to get the laser narrow enough to distinguish this separation, as Blatt *et al.* have reported linewidths on the order of 10 Hz [116]. At this level magnetic field stability is the main limitation, so getting to single Hz linewidths may require using a transition in $^{43}Ca^+$ which is insensitive to magnetic fluctuations.

6.2.3 Effect of Stray Fields

Initial experiments only took data for $^{40}Ca^+$ ions, and then the two easiest molecular ions $^{40}CaH^+$ and $^{40}CaO^+$. When it was discovered that $^{40}CaO^+$ data was far from the

expected value, repeated measurements were taken. Again, the same systematic shift in the sideband frequency from the expected value was reported. It was then decided to use the other stable isotopes of calcium as test masses to map out the region between $^{40}CaH^+$ and $^{40}CaO^+$. It is possible to use the center-of-mass (COM) and the breathing mode (BM) frequencies to make a mass measurement that is independent of the reference vibrational frequency. The dimensionless variable ξ is defined as:

$$\xi = \frac{\nu_+^2 - \nu_-^2}{\nu_+^2 + \nu_-^2}. \tag{18}$$

When Eq. 17 holds this can be rewritten in terms of the mass ratio μ

$$\xi = \frac{\sqrt{(1 - \mu + \mu^2)}}{1 + \mu}. \tag{19}$$

Because Eq. 17 is not valid for this case, Eq. 19 no longer holds (as clearly exhibited in Figure 47). By examining the deviation from Eq. 17 and using a set of test masses it is possible to determine the strength of the stray electric field and further compensate the trap. For test masses, the even isotopes of calcium are used. Any naturally abundant isotope can be loaded into the trap, but with the current experimental setup only the even isotopes can be identified spectroscopically via fluorescence with a second set of 397 nm and 866 nm lasers [88]. The hyperfine structure present in $^{43}Ca^+$ requires additional laser frequencies to observe fluorescence. Experimental test data and data for $^{40}CaH^+$, $^{43}Ca^+$ and $^{40}Ca^{16}O^+$ are presented in Figure 45 and Table 5. Figure 45 shows broader peaks for $^{48}Ca^+$ and $^{40}CaO^+$. These peaks are Doppler broadened due to heating that arises from the excess micromotion expected for heavier masses in an uncompensated trap.

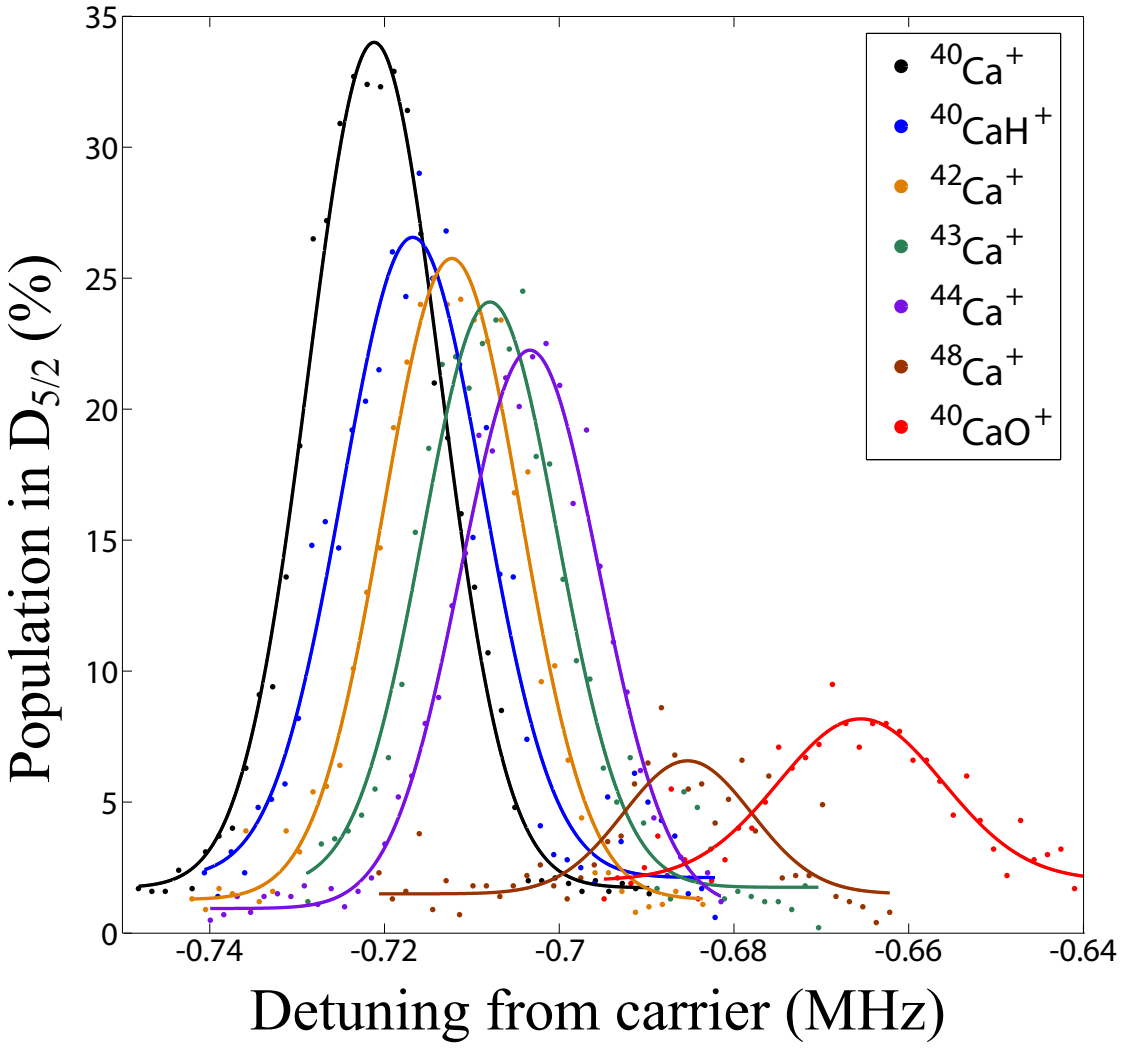

Figure 45: 729 nm frequency scan of the first-order red axial center-of-mass mode sideband of a Doppler cooled $^{40}Ca^+$ with one of the following target ions:$^{40}Ca^+$,$^{40}CaH^+$,$^{42}Ca^+$,$^{43}Ca^+$,$^{44}Ca^+$,$^{48}Ca^+$,$^{40}CaO^+$. Solid line is a Gaussian fit.

Table 5: Comparison of the measured normal mode frequencies (MHz) in a stray field to the expected normal mode frequencies without a stray field.

Ion	COM Calculated	COM Measured	BM Calculated	BM Measured
$^{40}Ca^+$	0.7213	0.7213(2)	1.2493	1.2478(3)
$^{40}CaH^+$	0.7168	0.7168(1)	1.2417	1.2407(6)
$^{42}Ca^+$	0.7124	0.7122(2)	1.2346	1.235(1)
$^{43}Ca^+$	0.7079	0.7078(3)	1.2278	1.2353(2)
$^{44}Ca^+$	0.7035	0.7032(4)	1.2213	1.2288(8)
$^{48}Ca^+$	0.6863	0.6850(6)	1.1986	1.236(9)
$^{40}CaO^+$	0.6540	0.6653(4)	1.1644	-

Table 6: Axial normal mode frequencies for two ions in a compensated trap. The reported BM frequency of $^{40}CaO^+$ is a single Gaussian fit to the overlapped T and BM frequencies (see Figure 46)

Ion	COM Calculated	COM Measured	BM Calculated	BM Measured
	Sec. Freq.(MHz)	Sec. Freq.(MHz)		
$^{40}Ca^+$	0.5194	0.5194(4)	0.8996	0.8992(4)
$^{44}Ca^+$	0.5066	0.506(1)	0.8794	0.878(1)
$^{48}Ca^+$	0.4942	0.4933(9)	0.8631	0.8601(6)
$^{40}CaO^+$	0.4709	0.4807(4)	0.8385	0.8230(4)*

Eq. 19 can be used when peak identification is possible and there are no stray fields. Figure 47 compares experimentally measured values of ξ using Eq. 18 to the values expected from Eq. 19, and for a compensated trap there is good agreement (except for CaO^+). The CaO^+ data is in disagreement because three unresolved modes form a broad peak. Plotting the expected normal mode frequencies as a function of mass (Figure 46), shows that the measured CaO^+ frequency assigned to the breathing mode lies between the expected values of the tilt modes and the breathing mode. For simplicity, the pair of tilt modes have been treated as degenerate. A calculation of the normal modes in three dimensions allows one to determine mass ranges where difficulties may be expected. A less exact method is to use the frequencies calculated from Eq. 17 and the radial frequencies of each ion individually. As the mass of the two ions becomes more distinct, the radial mode frequencies become similar to the radial mode frequencies of each ion individually, with the frequency of the lighter mass

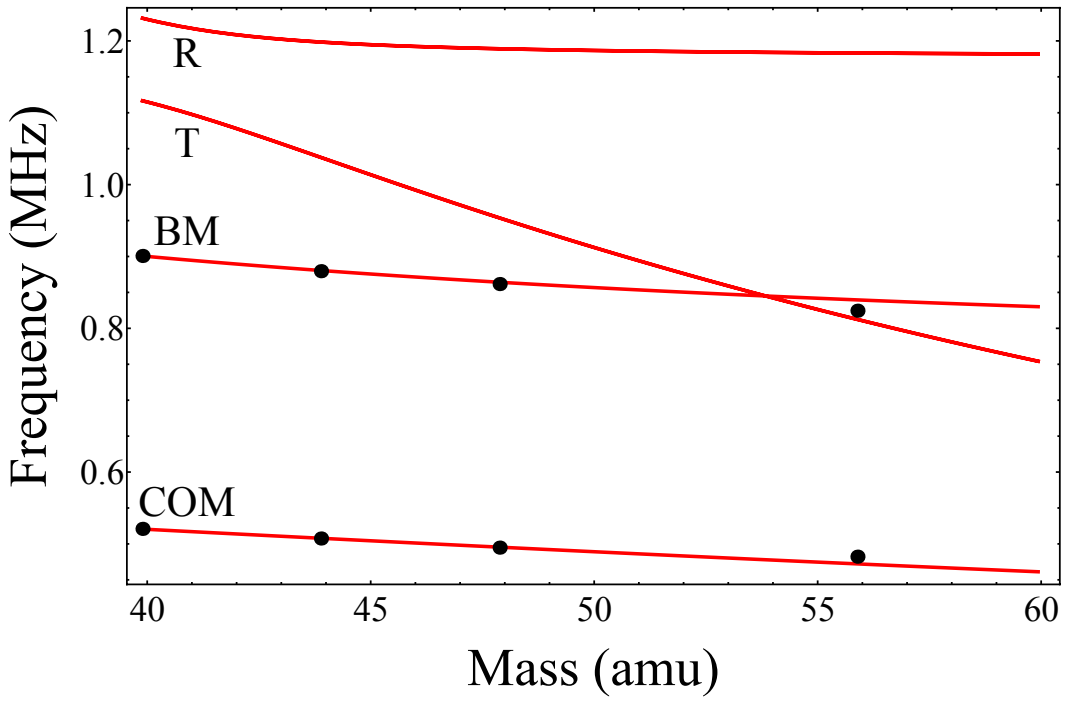

Figure 46: Normal modes in a fully compensated ion trap. Red lines represent the expected normal modes without a stray field. Data points correspond to $^{40}Ca^{+}$, $^{44}Ca^{+}$, $^{48}Ca^{+}$, and $^{40}Ca^{16}O^{+}$. Notice the $^{40}Ca^{16}O^{+}$ data point between the T and BM lines which equates to the center of two Gaussians [95].

reduced and the frequency of the heavier mass increased. This simple method can be used to estimate potential frequency overlaps and helps in selecting the appropriate ratio of axial and radial frequencies.

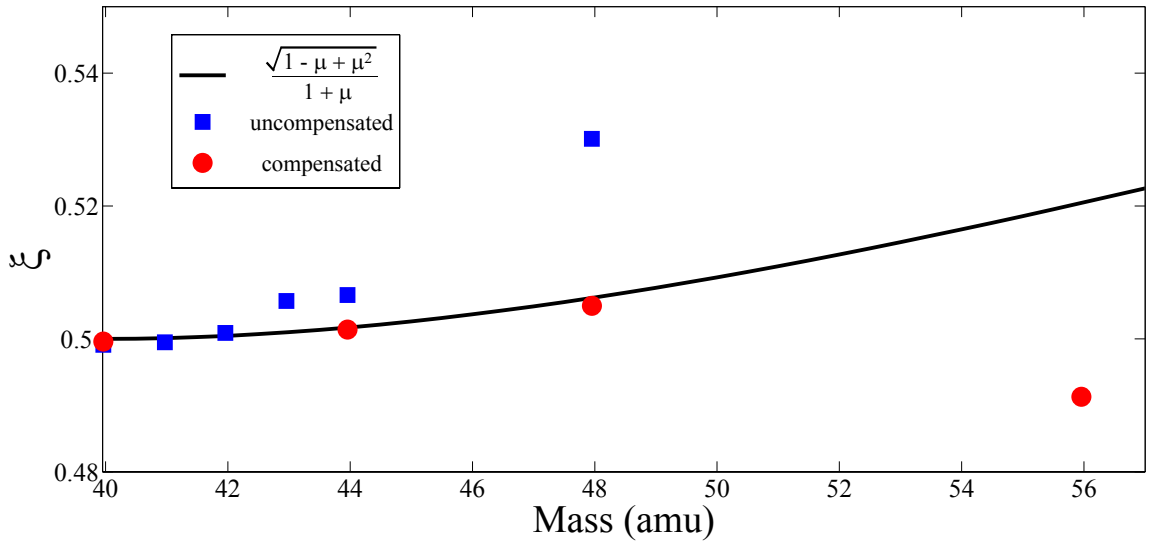

Figure 47: ξ as a function of mass of the target ion. For a compensated trap (red circles) there is good agreement with Eq. 19 (the line) except for $^{40}CaO^+$. This is due to spectral overlap of the T modes and the BM leading to an error in the extracted frequency (see text and Fig 46). If there is a stray electric field (blue squares), the mass derived from Eq.19 will be incorrect.

CHAPTER VII

SPECTROSCOPY OF SINGLE IONS

Quantum Logic Spectroscopy (QLS) transfers information between two trapped ions, a logic ion and a spectroscopy ion, through the quantized vibrational motion of the crystal. The logic ion serves as a quantum sensor for detecting transitions in the spectroscopy ion [27]. Initialization in QLS experiments requires cooling of the vibrational modes of the crystal to the ground state, which is achieved by addressing the motional sidebands [63]. One drawback of QLS is the requirement of ground-state cooling, which adds significant experimental complication. Moreover, QLS is difficult to apply to complicated systems because it relies on narrow optical transitions in the spectroscopy ion, which must be accessible by continuous-wave laser sources. For most ion systems, such a resonance is unavailable or, through spontaneous emission, leads to dissociation away from the measurement basis [64].

High precision spectroscopy outside of the strong-binding limit is challenging since the spectroscopy laser induces detuning dependent heating and cooling which can distort the transition lineshape. Recently, experiments in the weak binding limit have been performed using low intensity spectroscopy laser beams on a chain of sympathetically cooled ions [28, 30, 31]. Sympathetic cooling removes the heating limitation by counteracting the back action of the interrogating lasers. High resolution is achieved by calibrating the probe laser to an absolute frequency by referencing it to a frequency comb, or using the comb light directly [29]. Ion fluorescence is measured directly, as the constant sympathetic cooling absorbs the minimal heating due to the low intensity probe lasers.

In the same manner that the coupled motion of ions in the trap can be used to

determine mass information (and sympathetically cool other ions), it is possible to connect the frequency-dependent laser-induced heating of a sympathetically cooled spectroscopy ion with changes in the fluorescence of a laser-cooled control ion [88]. There are two main methods for measuring ion heating via fluorescence: comparing the ratio of the red and blue motional sidebands [118], and Doppler recooling [121]. These two techniques can also both be used to extract spectroscopic data from single ions.

Sideband spectroscopy is the conventional technique for characterizing motional states, and it has been used to characterize the heating of ions in the absence of cooling [63, 84, 118, 121, 128, 129, 130]. However, it is more complicated to implement experimentally than Doppler cooling, requiring more laser beams. Also requires a low phonon number, hence it is not applicable with low secular frequencies or large heating rates. As such, Doppler recooling, a simpler method, was the first method used for spectroscopy, demonstrated using two isotopes of calcium. Estimated heating rates have been found to agree reasonably well with results obtained using the Raman sideband technique, which is not sensitive to collisional heating. For sidebands, the ion is allowed to heat for only a few milliseconds, thereby gaining a few motional quanta. In contrast, the Doppler recooling method is based on heating periods on the order of seconds, allowing the ion to gain many motional quanta [121].

7.1 Sympathetic Heating Spectroscopy

In this work, the frequency dependent heating of a spectroscopy ion is measured by observing the fluorescence of a second ion (control ion) as the system is recooled [88, 131]. Even a low scattering rate of photons from the spectroscopy ion can create a significant stochastic optical force that builds up quickly with the laser interaction time (t_{heat}), and dramatically changes the trajectory of both ions. This results in a large Doppler shift of the control ion which can be observed in the recooling process. Laser Induced

Fluorescence (LIF) experiments using similar low laser intensities would require long photon counting times to acquire line profiles with signal to noise adequate for detection. As such, SHS is an effective tool to study dipole transitions that are weak or fall in regions of the electromagnetic spectrum where the sensitivity of detectors is marginal or non-existent.

Initially, the two ions are trapped (Figure 48). By turning off the laser-cooling on the control ion and applying a near-resonant laser to the spectroscopy ion, the two-ion system will be heated for a time t_{heat}. The resulting laser heating is measured by blocking the spectroscopy laser and monitoring the fluorescence of the control ion as it recools. The $^{40}Ca^{+}$ lasers are detuned from resonance ($^{40}\Delta_{866} = 20$ MHz and $^{40}\Delta_{397} = -30$ MHz) with intensities fixed to yield saturation values of $^{40}s_{866} = 1000$ and $^{40}s_{397} = 8$. In the absence of ions in the trap, the photon counter reads $\sim$ 500 photons/second of background scattering at these laser intensities. The $^{44}Ca^{+}$ repumper laser has a fixed detuning $^{44}\Delta_{866} = 20$ MHz, while the $^{44}\Delta_{397}$ is varied to obtain spectra for a range of laser intensities. The relative isotope shifts for $^{44}Ca^{+}$ are 842 MHz and -4.5 GHz for the $S_{1/2}$-$P_{1/2}$ and $D_{3/2}$-$P_{1/2}$ transitions, respectively [132].

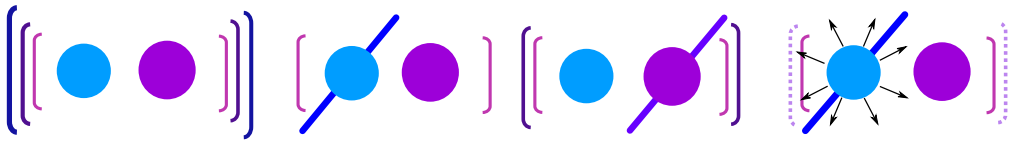

Figure 48: Procedure for Sympathetic Heating Spectroscopy. The solid circles represent the two ions, the brackets represent the magnitude of vibrational energy in the Coulomb crystal, and the diagonal line represents an applied laser beam. (a) First, the spectroscopy ($^{44}Ca^{+}$) and control ($^{40}Ca^{+}$) ions are trapped. (b) The Coulomb crystal is then laser cooled via the control ion. (c) By simultaneously switching off the cooling laser and turning on the heating laser, the Coulomb crystal heats for a fixed interaction time. (d) Finally, the magnitude of heating is observed by measuring the fluorescence of the control ion as the crystal recools.

Doppler recooling curves are obtained for a range of t_{heat}, laser intensities, and detunings. Two representative curves are shown in Figure 49 illustrating the return of the $^{40}Ca^{+}$ fluorescence to steady state as the ions are cooled. In comparison, a third curve shows that without spectroscopy lasers there is no visible heating at $t_{\text{heat}} = 250$ ms. Each of the three curves is an average of 20 individual experiments and the data points measure the number of photons collected in a time t_{bin}. Depending on the experimentally observed fluorescence, t_{bin} is chosen to be between 3 and 8 ms to ensure that most of the trajectories reach a steady-state fluorescence. Recooling lasers remain on for an additional 500 ms (t_{int}) between experiments to ensure that the system is initialized.

An SHS signal is expected when $^{44}\Delta_{397} > 0$, the region of the fluorescence spectra where Doppler heating dominates. In the Doppler cooling regime $^{44}\Delta_{397} < 0$, the laser cools the ion and reduces the Doppler shift to below the natural linewidth. As a result, the observed fluorescence can be described assuming the ion is motionless. For SHS, the ion is heated by the scattered photons and the resulting Doppler shift

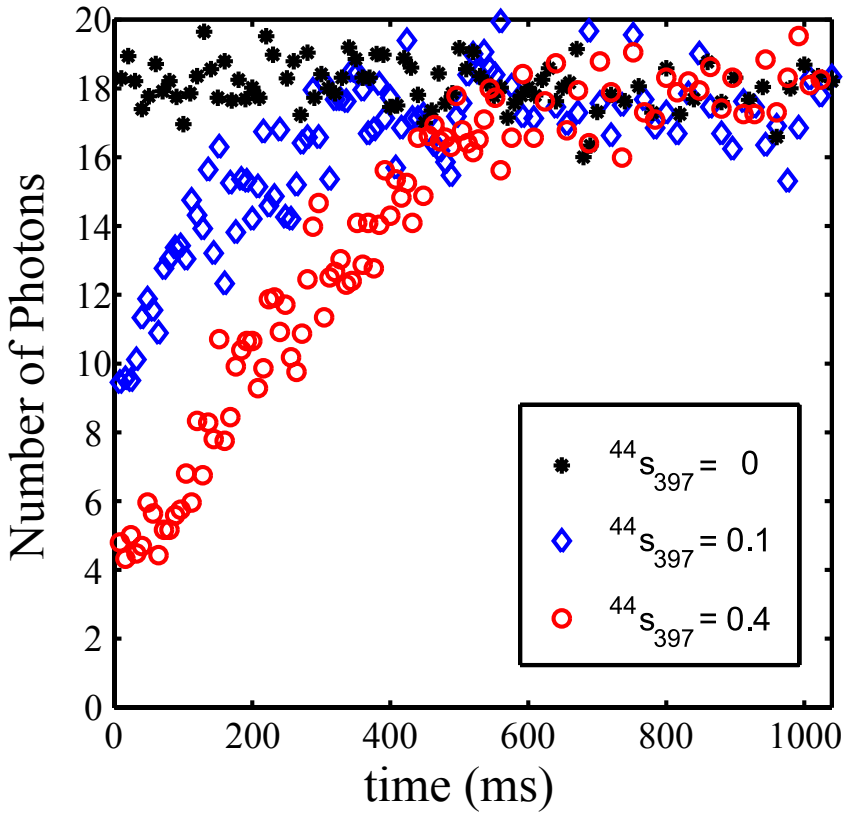

Figure 49: Doppler recooling fluorescence vs. laser-induced heating parameters. In two heating situations, lasers are kept at ${}^{44}\Delta_{866} \approx 20$ MHz, ${}^{44}\Delta_{397} \approx 40$ MHz, ${}^{44}s_{866} = 0.5$, and 250 ms heating times. Blue diamonds and red circles show recooling after laser induced heating is applied on the spectroscopy ion with intensities proportional to ${}^{44}s_{397} = 0.1$ and ${}^{44}s_{397} = 0.4$, respectively. The black points show no deviation from steady-state fluorescence after turning off all lasers for the same period of time. Each time dependent curve is the average of 20 fluorescence trajectories. The ordinate shows the mean number of photons detected in 8 ms.

dramatically changes the scattering rate.

The heating and recooling is stochastic, and the individual experiments show a variety of behaviors for the same laser parameters. To simplify the measurement, P_{heat}, the percent of experiments where there is noticeable heating at short times, is reported. To calculate P_{heat}, the average number of photons in the first three data points is compared to a threshold value, $T = \langle\Gamma_c\rangle t_{\text{bin}} - 2\sigma$, where $\langle\Gamma_c\rangle$ is the steady-state scattering rate and σ is the standard deviation of the Poissonian distribution. If the signal is below the threshold, the experiment is marked as heating. False positives

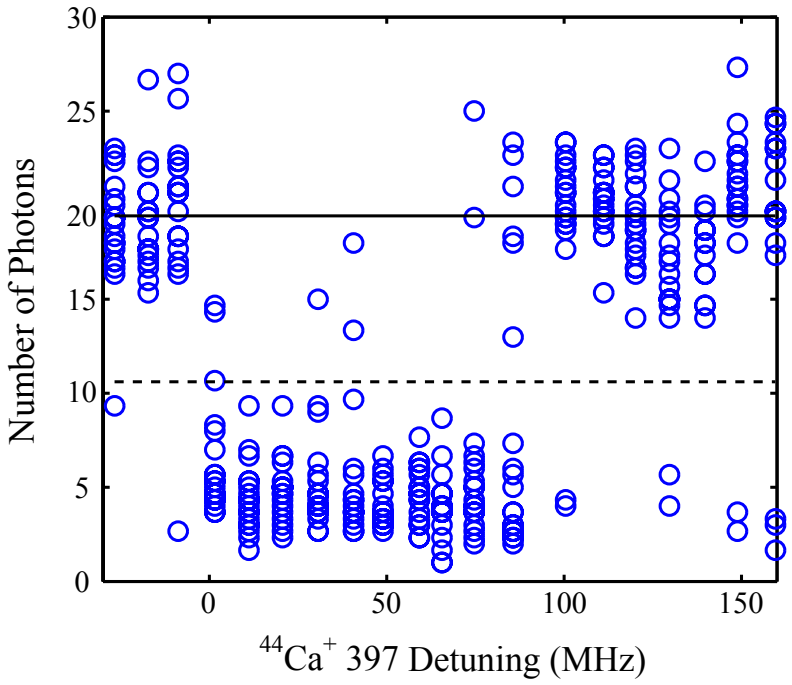

Figure 50: Average of the first 3 fluorescence points for 20 Doppler recooling trajectories versus heating laser detunings. The ordinate shows the average number of photons detected in 8 ms. The solid black line shows the average steady-state fluorescence for a cold crystal. The dotted black line represents the threshold, which is 2σ from the average of the steady-state fluorescence and is used to determine whether heating is observed during the experiment (spectroscopy laser parameters: ${}^{44}\Delta_{866} = 20$ MHz, ${}^{44}s_{866} = 0.5$, and ${}^{44}s_{397} = 0.4$).

for cases without heating occur less than 2.5% of the time. An example of applying this threshold to experimental data is shown in Figure 50. A clear distinction between heating and no heating is observed.

7.1.1 Limits of SHS

For a typical photon detection efficiencies, very few photons are registered in a single experiment. Therefore, many experimental cycles consisting of a heating period and a cooling period must be repeated [121]. This results in the heating rate of the trap limiting the amount of laser induced heating that can be detected. For a single ion in the Urabe trap, no heating is measured for times as long as 20 seconds. For two ions, a small amount of heating is observable at 1 second, corresponding to a

$P_{\text{heat}} \approx 10 - 30$ and an ion temperature of approximately 7 K. This is probably due to micromotion for the poorly compensated 2 ion crystal. Figure 51 shows that for very low laser powers ($^{44}s_{397}$=0.01 and $^{44}s_{866} = 1 \times 10^{-3}$), the P_{heat} spectrum has a signal to noise ratio of ~ 2. The predicted LIF spectrum at these conditions is shown in Figure 51, together with a simulation of the photon counting noise associated with the dark counts of the device employed in these experiments. The number of scattered photons (I_{LIF}) is at least 9 times smaller than the photon shot noise. One way to overcome the shot noise would be to average over more than 7000 experiments. Alternatively, an increase in the collection efficiency will reduce the time required to obtain a LIF spectra. For SHS, the same detection improvement would similarly enhance the ability to distinguish laser induced heating from trap heating.

A SHS signal is observed when the calculated optimal fluorescence would result in at most 1500 photons per second being scattered into a solid angle of 4π [88, 131]. This is very dim compared to the millions of photons per second typically scattered by alkaline earth ions. Experiments with extremely low heating powers, corresponding to a maximum fluorescence of a few hundred photons from the spectroscopy ion, resulted in indistinguishable signal from the case without heating lasers. The 1500 photons/s number is an upper bound on the limit for this technique, as it was calculated for resonance excitation using a three-level model; a proper analysis of the amount of scattered photons would require a model of the entire eight level system (the two Zeeman levels of the $S_{1/2}$ and $P_{1/2}$ states and the additional $D_{3/2}$ level which is split into four Zeeman components [75]).

The current work uses a simple metric, P_{heat}, to measure the heating in a two ion Coulomb crystal. This reveals the approximate line position but does not provide a clear method for determining the linewidth. The resolution of the spectrum is limited by the accumulative stochastic heating mechanism. A better understanding of the distribution of ion energies after heating and during the recooling process may allow

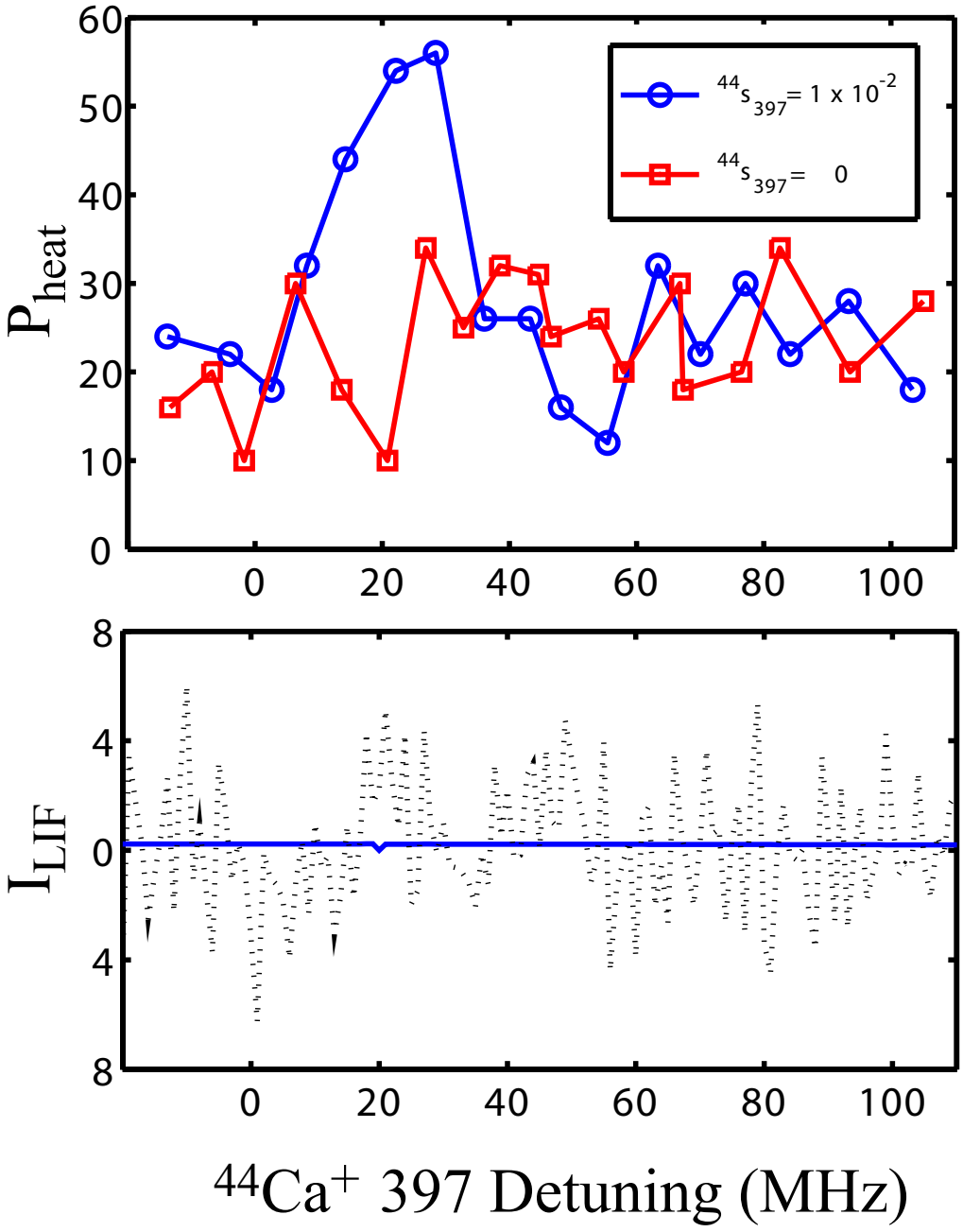

Figure 51: Comparison of a low power SHS spectra with simulated LIF signal. (a) The blue circles show a SHS spectra for ${}^{44}s_{397} = 0.01$ and ${}^{44}s_{866}=1\times10^{-3}$ with $t_{\text{heat}} = 1$ s, $t_{\text{bin}} = 3$ ms, and ${}^{44}\Delta_{866} = 20$ MHz (averaged over 20 experiments). The background P_{heat} measurements without heating lasers are shown by the red squares. Lines are to guide the eye. (b) The predicted LIF spectrum with a $t_{\text{meas}} = 1.89$ s is shown in blue for comparison. The dotted black line is a simulation of the shot noise corresponding to the dark counts of the experimental device (50 counts/sec).

for the extraction of the transition dipole moment. Potentially, SHS can become an effective tool to study dipole transitions that are weak or fall in regions of the electromagnetic spectrum where the sensitivity of detectors is marginal or nonexistent. Future work will include developing a Monte Carlo simulation that accounts for the effect of stochastic scattering of photons on the ion motion.

7.1.2 Improvements of Experimental Setup

The photon scattering rate and laser heating are most strongly affected by the power of the 397 nm laser. The maximum signal is detected with ${}^{44}\Delta_{397}$ between +10 and +70 MHz. The spectra have a sharp rise at zero detuning, and the width of the peak reduces with laser power resembling a standard LIF spectra. For certain laser intensities and detunings, the three-level system shows fine features arising from both resonance with dressed states and coherent population trapping [133].

The experimental signal during a single recooling cycle will consist of an initial deviation from the steady state scattering rate. For all of the SHS experiments, the ${}^{40}Ca^{+}$ lasers are detuned ${}^{40}\Delta_{866} = 20$ MHz and ${}^{40}\Delta_{397} = -30$ MHz from resonance. The ${}^{44}Ca^{+}$ repumper laser has a fixed detuning ${}^{44}\Delta_{866} = 20$ MHz, while the ${}^{44}\Delta_{397}$ is varied to obtain spectra for a range of laser intensities. These may not have been the ideal detunings for optimal measurement. Instead, the optimal detuning is decided as a compromise between recooling signal and ability to recool atoms that have been highly excited [121]. Experimental results have shown that low detuning is indeed favorable, and the ${}^{40}Ca^{+}$ detunings would ideally be at ${}^{40}\Delta_{397} = \Gamma/2 = -11$ MHz and ${}^{40}\Delta_{866} = 0$ MHz from resonance (though the value of the 866 nm laser detuning is less important).

Laser intensities were fixed to yield saturation values of ${}^{40}s_{866} = 1000$ and ${}^{40}s_{397} = 8$. A lower laser beam intensity will give a larger signal for a given heating period since the average initial energy is proportional to the power-broadened linewidth.

This suggests using the smallest feasible laser intensity, requiring a compromise with respect to robust cooling and detector dark counts. This leads to an ideal saturation parameter close to 1 [121].

In order to determine the limits of observable heating, the laser powers were decreased and the heating time extended. The time to extract a certain amount of energy increases with atom temperature (Figure 52). The heating period should be chosen long enough to get a significant signal, but the optimal heating period must be decided based on other experimental parameters such as trap depth, trap heating rate, and background gas collision rate. It is also important to have sequential time bins that are short compared to the total time required for the cooling process [121]. The P_{heat} line profiles not only increase in height, but also broaden. For long heating times the red edge of the peak is within 10 MHz of the $S_{1/2}$-$P_{1/2}$ transition (blue circles and red squares). This is not the case as the heating time is reduced (green diamonds). Therefore, heating times on the order of 100 ms appear ideal for the experimental conditions.

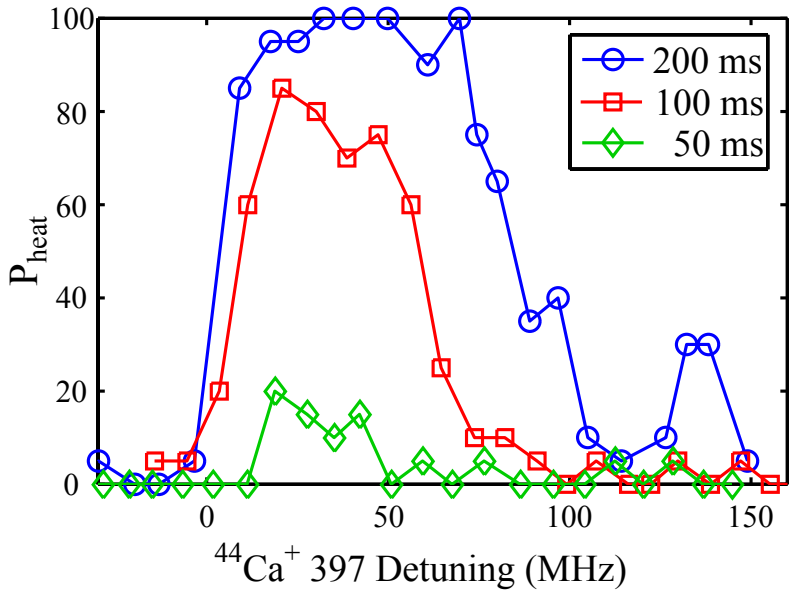

Figure 52: The effect of varying t_{heat} on SHS spectra. The intensity of the 397 spectroscopy laser is proportional to ${}^{44}s_{397} = 0.03$, and the heating repumper laser is tuned to ${}^{44}\Delta_{866} = 25$ MHz with a saturation value fixed at ${}^{44}s_{866} = 0.5$. Lines shown are to guide the eye.

7.2 Quantum Sympathetic Heating Spectroscopy

From the early results on sympathetic sideband cooling and the success of SHS, a possible middle ground between QLS and SHS has been proposed, where the atomic sidebands of the reporter ion are used to determine the temperature (Quantum Sympathetic Heating Spectroscopy, or Q-SHS). Even without reaching the ground state of motion with a molecular ion, SHS can be extended by using sideband heating measurements as a more sensitive probe than Doppler recooling curves [118]. This represents a logical extension of the work presented in this thesis since the resoled sidebands have already been shown as a method of detecting and identifying nonfluorescing ions as well as a well-established technique for high-resolution temperature experiments. This intermediate technique may be able to resolve the peak centers of

the Fe^+ lines between $234 - 260$ nm for comparison with high-redshift astronomical data [134].

Q-SHS will allow for the detection of even lower scattering rates than SHS, approaching the limit of a single photon scattering event demonstrated by QLS [27]. With no further optimization of sideband cooling, a scattering rate of $\sim$ 10 photons/s could be detected using sideband heating measurements. This number is based off of being able to resolve a change of 0.5 quanta via the ratio of the red and blue sidebands. Additional work in increasing the signal-to-noise ratio should allow for 0.1 quanta resolution, which would bring the resolution of Q-SHS to the single photon level.

Two separate experiments could be run using Q-SHS with little additional experimental setup. First, a direct extension of SHS that again monitors the 397 nm transition of $^{44}Ca^+$; or second, a measurement of the $S_{1/2} \rightarrow D_{5/2}$ transition in $^{44}Ca^+$ which has not yet been characterized. Initial experiments investigating the 397 nm line would allow for optimization of experimental parameters as well as giving an upper bound for the sensitivity limit of this technique. The second experiment measuring isotope shifts of the $S_{1/2} \rightarrow D_{5/2}$ transition in less abundant calcium isotopes would allow for closure on the experimental lines. The hyperfine $^{43}Ca^+$ atom is the only isotope that has been measured to date [85]. That result was obtained by switching the laser from ν_{40} to ν_{43} by locking the laser to a TEM_{00} cavity mode three modes higher ($\nu_{n+3} = \nu_n + 3\Delta_{FSR}$) than for $^{40}Ca^+$ and adjusting its frequency with an AOM. By utilizing a widepass EOM for the 729 and 854 nm lasers, it will be possible to probe the narrow transition in both the $^{40}Ca^+$ and the $^{44}Ca^+$ so that a reference measurement may be made while the laser is locked to the $^{40}Ca^+$ resonance. Additional work with $^{42}Ca^+$ and $^{48}Ca^+$ would also be possible with sufficient bandwidth.

CHAPTER VIII

CONCLUSIONS AND OUTLOOK

This thesis has focused on the initial requirements for building a lab to do molecular spectroscopy. Ion traps were constructed explicitly for the purpose of molecular ion work, both in regards to current experiments with low heating rates and large optical access, but also future experiments which may require multiple loading zones or incorporation of Zeeman or Stark slowers or ablation targets. The Goeders trap was demonstrated to reliably trap ions, with dark lifetimes of several hours observed, and the ability to be properly compensated for micromotion with only two additional electrodes. A new technique for identifying stray electric fields was presented, which also indicated that experimenters must stay cognizant of the normal modes of a crystal when selecting secular frequencies for both the atomic coolant ion as well as the molecular ion of interest. Without appropriate calculation, the heavier ion may experience a mixing a modes leading to ion heating and a broadening of transitions. Sideband cooling of an atomic ion to its motional ground state was demonstrated, as well as the many possible pitfalls that may preclude reaching the ground state. An extension to sympathetic sideband cooling of a second ion to $\bar{n} < 1$ was done to eliminate first order Doppler effects that would arise during spectroscopic investigation. Finally, a new spectroscopic technique was demonstrated where measurements can be performed using either Doppler recooling curves or resolved sidebands. In the coming years, these techniques will be extended to perform spectroscopy of CaH^+. Further goals will involve direct laser cooling of a BH^+ ion.

8.1 Resolved Sideband Mass Spectrometry

The ability to identify an unknown ion using motional mode spacing has been shown previously using resonance excitation. The move to resolved sideband spectroscopy provides a number of improvements. First, the system as a whole is no longer perturbed, so ion loss from external heating is non-existent. The speed of the measurement is also increased since the excitation time is on the order of μs. Additionally, the absolute mass accuracy is dependent on the natural linewidth of the transition (on the order of 1 Hz). Laser linewidths of 10 Hz have been reported [116], giving mass resolution below 0.02 amu which could be used to distinguish a $^{42}Ca^+$ ion from a $^{40}CaD^+$ molecule.

Perhaps the most overlooked advantage of the resolved sideband identification technique is that no reference measurement must be made to the control ion. Instead, the motional sidebands of the two ion crystal can directly be probed. This is especially useful if the ions are loaded in a manner other than chemical reaction. Assume the molecular ion is being loaded via ablation; it has been noted that ablating a target with a high powered laser can lead to dips in the RF voltage, which would necessarily lead to ion loss. If instead the molecular ion were loaded first via ablation and then the atomic coolant ion were loaded, no reference measurement would be possible. With the resolved sideband method, order of loading is not important.

8.2 Measuring Vibrational Overtones of CaH^+

Currently, all information describing the rovibrational structure of CaH^+ is from theoretical studies. *Ab initio* studies have been done on vibrational dipole moments of $^{40}CaH^+$ (Figure 53), with proposals on using these lines for a precise measurement of m_e/m_p [54, 135].

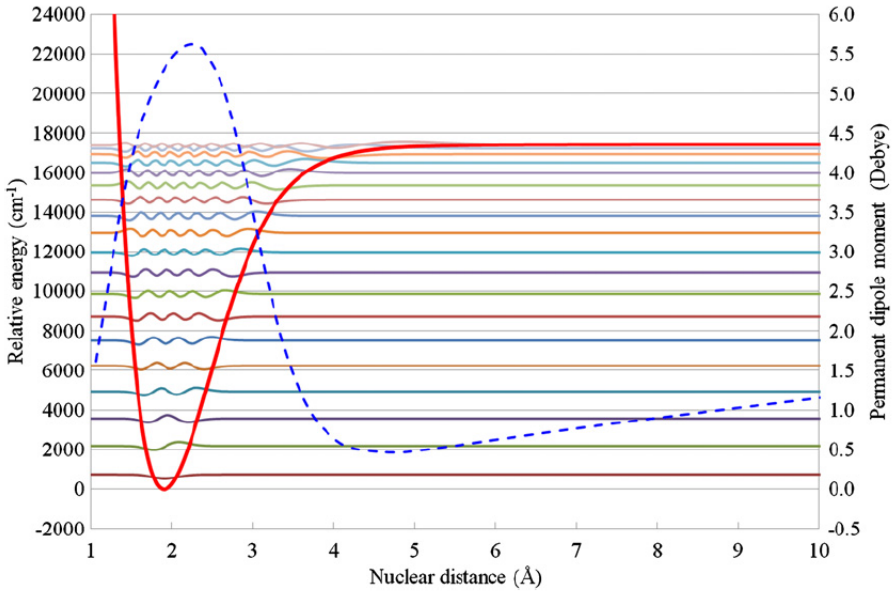

Figure 53: Potential energy curve of the ground state of $^{40}CaH^+$ with vibrational wavefunctions $\Psi_\nu(R)$(colored lines) and the permanent dipole moment function $\mu(R)$(the blue dashed line). Figure reproduced precisely as in Ref [135]

.

Though published results only reach $\nu = 4$ [135], unpublished results indicate vibrational overtone lines in the range of a Ti:Sapphire laser. These transitions include:

- $X^1\Sigma(\nu, J) = (0, 0) \rightarrow (9, 0) = 883.3$ nm
- $X^1\Sigma(\nu, J) = (0, 0) \rightarrow (10, 0) = 813.3$ nm
- $X^1\Sigma(\nu, J) = (0, 0) \rightarrow (11, 0) = 757.9$ nm.

With these overtone transitions, the dipole moments should be very small, but the higher order transitions should be accessible with intense lasers. A Ti:Sapph laser can output approximately 2 W of power, so it may populate these vibrational states. Initial experiments will involve trapping and sympathetically cooling a $^{40}CaH^+$ ion with several $^{40}Ca^+$ ions. Identification of the $^{40}CaH^+$ can be done with either of the mass spectrometry techniques listed in Chapter 6, though the sideband method may

be preferable to avoid heating the crystal and losing the molecular ion. After proper identification of $^{40}CaH^+$, REMPD spectroscopy can be attempted on these overtone transitions.

By taking advantage of a known dissociation channel for CaH^+ at 272 nm [115] a $1 + 1'$ REMPD experiment should be possible to confirm vibrational overtones. Combining the IR Ti:Sapphire laser with a UV tripled YAG at 355 nm will lead to dissociation when the Ti:Sapph laser is tuned near the predicted vibrational transition. The YAG alone will not dissociate the ion, or will dissociate on a timescale observably slower than the two photon process. Fluorescence imaging will be used to verify an increase in atomic ion fluorescence verifying the dissociation of the molecule. Future work will involve narrowing the linewidth of the pulsed IR laser and eventually getting very narrow transition data via Q-SHS.

APPENDIX A

SOLID WORKS DRAWINGS

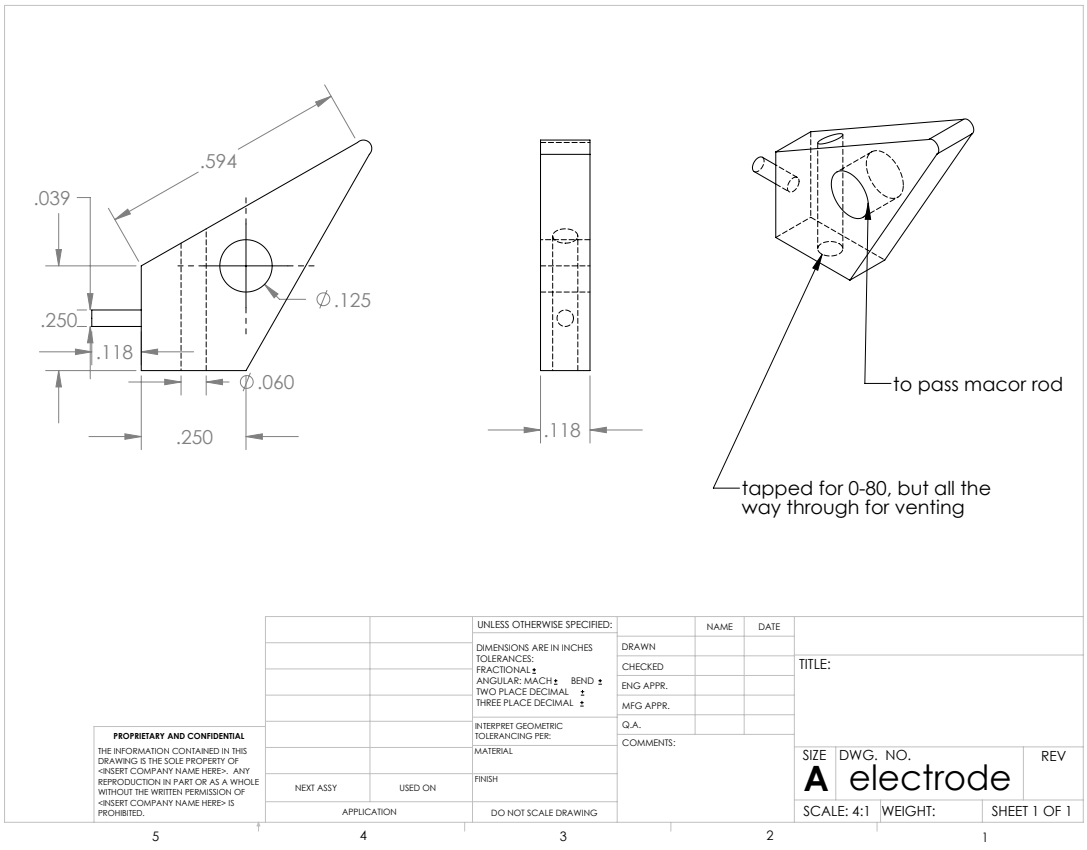

Figure 54: Goeders trap DC electrode

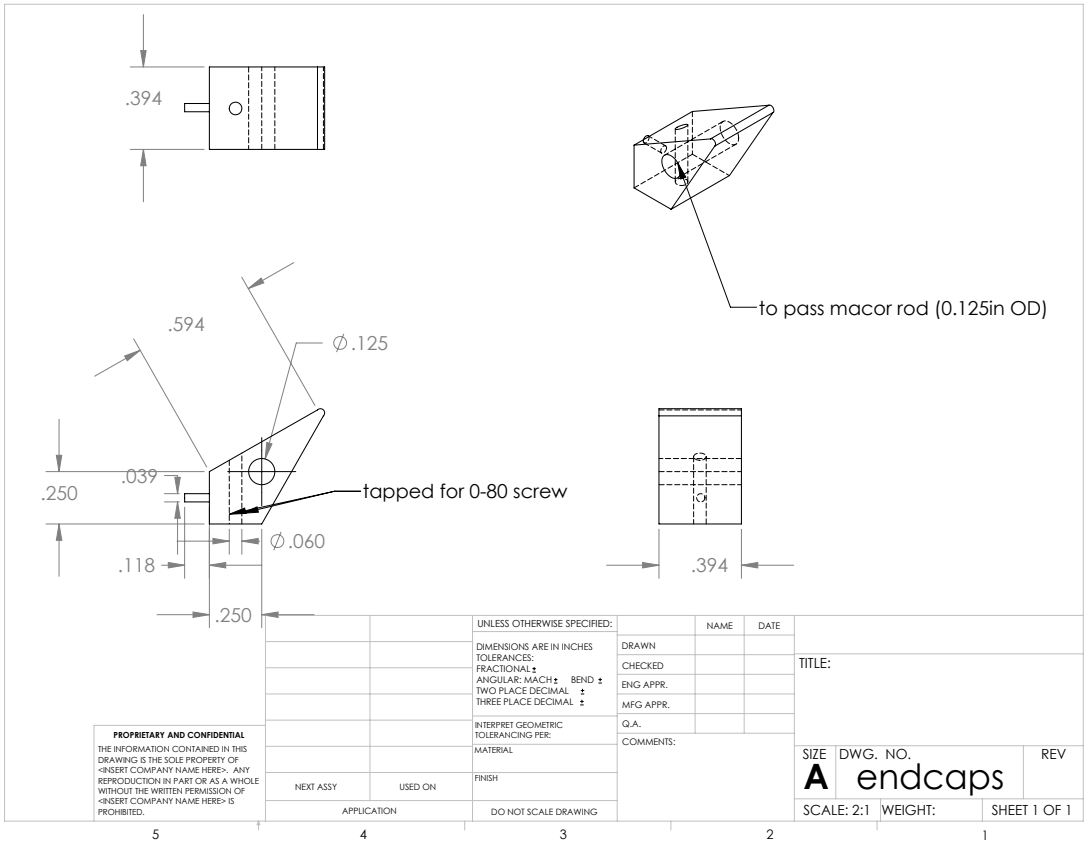

Figure 55: Goeders trap endcap

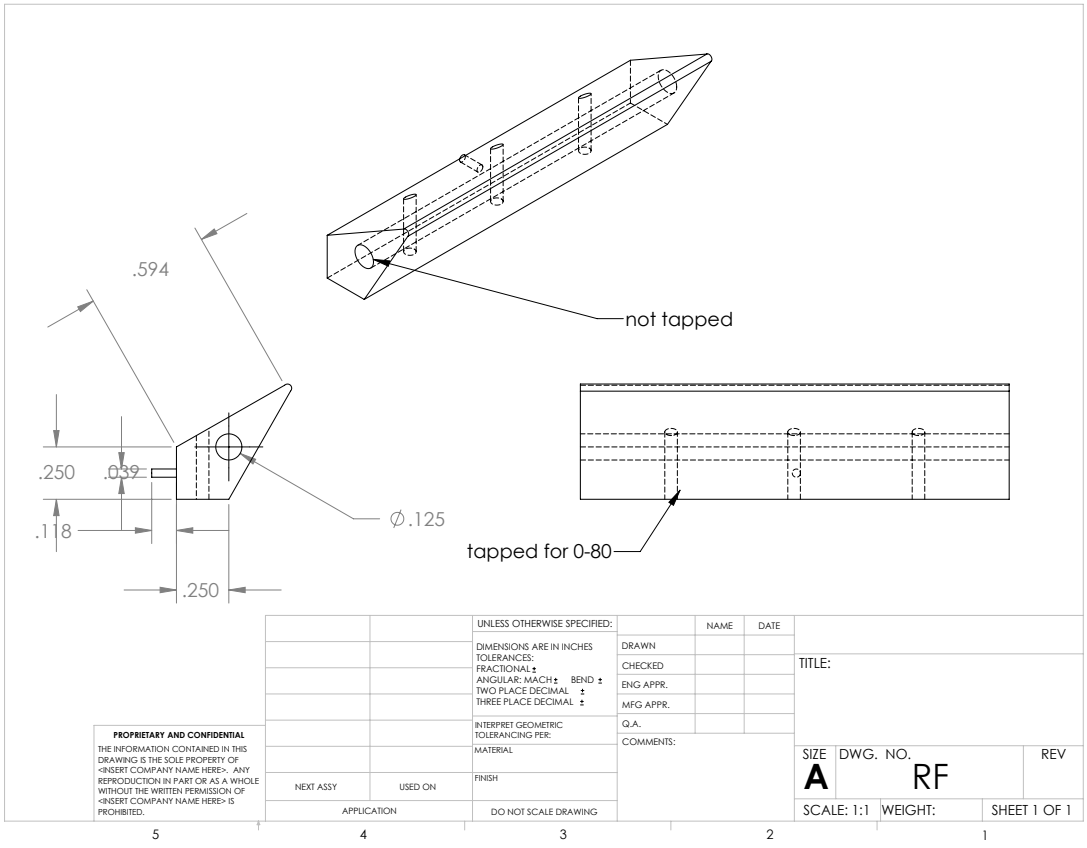

Figure 56: Goeders trap RF electrode

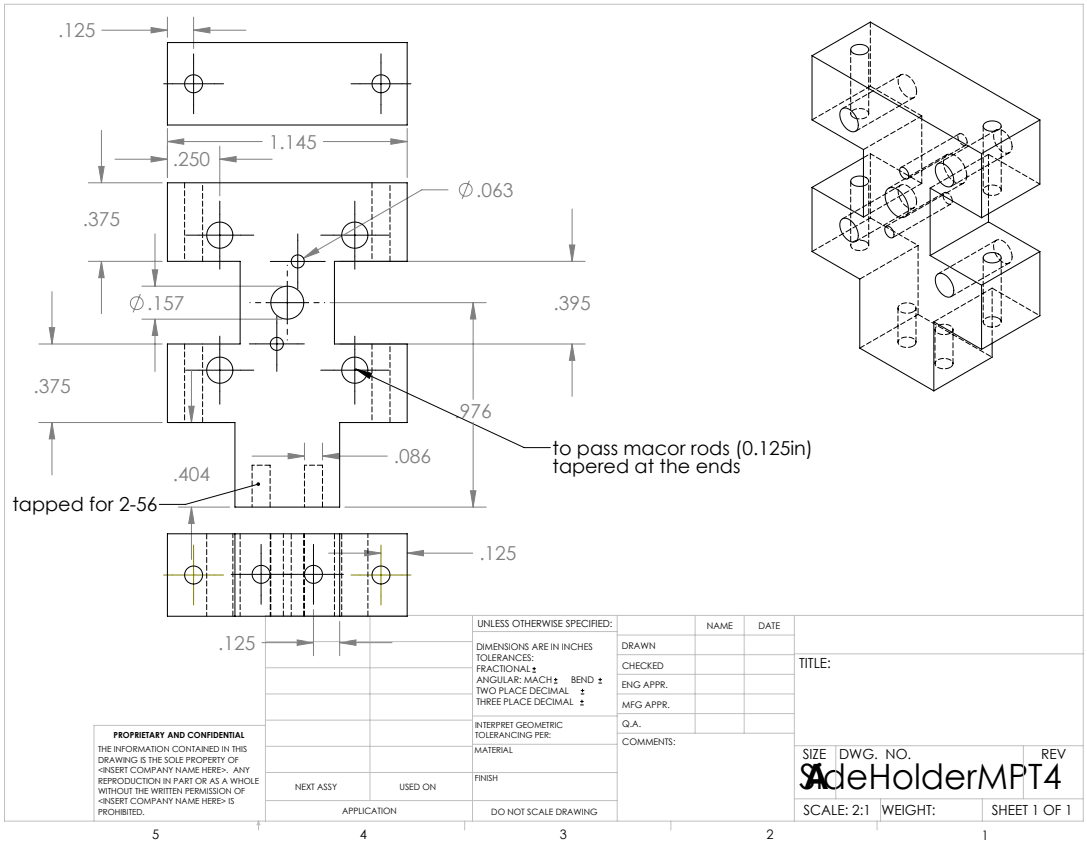

Figure 57: Goeders trap endpiece for $r_0 = 1$ mm

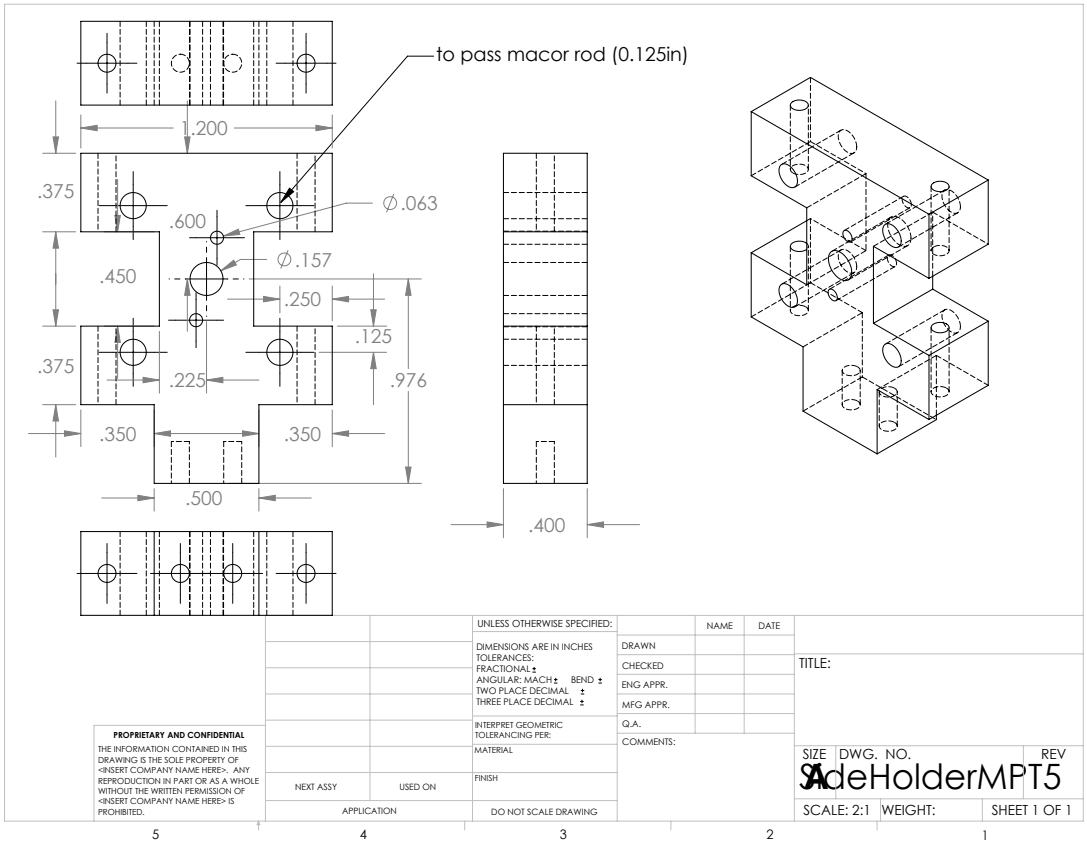

Figure 58: Goeders trap endpiece for $r_0 = 2$ mm

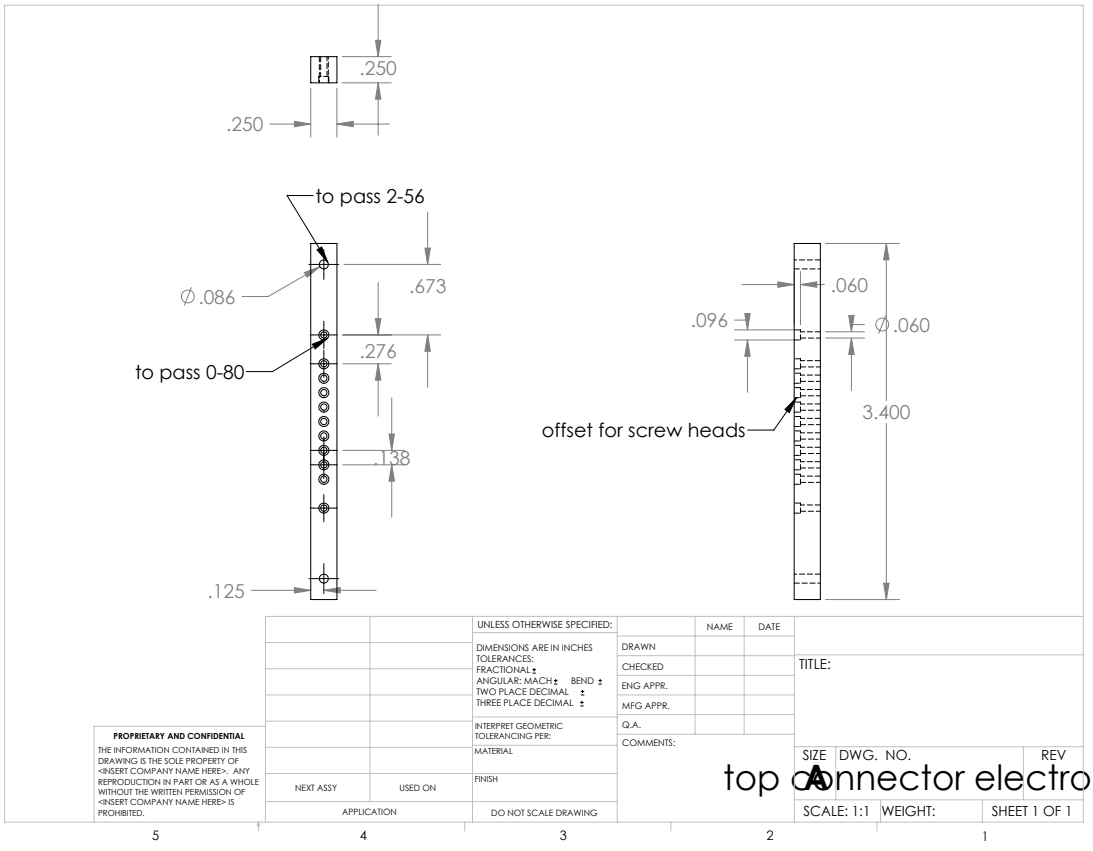

Figure 59: Goeders trap top MACOR bar for DC electrodes

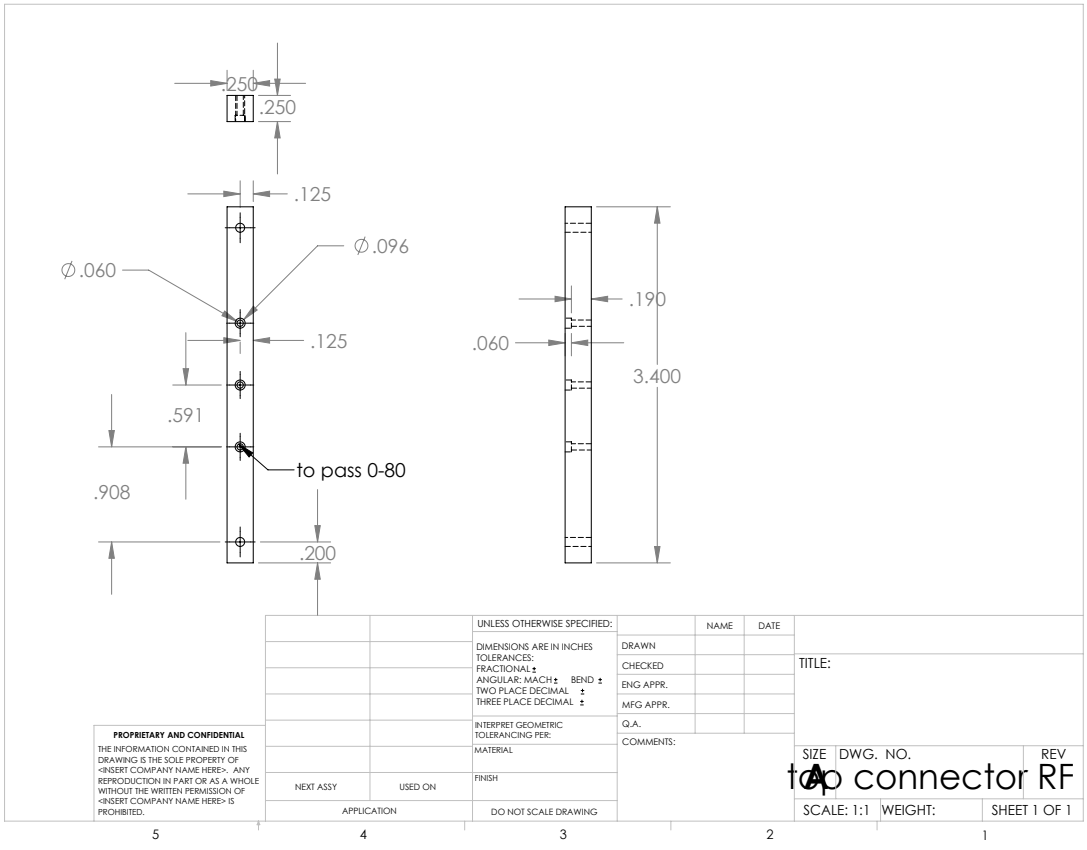

Figure 60: Goeders trap top MACOR bar for RF electrodes

REFERENCES

[1] *The Spectra and Dynamics of Diatomic Molecules* (Elsevier Academic Press, 2004).

[2] P. K. Ghosh, *Ion Traps* (Clarnedon Press, 1995).

[3] R. F. Wuerker, H. Shelton, and R. V. Langmuir, "Electrodynamic containment of charged particles," *J. Appl. Phys.* **30**, 342 (1959).

[4] H. J. Metcalf and P. van der Straten, *Laser Cooling and Trapping* (Springer, 1999).

[5] W. M. Itano, J. C. Bergquist, J. J. Bollinger, and D. J. Wineland, "Cooling Methods in Ion Traps," *Phys. Scr.* **T59**, 106 (1995).

[6] Y. Hashimoto, D. Nagamoto, and S. Hasegawa, "Isotope selective manipulatiion and observation of Ca^+ ions by ion trap-laser cooling technique," *Int. J. Mass spectrom.* **279**, 163 (2009).

[7] M. Drewsen, I. Jensen, J. Lindballe, N. Nissen, R. Martinussen, A. Mortensen, P. Staanum, and D. Voigt, "Ion Coulomb crystals: a tool for studying ion processes," *Int. J. Mass spectrom.* **229**, 83 (2003).

[8] S. Willitsch, M. T. Bell, A. D. Gingell, and T. P. Softley, "Chemical applications of laser- and sympathetically-cooled ions in ion traps," *Phys. Chem. Chem. Phys.* **10**, 7200 (2008).

[9] R. Blatt and D. Wineland, "Entangled states of trapped atomic ions," *Nature* **453**, 1008 (2008).

[10] S. Willitsch, "Coulomb-crystallised molecular ions in traps: methods, applications, prospects," *Int. Rev. Phys. Chem.* **31**, 175 (2012).

[11] D. F. V. James, "Theory of Heating of the Quantum Ground State of Trapped Ions," *Phys. Rev. Lett.* **81**, 317 (1998).

[12] T. Baba and I. Waki, "Cooling and Mass-Analysis of Molecules Using Laser-Cooled Atoms," *Jpn. J. Appl. Phys* **35**, L1134 (1996).

[13] R. V. Krems, W. C. Stwalley, and B. Friedrich, *Cold Molecules: Theory, Experiment, Applications* (CRC Press, 2009).

[14] D. F. V. James, "Quantum dynamics of cold trapped ions with application to quantum computation," *Appl. Phys. B* **66**, 181 (1998).

[15] J. C. J. Koelemeij, B. Roth, A. Wicht, I. Ernsting, and S. Schiller, "Vibrational Spectroscopy of HD^+ with 2-ppb Accuracy," *Phys. Rev. Lett.* **98**, 173002 (2007).

[16] V. L. Ryjkov, X. Zhao, and H. A. Schuessler, "Sympathetic cooling of fullerene ions by laser-cooled Mg^+ ions in a linear rf trap," *Phys. Rev. A: At. Mol. Opt. Phys.* **74** (2006).

[17] K. Mølhave and M. Drewsen, "Formation of translationally cold MgH^+ and MgD^+ molecules in an ion trap," *Phys. Rev. A: At. Mol. Opt. Phys.* **62**, 011401 (2000).

[18] M. Drewsen, A. Mortensen, R. Martinussen, P. Staanum, and J. L. Sørensen, "Nondestructive Identification of Cold and Extremely Localized Single Molecular Ions," *Phys. Rev. Lett.* **93**, 243201 (2004).

[19] B. Roth, U. Fröhlich, and S. Schiller, "Sympathetic cooling of $^4He^+$ ions in a radio-frequency trap," *Phys. Rev. Lett.* **94** (2005).

[20] P. Blythe, B. Roth, U. Fröhlich, H. Wenz, and S. Schiller, "Production of Ultracold Trapped Molecular Hydrogen Ions," *Phys. Rev. Lett.* **95**, 183002 (2005).

[21] A. Ostendorf, C. B. Zhang, M. A. Wilson, D. Offenberg, B. Roth, and S. Schiller, "Sympathetic Cooling of Complex Molecular Ions to Millikelvin Temperatures," *Phys. Rev. Lett.* **97**, 243005 (2006).

[22] D. Offenberg, C. B. Zhang, C. Wellers, B. Roth, and S. Schiller, "Translational cooling and storage of protonated proteins in an ion trap at subkelvin temperatures," *Phys. Rev. A: At. Mol. Opt. Phys.* **78**, 061401 (2008).

[23] V. A. Alekseev and D. D. Krylova, "Sympathetic Cooling of Two Trapped Ions," *Phys. Scr.* **51**, 368 (1995).

[24] T. Papenbrock, A. N. Salgueiro, and H. A. Weidenmüller, "Rate equations for sympathetic cooling of trapped bosons or fermions," *Phys. Rev. A: At. Mol. Opt. Phys.* **65**, 043601 (2002).

[25] T. Baba and I. Waki, "Spectral shape of *in situ* mass spectra of sympathetically cooled molecular ions," *J. Appl. Phys* **92**, 4109 (2002).

[26] M. D. Barrett, B. DeMarco, T. Schaetz, V. Meyer, D. Leibfried, J. Britton, J. Chiaverini, W. M. Itano, B. Jelenkovic, J. D. Jost, C. Langer, T. Rosenband, and D. J. Wineland, "Sympathetic cooling of $^9Be^+$ and $^{24}Mg^+$ for quantum logic," *Phys. Rev. A: At. Mol. Opt. Phys.* **68**, 042302 (2003).

[27] P. O. Schmidt, T. Rosenband, C. Langer, W. M. Itano, J. C. Bergquist, and D. J. Wineland, "Spectroscopy using quantum logic," *Science* **309**, 749 (2005).

[28] V. Batteiger, S. Knünz, M. Herrmann, G. Saathoff, H. A. Schüessler, B. Bernhardt, T. Wilken, R. Holzwarth, T. W. Hänsch, and T. Udem, "Precision spectroscopy of the $3s$-$3p$ fine-structure doublet in Mg^+," *Phys. Rev. A: At. Mol. Opt. Phys.* **80**, 022503 (2009).

[29] A. L. Wolf, S. A. van den Berg, W. Ubachs, and K. S. E. Eikema, "Direct Frequency Comb Spectroscopy of Trapped Ions," *Phys. Rev. Lett.* **102** (2009).

[30] A. L. Wolf, S. A. van den Berg, C. Gohle, E. J. Salumbides, W. Ubachs, and K. S. E. Eikema, "Frequency metrology on the $4s^2S_{1/2}$-$4p^2P_{1/2}$ transition in $^{40}Ca^+$ for a comparison with quasar data," *Phys. Rev. A: At. Mol. Opt. Phys.* **78** (2008).

[31] M. Herrmann, V. Batteiger, S. Knünz, G. Saathoff, T. Udem, and T. W. Hänsch, "Frequency Metrology on Single Trapped Ions in the Weak Binding Limit: The $3s_{1/2}$-$3p_{3/2}$ Transition in $^{24}Mg^+$," *Phys. Rev. Lett.* **102**, 013006 (2009).

[32] T. Rosenband, P. O. Schmidt, D. B. Hume, W. M. Itano, T. M. Fortier, J. E. Stalnaker, K. Kim, S. A. Diddams, J. C. J. Koelemeij, J. C. Bergquist, and D. J. Wineland, "Observation of the $^1S_0$-¿$^3P_0$ clock transition in $^{27}Al^+$," *Phys. Rev. Lett.* **98**, 220801 (2007).

[33] T. Rosenband, D. B. Hume, P. O. Schmidt, C. W. Chou, A. Brusch, L. Lorini, W. H. Oskay, R. E. Drullinger, T. M. Fortier, J. E. Stalnaker, S. A. Diddams, W. C. Swann, N. R. Newbury, W. M. Itano, D. J. Wineland, and J. C. Bergquist, "Frequency ratio of Al^+ and Hg^+ single-ion optical clocks; Metrology at the 17th decimal place," *Science* **319**, 1808 (2008).

[34] W. Schnitzler, N. M. Linke, R. Fickler, J. Meijer, F. Schmidt-Kaler, and K. Singer, "Deterministic Ultracold Ion Source Targeting the Heisenberg Limit," *Phys. Rev. Lett.* **102** (2009).

[35] S. Willitsch, M. T. Bell, A. D. Gingell, S. R. Procter, and T. P. Softley, "Cold reactive collisions between laser-cooled ions and velocity-selected neutral molecules," *Phys. Rev. Lett.* **100** (2008).

[36] M. T. Bell and T. P. Softley, "Ultracold molecules and ultracold chemistry," *Mol. Phys.* **107**, 99 (2009).

[37] L. D. Carr, D. DeMille, R. V. Krems, and J. Ye, "Cold and ultracold molecules: science, technology and applications," *New J. Phys.* **11**, 055049 (2009).

[38] M. T. Bell, A. D. Gingell, J. M. Oldham, T. P. Softley, and S. Willitsch, "Ion-molecule chemistry at very low temperatures: cold chemical reactions between Coulomb-crystallized ions and velocity-selected neutral molecules," *Faraday Discuss.* **142**, 73 (2009).

[39] K. Okada, M. Wada, L. Boesten, T. Nakamura, I. Katayama, and S. Ohtani, "Acceleration of the chemical reaction of trapped Ca^+ ions with H_2O molecules by laser excitation," *J. Phys. B.-At. Mol. Opt.* **36**, 33 (2003).

[40] B. Roth, P. Blythe, H. Wenz, H. Daerr, and S. Schiller, "Ion-neutral chemical reactions between ultracold localized ions and neutral molecules with single-particle resolution," *Phys. Rev. A: At. Mol. Opt. Phys.* **73**, 042712 (2006).

[41] B. Roth, R. Blythe, H. Daerr, L. Patacchini, and S. Schiller, "Production of ultracold diatomic and triatomic molecular ions of spectroscopic and astrophysical interest," *J. Phys. B: At. Mol. Opt. Phys.* **39**, S1241 (2006).

[42] P. F. Staanum, K. Højbjerre, R. Wester, and M. Drewsen, "Probing isotope effects in chemical reactions using single ions," *Phys. Rev. Lett.* **100**, 243003 (2008).

[43] K. Højbjerre, D. Offenberg, C. Z. Bisgaard, H. Stapelfeldt, P. F. Staanum, A. Mortensen, and M. Drewsen, "Consecutive photodissociation of a single complex molecular ion," *Phys. Rev. A: At. Mol. Opt. Phys.* **77**, 030702 (2008).

[44] D. Offenberg, C. Wellers, C. B. Zhang, B. Roth, and S. Schiller, "Measurement of small photodestruction rates of cold, charged biomolecules in an ion trap," *J. Phys. B: At. Mol. Opt. Phys.* **42**, 035101 (2009).

[45] S. Schiller and V. Korobov, "Tests of time independence of the electron and nuclear masses with ultracold molecules," *Phys. Rev. A: At. Mol. Opt. Phys.* **71** (2005).

[46] M. Ziskind, C. Daussy, T. Marrel, and C. Chardonnet, "Improved sensitivity in the search for a partiy-violating energy difference in the vibrational spectrum of the enantiomers of CHFClBr," *Eur. Phys. J. D.* **20**, 219 (2002).

[47] J. Crassous, C. Chardonnet, T. Saue, and P. Schwerdtfeger, "Recent experimental and theoretical developments towards the observation of parity violation (PV) effects in molecules by spectroscopy," *Org. Biomol. Chem.* **3**, 2218 (2005).

[48] D. Gerlich, "Applications of rf fields and collision dynamics in atomic mass spectrometry," *J. Anal. At. Spectrom.* **19**, 581 (2004).

[49] W. W. Smith, O. P. Makarov, and J. Lin, "Cold ion-neutral collisions in a hybrid trap," *J. Mod. Opt.* **52**, 2253 (2005).

[50] B. Odom, personal communication.

[51] L. Hornekaer, "Single and multi-species coulomb ion crystals: structures, dynamics and sympathetic cooling," 2000.

[52] K. H.W., *Molecular Rotation Spectra* (Dover Publications, 1992).

[53] B. Roth, J. C. J. Koelemeij, H. Daerr, and S. Schiller, "Rovibrational spectroscopy of trapped molecular hydrogen ions at millikelvin temperatures," *Phys. Rev. A: At. Mol. Opt. Phys.* **74**, 040501 (2006).

[54] M. Kajita and Y. Moriwaki, "Proposed detection of variation in m_p/m_e using a vibrational transition frequency of a CaH^+ ion," *J. Phys. B: At. Mol. Opt. Phys.* **42**, 154022 (2009).

[55] X. Calmet and H. Fritzsch, "The cosmological evolution of the nucleon mass and the electroweak coupling constants," *Eur. Phys. J. C* **24**, 639 (2002).

[56] P. Langacker, G. Segré, and M. J. Strassler, "Implications of gauge unification for time variation of the fine structure constant," *Phys. Lett. B* **528**, 121 (2002).

[57] V. V. Flambaum, D. B. Leinweber, A. W. Thomas, and R. D. Young, "Limits on variations of the quark masses, QCD scale, and fine structure constant," *Phys. Rev. D: Part. Fields* **69** (2004).

[58] E. Reinhold, R. Buning, U. Hollenstein, A. Ivanchik, P. Petitjean, and W. Ubachs, "Indicaton of a cosmological variation of the proton-electron mass ratio based on laboratory measurement and reanalysis of H_2 spectra," *Phys. Rev. Lett.* **96** (2006).

[59] K. Højbjerre, A. K. Hansen, P. S. Skyt, P. F. Staanum, and M. Drewsen, "Rotational state resolved photodissociation spectroscopy of translationally and vibrationally cold MgH^+ ions: toward rotational cooling of molecular ions," *New J. Phys.* **11**, 055026 (2009).

[60] P. F. Staanum, K. Højbjerre, P. S. Skyt, A. K. Hansen, and M. Drewsen, "Rotational laser cooling of vibrationally and translationally cold molecular ions," *Nat Phys* **6**, 271 (2010).

[61] T. Schneider, B. Roth, H. Duncker, I. Ernsting, and S. Schiller, "All-optical preparation of molecular ions in the rovibrational ground state," *Nat Phys* **6**, 275 (2010).

[62] D. J. Wineland and W. M. Itano, "Laser cooling of atoms," *Phys. Rev. A: At. Mol. Opt. Phys.* **20**, 1521 (1979).

[63] C. Monroe, D. M. Meekhof, B. E. King, S. R. Jefferts, W. M. Itano, D. J. Wineland, and P. Gould, "Resolved-Sideband Raman Cooling of a Bound Atom to the 3D Zero-Point Energy," *Phys. Rev. Lett.* **75**, 4011 (1995).

[64] D. B. Hume, C. W. Chou, D. R. Leibrandt, M. J. Thorpe, D. J. Wineland, and T. Rosenband, "Trapped-Ion State Detection through Coherent Motion," *Phys. Rev. Lett.* **107** (2011).

[65] D. J. Larson, J. C. Bergquist, J. J. Bollinger, W. M. Itano, and D. J. Wineland, "Sympathetic Cooling of Trapped Ions: A Laser-Cooled Two-Species Nonneutral Ion Plasma," *Phys. Rev. Lett.* **57**, 70 (1986).

[66] J. Shen, A. Borodin, M. Hansen, and S. Schiller, "Observation of a rotational transition of trapped and sympathetically cooled molecular ions," *Phys. Rev. A* **85** (2012).

[67] T. Merrill, "Compensating sequences for robust quantum control of trapped-ion qubits," 2013.

[68] J. T. Watson and O. D. Sparkman, *Introduction to mass spectrometry*volume 4 (Wiley, 2007).

[69] L. R. Churchill, "Trapping Triply Ionized Thorium Isotopes," 2010.

[70] R. Blümel, C. Kappler, W. Quint, and H. Walther, "Chaos and order of laser-cooled ions in a Paul trap," *Phys. Rev. A: At. Mol. Opt. Phys.* **40**, 808 (1989).

[71] F. Diedrich, E. Peik, J. M. Chen, W. Quint, and H. Walther, "Observation of a Phase-Transition of Stored Laser-Cooled Ions," *Phys. Rev. Lett.* **59**, 2931 (1987).

[72] M. Cetina, A. T. Grier, and V. Vuletić, "Micromotion-induced limit to atom-ion sympathetic cooling in Paul traps," *Phys. Rev. Lett.* **109**, 253201 (2012).

[73] W. Neuhauser, M. Hohenstatt, P. Toschek, and H. Dehmelt, "Optical-Sideband Cooling of Visibile Atom Cloud Confined in Parabolic Well," *Phys. Rev. Lett.* **41**, 233 (1978).

[74] R. C. Hilborn, "Einstein coefficients, cross-sections, f values, dipole moments, and all that," *Am. J. Phys* **50**, 982 (1982).

[75] J. F. Poyatos, J. I. Cirac, R. Blatt, and P. Zoller, "Trapped ions in the strong-excitation regime: Ion interferometry and nonclassical states," *Phys. Rev. A: At. Mol. Opt. Phys.* **54**, 1532 (1996).

[76] C. F. Roos, "Controlling the quantum state of trapped ions," 2000.

[77] B. W. Shore, "Definition of virtual levels," *Am. J. Phys* **47**, 262 (1979).

[78] W. Nagourney, J. Sandberg, and H. Dehmelt, "Shelved Optical Electron Amplifier: Observation of Quantum Jumps," *Phys. Rev. Lett.* **56**, 2797 (1986).

[79] N. Bohr, "On the Constitution of Atoms and Molecules," *Philos. Mag.* **26**, 1 (1913).

[80] T. Sauter, W. Neuhauser, R. Blatt, and P. E. Toschek, "Observation of quantum jumps," *Phys. Rev. Lett.* **57**, 1696 (1986).

[81] J. Bergquist, R. G. Hulet, W. M. Itano, and D. J. Wineland, "Observation of Quantum Jumps in a Single Atom," *Phys. Rev. Lett.* **57**, 1699 (1986).

[82] G. Ritter, S.-M. Bae, and W. Eichmann, "All-diode-laser cooling of single Ca^+ ions," *Appl. Phys. B* **66**, 609 (1998).

[83] K. Matsubara, K. Hayasaka, Y. Li, H. Ito, S. Nagano, M. Kajita, and M. Hosokawa, "Frequency Measurement of the Optical Clock Transition of $^{40}Ca^+$ with an Uncertainty of 10^{-14} Level," *Appl. Phys Express* **1** (2008).

[84] F. Diedrich, J. C. Bergquist, W. M. Itano, and D. J. Wineland, "Laser Cooling to the Zero-Point Energy of Motion," *Phys. Rev. Lett.* **62**, 403 (1989).

[85] J. Benhelm, G. Kirchmair, U. Rapol, T. Korber, C. Roos, and R. Blatt, "Measurement of the hyperfine structure of the $S_{1/2}$-$D_{5/2}$ transition in $^{43}Ca^+$," *Phys. Rev. A: At. Mol. Opt. Phys.* **75**, 032506 (2007).

[86] T. Furukawa, J. Nishimura, U. Tanaka, and S. Urabe, "Design and Characteristic Measurement of Miniature Three-Segment Linear Paul Trap," *Jpn. J. Appl. Phys., Part 1* **44**, 7619 (2005).

[87] D. R. Leibrandt, J. Labaziewicz, V. Vuletić, and I. L. Chuang, "Cavity sideband cooling of a single trapped ion," *Phys. Rev. Lett.* **103**, 103001 (2009).

[88] C. R. Clark, J. E. Goeders, Y. K. Dodia, C. R. Viteri, and K. R. Brown, "Detection of single-ion spectra by Coulomb-crystal heating," *Phys. Rev. A: At. Mol. Opt. Phys.* **81**, 043428 (2010).

[89] D. J. Berkeland, J. D. Miller, J. C. Bergquist, W. M. Itano, and D. J. Wineland, "Minimization of ion micromotion in a Paul trap," *J. Appl. Phys.* **83**, 5025 (1998).

[90] D. Berkeland, "Linear Paul trap for strontium ions," *Rev. Sci. Instrum.* **73**, 2856 (2002).

[91] D. Kielpinski, C. Monroe, and D. J. Wineland, "Architecture for a large-scale ion-trap quantum computer," *Nature* **417**, 709 (2002).

[92] K. R. Brown, C. R. Clark, J. E. Goeders, N. Khanyile, C. R. Viteri, and G. D. Vittorini, "Laser-cooled atomic ions as probes of molecular ions," *SMILES* (2010).

[93] H. Alloy, "Nitronic 50 - High Performance Alloys," 1997.

[94] A. Technologies, "Programmable DC Power Supplies," 2013.

[95] J. E. Goeders, C. R. Clark, G. Vittorini, K. Wright, C. R. Viteri, and K. R. Brown, "Identifying Single Molecular Ions by Resolved Sideband Measurements," *J. Phys. Chem. A.* (2013).

[96] S. C. Doret, "Transfer Cavity / Stabilized HeNe based Laser Frequency Stabilization," 2011.

[97] K. Matsubara, S. Uetake, H. Ito, Y. Li, K. Hayasaka, and M. Hosokawa, "Precise Frequenchy-Drift Measurement of Extended-Cavity Diode Laser Stabilized with Scanning Transfer Cavity," *Jpn. J. Appl. Phys., Part 1* **44**, 229 (2005).

[98] E. D. Black, "An introduction to Pound-Drever-Hall laser frequency stabilization," *Am. J. Phys* **69**, 79 (2001).

[99] G. Vittorini, "Development of a cryogenic surface-electrode ion trapping apparatus," 2013.

[100] K. Wright, "Performance of dynamic decoupling control sequences on trapped $^{40}Ca^{+}$," 2010.

[101] C. S. Nichols, "An FPGA-based microarchitecture for the implementation of quantum gates with trapped ions," 2012.

[102] M. J. McDonnell, J.-P. Stacey, S. C. Webster, J. P. Home, A. Ramos, D. M. Lucas, D. N. Stacey, and A. M. Steane, "High-Efficiency Detection of a Single Quantum of Angular Momentum by Suppression of Optical Pumping," *Phys. Rev. Lett.* **93**, 153601 (2004).

[103] S. Narayanan, N. Daniilidis, S. A. Möller, R. Clark, F. Ziesel, K. Singer, F. Schmidt-Kaler, and H. Häffner, "Electric field compensation and sensing with a single ion in a planar trap," *J. Appl. Phys.* **110**, 114909 (2011).

[104] *CRC Handbook of Chemistry and Physics 73rd ed.* (CRC Press, 1992-1993).

[105] S. Urabe, H. Imajo, K. Hayasaka, and M. Watanabe, "Trapping of Ca^{+} ions and optical detection," *Jpn. J. Appl. Phys.* **30**, L1532 (1991).

[106] E. Shimshoni, G. Morigi, and S. Fishman, "Quantum zigzag transition in ion chains," *Phys. Rev. Lett.* **106** (2011).

[107] D. H. E. Dubin, "Theory of Structural Phase-Transitions in a Trapped Coulomb Crystal," *Phys. Rev. Lett.* **71**, 2753 (1993).

[108] H. G. Dehmelt, "Mono-ion oscillator as potential ultimate laser frequency standard," *IEEE Trans. Instrum. Meas.* **31**, 83 (1982).

[109] R. G. DeVoe, J. Hoffnagle, and R. G. Brewer, "Role of laser damping in trapped ion crystals," *Phys. Rev. A: At. Mol. Opt. Phys.* **39**, 4362 (1989).

[110] C. W. Chou, D. B. Hume, J. C. J. Koelemeij, D. J. Wineland, and T. Rosenband, "Frequency Comparison of Two High-Accuracy Al^{+} Optical Clocks," *Phys. Rev. Lett.* **104**, 070802 (2010).

[111] D. A. Church, "Storage-Ring Ion Trap Derived from the Linear Quadrupole Radio-Frequency Mass Filter," *J. Appl. Phys.* **40**, 3127 (1969).

[112] B. Roth, P. Blythe, and S. Schiller, "Motional resonance coupling in cold multispecies Coulomb crystals," *Phys. Rev. A: At. Mol. Opt. Phys.* **75** (2007).

[113] C. Roos, T. Zeiger, H. Rohde, H. C. Nägerl, J. Eschner, D. Leibfried, F. Schmidt-Kaler, and R. Blatt, "Quantum state engineering on an optical transition and decoherence in a Paul trap," *Phys. Rev. Lett.* **83**, 4713 (1999).

[114] H. Rohde, S. T. Gulde, C. F. Roos, P. A. Barton, D. Leibfried, J. Eschner, F. Schmidt-Kaler, and R. Blatt, "Sympathetic ground-state cooling and coherent manipulation with two-ion crystals," *J. Opt. B: Quantum Semiclassical Opt.* **3**, S34 (2001).

[115] A. K. Hansen, M. A. Sørensen, P. F. Staanum, and M. Drewsen, "Single-Ion Recycling Reactions," *Angew. Chem. Int. Ed.* **51**, 7960 (2012).

[116] M. M. Chwalla, "Precision spectroscopy with $^{40}Ca^{+}$ ions in a Paul trap," 2009.

[117] J. Labaziewicz, "High Fidelity Quantum Gates with Ions in Cryogenic Microfabricated Ion Traps," 2008.

[118] Q. A. Turchette, D. Kielpinski, B. E. King, D. Leibfried, D. M. Meekhof, C. J. Myatt, M. A. Rowe, C. A. Sackett, C. S. Wood, W. M. Itano, C. Monroe, and D. J. Wineland, "Heating of trapped ions from the quantum ground state," *Phys. Rev. A: At. Mol. Opt. Phys.* **61**, 063418 (2000).

[119] M. Drewsen, personal communication.

[120] H. Sawamura, K. Toyoda, and S. Urabe, "Optimization of Doppler cooling of a single $^{40}Ca^{+}$ ion," *Jpn. J. Appl. Phys., Part 1* **46**, 1713 (2007).

[121] J. H. Wesenberg, R. J. Epstein, D. Leibfreid, R. B. Blakestad, J. Britton, J. P. Home, W. M. Itano, J. D. Jost, E. Knill, C. Langer, R. Ozeri, S. Seidelin, and D. J. Wineland, "Fluorescence during Doppler cooling of single trapped atom," *Phys. Rev. A: At. Mol. Opt. Phys.* **76** (2007).

[122] S. Rainville, J. K. Thompson, and D. E. Pritchard, "An Ion Balance for Ultra-High-Precision Atomic Mass Measurements," *Science* **303**, 334 (2004).

[123] U. Bressel, A. Borodin, J. Shen, M. Hansen, I. Ernsting, and S. Schiller, "Manipulation of Individual Hyperfine States in Cold Trapped Molecular Ions and Application to HD^{+} Frequency Metrology," *Phys. Rev. Lett.* **108**, 183003 (2012).

[124] D. Kielpinski, B. E. King, C. J. Myatt, C. A. Sackett, Q. A. Turchette, W. M. Itano, C. Monroe, D. J. Wineland, and W. H. Zurek, "Sympathetic cooling of trapped ions for quantum logic," *Phys. Rev. A: At. Mol. Opt. Phys.* **61**, 032310 (2000).

[125] H. C. Nägerl, W. Bechter, J. Eschner, F. Schmidt-Kaler, and R. Blatt, "Ion strings for quantum gates," *Appl. Phys. B* **66**, 603 (1998).

[126] P. O. Schmidt, T. Rosenband, J. C. J. Koelemeij, D. B. Hume, W. M. Itano, J. C. Bergquist, and D. J. Wineland, "Spectroscopy of atomic and molecular ions using quantum logic," *Proc. Non-Neutral Plasma VI* , 305 (2006).

[127] G. Audi, A. Wapstra, and C. Thibault, "The Ame2003 atomic mass evaluation: (II). Tables, graphs and references," *Nuc. Phys. A* **729**, 337 (2003).

[128] S. Seidelin, J. Chiaverini, R. Reichle, J. J. Bollinger, D. Leibfried, J. Britton, J. H. Wesenberg, R. B. Blakestad, R. J. Epstein, D. B. Hume, W. M. Itano, J. D. Jost, C. Langer, R. Ozeri, N. Shiga, and D. J. Wineland, "Microfabricated surface-electrode ion trap for scalable quantum information processing," *Phys. Rev. Lett.* **96** (2006).

[129] C. E. Pearson, D. R. Leibrandt, W. S. Bakr, W. J. Mallard, K. R. Brown, and I. L. Chuang, "Experimental investigation of planar ion traps," *Phys. Rev. A: At. Mol. Opt. Phys.* **73**, 032307 (2006).

[130] R. J. Epstein, S. Seidelin, D. Leibfried, J. H. Wesenberg, J. J. Bollinger, J. M. Amini, R. B. Blakestad, J. Britton, J. P. Home, W. M. Itano, J. D. Jost, E. Knill, C. Langer, R. Ozeri, N. Shiga, and D. J. Wineland, "Simplified motional heating rate measurements of trapped ions," *Phys. Rev. A: At. Mol. Opt. Phys.* **76**, 033411 (2007).

[131] C. Clark, "Sympathetic heating and cooling of trapped atomic and molecular ions," 2012.

[132] D. M. Lucas, A. Ramos, J. P. Home, M. J. McDonnell, S. Nakayama, J.-P. Stacey, S. C. Webster, D. N. Stacey, and A. M. Steane, "Isotope-selective photoionization for calcium ion trapping," *Phys. Rev. A* **69**, 012711 (2004).

[133] E. Arimondo, "Relaxation processes in coherent-population trapping," *Phys. Rev. A: At. Mol. Opt. Phys.* **54**, 2216 (1996).

[134] J. K. Webb, V. V. Flambaum, C. W. Churchill, M. J. Drinkwater, and J. D. Barrow, "Search for time variation of the fine structure constant," *Phys. Rev. Lett.* **82**, 884 (1999).

[135] M. Abe, M. Kajita, M. Hada, and Y. Moriwaki, "*Ab initio* study on vibrational dipole moments of XH^+ molecular ions: X=^{24}Mg,^{40}Ca, ^{64}Zn, ^{88}Sr, ^{114}Cd, ^{138}Ba, ^{174}Yb and ^{202}Hg," *J. Phys. B: At. Mol. Opt. Phys.* **43**, 245102 (2010).